Doctoral Dissertation

博士論文

Thermal state of the upper mantle and the origin of the ophiolite pulse in the Cambrian-Ordovician time

（カンブリア-オルドビス紀における上部マントルの熱状態と
オフィオライトパルスの成因）

A Dissertation Submitted for the Degree of Doctor of Philosophy

December 2020

令和２年１２月博士（理学）申請

Department of Earth and Planetary of Science,

Graduate School of Science, The University of Tokyo

東京大学大学院 理学系研究科 地球惑星科学専攻

Takafumi Kimura

木村 皐史

Abstract

The Earth releases heat into the space, which drives internal and surface processes, such as magmatism, plate tectonics, and evolution of the surface environment. In this regard, the thermal history of the Earth is an essential part of its evolution. In order to better understand the past and future evolution of the Earth, it is important to reveal temporal changes of the thermal state of the mantle, which occupies 80 vol% of the solid Earth transferring heat to the Earth's surface by thermal convection. Ophiolites, suites of temporally and spatially associated ultramafic, mafic, and felsic magma-related rocks, were formed and exhumed at least since the Paleoproterozoic to the very recent past and may provide rich information on the thermal history of the Earth. Their age distributions show confined periods with high rates of occurrence in late Neoproterozoic, Cambrian-Ordovician, and Jurassic-Cretaceous times, which are called "ophiolite pulses".

The ophiolite pulses are explained by highly active superplumes (superplume model). However, the Cambrian-Ordovician pulse has two critical geological features that cannot be explained by such superplume model: predominance of subduction-related ophiolites and scarcity of plume-related magma activities. We addressed this issue by quantitatively estimating a mantle potential temperature (MPT) from ~500 Ma subduction-related ophiolite, Hayachine-Miyamori ophiolite. We developed a novel method to overcome difficulties in MPT estimation for an arc environment by using porphyritic ultramafic dikes showing flow differentiation, which have a record of intact chemical composition of a primitive magma including its water content because of their high pressure (~0.6 GPa) intrusion and rapid solidification. The melt segregation conditions for the primary magmas are estimated to be ~1430 ℃, ~5.0 GPa. Geochemical data of the dikes show decompressional melting of a depleted source mantle in the garnet stability field without a strong influence of slab-derived fluids. These results combined with the extensive

fluxed melting of the wedge mantle prior to the dike formation indicate sudden changes of the melting environment, its mechanism, and the source mantle from extensive fluxed melting of the wedge mantle to decompressional melting of sub-slab mantle most plausibly triggered by a slab breakoff. The MPT of the sub-slab mantle is estimated to be ~1350 °C. The value is within the range of MPTs estimated from rare Cambrian-Ordovician mid-ocean ridge type ophiolites (1330 – 1410 ℃) by applying our MPT estimation method. The range of MPT thus represents the global thermal state of the Cambrian-Ordovician upper mantle. Furthermore, they are essentially the same as the global MPTs of the present-day upper mantle. We conclude that the Cambrian-Ordovician ophiolite pulse dominated by the supra-subduction type is not attributable to high-temperature of the upper mantle as proposed by the superplume model. The common generation of magma by decompressional melting of MORB mantle source at high pressure during the Cambrian-Ordovician ophiolite pulse is also supported by the compilation of REE ratios of the world ophiolites belonging to the ophiolite pulse. We propose frequent occurrence of slab breakoff during the Cambrian-Ordovician ophiolite pulse (slab breakoff model). The assembly of the Gondwana supercontinent accompanied by continent-continent and/or continent-arc collisions caused frequent occurrence of slab breakoff and following obduction of many ophiolites.

We further examined evolutional dynamics of the slab breakoff process in the Cambrian-Ordovician northeast Japan in high time resolution on the time scale of shorter than a few million years. We used chondrite-normalized REE ratios of clinopyroxene in the cumulate to develop proxies for magma generation conditions in the mantle: (Sm/Gd)n, (Dy/Yb)n, and (Ce/Sm)n for degree of melting (F), percentage of melting in the garnet stability field in total melting (PMGF), and material influx rate (β), respectively. We clarified temporal change of melting conditions recorded in the Cumulate Member after establishing stratigraphy of the cumulate. The

stratigraphic variations of the PMGFs, Fs, and βs show large variations in the middle and lower zones but are consistent and close to those of the ultramafic dikes in the upper zone, showing a tendency of convergence to the values of the ultramafic dikes, which formed after complete solidification of the Cumulate Member. The F and β show overall decreases with stratigraphic horizon from the lower to the upper zone, but the PMGF does not. There is no correlation between F and β if data with high values of β are ignored, indicating that the melting mechanism is dominated by decompressional melting with minor contribution of slab-derived fluid. There is a weak overall correlation between F and PMGF, and the correlation is very tight if data with high values of β are ignored. On the basis of these variations, we propose the following scenario for the evolution of slab-breakoff in the Cambrian-Ordovician northeast Japan arc. The slab breakoff took place at the depth of ~140 km and triggers counter flows and passive upwelling of the sub-slab mantle from various depths ranging 140 – 250 km, which induced decompressional melting generating magmas for the lower and middle zones of the Cumulate Member. In this initial stages, melting of the wedge mantle material affected by slab-derived fluids may have taken place. As the slab sunk, the flux melting became suppressed, and upwelling and decompressional melting continued, but the upwelling depths tend to have been narrowed and confined to the depth range 160 – 190 km, which generated magmas for the upper zone of the Cumulate Member. After the formation of the Cumulate Member, the counter flows waned, but a very small amount of magma formed by decompressional melting at the depth of ~170 km, which generated magmas for the ultramafic dikes.

The Fe-Mg heterogeneity developed in tectonite xenoliths in cumulate and that at the boundary between the ultramafic dike and the host cumulate give constraints on the duration of magmatism of the Cumulate Member and subsequent cooling and the duration of the cooling after cessation of the

magmatism, respectively, the difference of which gives the time scale of magmatism of the Cumulate Member. We thus succeeded in estimation of time scale of slab breakoff event, which is shorter than a few million years. The catastrophic nature of slab breakoffs may trigger episodic cooling of the mantle from the upper thermal boundary layer of the Earth if its frequent occurrence culminates in an ophiolite pulse.

Table of contents

1. General Introduction

1.1 Thermal history of the Earth and the origin of ophiolite pulse

The Earth releases heat into the space, which drives internal and surface processes, such as magmatism, plate tectonics, and evolution of the surface environment (Davies, 1999). In this regard, the thermal history of the Earth is an essential part of its evolution. The major volume (~80 %) of the Earth is occupied by the mantle, which is transferring heat to the Earth's surface by thermal convection. It is, therefore, important to reveal the thermal state of the mantle and temporal changes in its thermal state in order to better understand the past and future evolution of the Earth.

A quantitative proxy of a thermal state of the mantle is the mantle potential temperature (MPT: McKenzie and Bickle, 1988). It has been estimated from the chemical compositions of magmas erupted on the Earth's surface at various tectonic settings, such as mid-ocean ridges and intraplate settings (Putirka, 2005; Lee at al., 2009; Herzberg et al., 2010) as well as volcanic arcs (Lee at al., 2009; Sakuyama et al., 2009, 2014). A secular change of the global thermal state of the mantle has been estimated from MPTs at restricted tectonic settings (non-arc environments, such as spreading centers; Herzberg et al., 2010; Fig. 1-1). The estimated secular change of the global MPTs is consistent to the parameterized convection models to first order approximation (Herzberg et al., 2010; Korenaga, 2008a, 2008b; Fig. 1-1). The models, however, do not allow us to discuss higher order features, such as episodic thermal events suggested by geological igneous records. In order to better understand the thermal history of the Earth including such episodicity, we need to clarify the relationships of the strength of the magmatic activity induced directly by mantle melting and the global MPTs at a high time resolution.

A large igneous province (LIP) is characterized by intraplate magmatisms and presumed to have formed related to mantle plumes, a upwelling of hot mantle originates deep in the mantle, either from the core-mantle boundary or the mantle transition zone (Ernst and Buchan, 2003). A periods of frequent occurrence of the mantle plumes marked by peaks in the age distribution of large igneous provinces (LIPs) are interpreted to be catastrophic superplume event (e.g., Maruyama, 1994; Condie, 2001; Ernst and Buchan, 2003). The high rates of juvenile crust formation indicated by peaks in the U-Pb age distribution of igneous zircons are also interpreted to be a consequence of the superplume events (e.g., Condie, 1998, 2001, 2004). The superplume events are thought to have taken place prior to breakup of the supercontinents, such as Rodinia and Pangea (Pavoni 1997; Burke and Torsvik, 2004). The superplume events are inferred to have been caused higher temperatures of the upper mantle and consequential higher rate of melt generation than the normal state (Niu et al., 2002). In this regard, the Jurassic-Cretaceous superplume event is proposed to be one of such cases, which is substantiated by that the estimated MPTs of the upper mantle beneath the mid-Atlantic ridge in the mid-Jurassic time (170 Ma) are hotter by ~50 ℃ than that of the modern mid-Atlantic ridge (Van Avendonk et al., 2016).

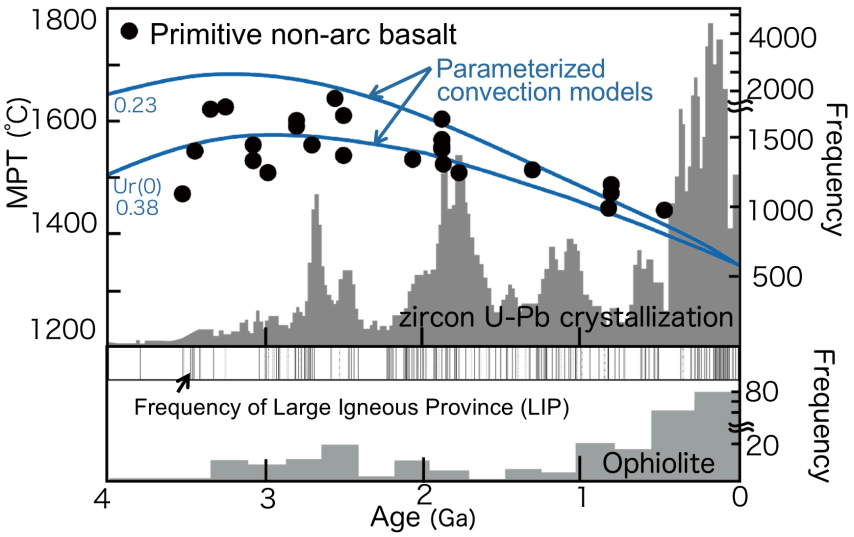

Fig. 1-1 Petrological estimates of secular change of mantle potential temperatures (MPTs) for primitive non-arc basalts (solid circles; Herzberg et al., 2010), age histogram of U-Pb ages of the igneous zircons (top histogram; Campbell and Allen, 2008), frequency of large igneous provinces (LIPs) (stripes; Ernst and Buchan, 2003), and frequency of ophiolite occurrence (bottom histogram; Furnes et al., 2014). These events are compared with a parameterized secular thermal evolution model for ambient upper mantle (blue curves; Korenaga, 2008a, 2008b). Numbers attached to model curves represent the assumed present-day Urey ratios (Ur(0)).

Ophiolites, which are defined in this paper as suites of temporally and spatially associated ultramafic, mafic, and felsic rocks related directly to magmas derived from the upper mantle (Dilek and Furnes, 2011, 2014), were formed and exhumed at least since the Paleoproterozoic to the very recent past (Stern, 2005). Their age distributions show several confined periods with high rates of occurrence, which are called “ophiolite pulses” (Abbate et al., 1985; Ishiwatari, 1994; Yakubchuk et al., 1994). These pulses occur in late Neoproterozoic, Cambrian-Ordovician, and Jurassic-Cretaceous times (Ishiwatari, 1994; Dilek, 2003). They have been explained by episodic activities of superplumes in 300 million years cycles, which induced more efficient

obduction of oceanic plates either by higher than normal rates of oceanic plateau production or increased rates of plate convergence (Ishiwatari, 1994; Dilek, 2003; Vaughan and Scarrow, 2003). We will refer to this hypothesis for the ophiolite pulse origin as the "superplume model". This model seems to be consistent with Jurassic-Cretaceous pulse as mentioned above. It does not, however, explain two critical features of the Cambrian-Ordovician ophiolite pulse. First, the Cambrian-Ordovician ophiolite pulse is dominated by subduction-related ophiolites thought to have formed mostly in a back-arc environment, which is in contrast to the minor occurrence of subduction-related ophiolites for the Jurassic-Cretaceous pulse (Dilek and Furnes, 2011; Furnes et al., 2014). This peculiarity of the pulse in ophiolite types requires some mechanisms to explain the high rate of subduction-related ophiolite formation during the Cambrian-Ordovician time. Second, there is almost no report of large igneous provinces (LIPs), which are believed to be closely related to mantle plume activities, during the Cambrian-Ordovician time. Ernst and Buchan (2003) compiled world LIPs since 4000Ma, which shows that LIP generation was significantly suppressed during the Cambrian-Ordovician compared to that during the Jurassic-Cretaceous. Because there are such fundamental inconsistencies between the essential features of Cambrian-Ordovician geological records and the superplume model, the origin of the Cambrian-Ordovician ophiolite pulse should be reappraised.

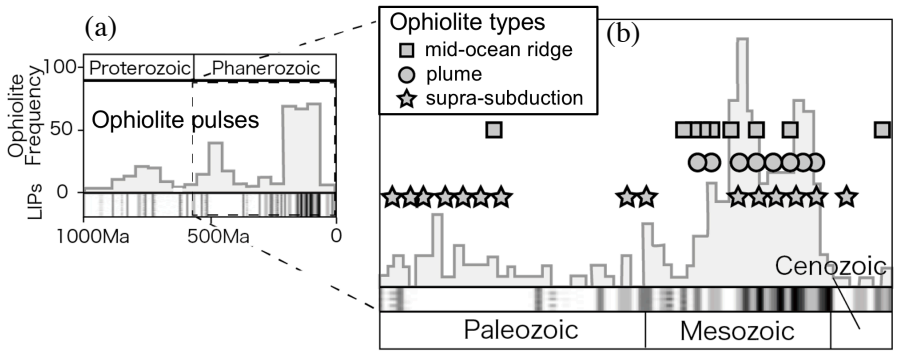

Fig. 1-2 Frequency distribution of formation ages of ophiolites and large igneous provinces (LIPs). (a) The histogram of formation ages of world ophiolites (Ishiwatari, 1994; Dilek and Furnes, 2011), and LIPs (Ernst and Buchan, 2003) from Neoproterozoic time to the present. Three high frequency periods of ophiolite occurrence, which are called ophiolite pulses, are noted. They are late Neoproterozoic, Cambrian-Ordovician, and Jurassic-Cretaceous times. (b) A blow-up of the younger ages (Phanerozoic time) of (a) with additional information on tectonic environments for ophiolite formation after Dilek and Furnes (2011). Tectonic environments are classified into three: gray star, supra-subduction type; gray circle, plume type; and gray square, mid−ocean ridge type.

In order to construct an appropriate model for the Cambrian-Ordovician ophiolite pulse and to seek a general model of ophiolite pulses through the Earth's history by considering the secular change of thermal state of the mantle, it is imperative to carefully evaluate dynamics involved in the formation of each ophiolite by examining the mechanisms of magma generation in the mantle, its MPT, and the controlling tectonics. We developed a new procedure for the estimation of magma generation conditions and the MPTs by examining ultramafic intrusive rocks in the mantle section of an ~500 Ma arc ophiolite, the Hayachine-Miyamori ophiolite (Ozawa et al., 2015), northern Japan. We carefully examined rare earth element (REE) patterns to find parameters useful to constrain melting conditions from REE data being consistent with those

estimated from the major element information. We apply the major and REE methods to the literature data from world ophiolites belonging to the Cambrian-Ordovician ophiolite pulse to support the applicability of what we argue for based on the Hayachine-Miyamori ophiolite to global thermal state and global tectonics during the period.

1.2 Hot upwelling vs. cold downwelling in the mantle as causes of thermal episodicity

The relationships of episodic thermal history of the mantle and geological igneous records, such as age distributions of the LIPs, igneous zircons, and ophiolites have been discussed mostly in the framework of large-scale hot upwelling from the core-mantle boundary or the mantle transition zone (e.g., Maruyama, 1994; Condie, 2001; Ishiwatari, 1994; Dilek, 2003). Such models presume the lower or bottom thermal boundary layers situated in the deep mantle or the core-mantle boundary heated from below. It has been, however, suggested that a large-scale cold downwelling in the mantle, such as rapid subduction of oceanic lithosphere or frequent occurrence of slab breakoff as an alternative model to explain episodicity in magmatism (e.g., Anderson, 1994; Korenaga and Jordan, 2003, 2004), though their relevance to the global thermal state of the mantle is equivocal. Such models presume the upper or surface thermal boundary layer cooled from above.

Slab breakoff model was first proposed by Davies and von Blanckenburg (1995) as a conceptual model, which presumed that a continental collision results in a detachment of preceding subducting oceanic lithosphere by localized tensional deformation of the slab. They also propose that the detachment induces passive upwellings of a sub-slab asthenosphere to cause magmatism and metamorphism. Since then, the model has been widely applied to explain

evolution of past orogenic belts and subduction zones (e.g., Alps, Anatolia-Zagros, Mediterranean, Himalaya, Tibet, and Japan) and thermal perturbations in asthenosphere to generate magmatism. Annual citations related to the model have increased from ~200 to ~2400 within last 20 years (Niu et al., 2017). However, most of the past slab breakoffs have not been constrained by lines of solid geological evidence.

Slab breakoff models have been invoked by various geological records, such as, extensive alkali basaltic magmatism (Dal Piaz et al., 2003), bimodal basaltic and rhyolitic magmatism (Sui et al., 2013), granitoid batholith formation (Zhu et al., 2015), and rapid exhumations of ultra-high or high pressure metamorphic belts (Ernst et al., 1997). These records, however, do not require the slab breakoff tectonic model as an casual mechanism. The alkali basalt magmatisms occur in an intra-plate or rear-arc environments (e.g., Barragan et al., 2005; Kuritani et a., 2008). The bimodal magmatisms are reported from an inmature-arc environment (e.g., Shukuno et al., 2006). Yamato et al. (2008) argued from numerical modeling that the breakoff occurs after the first stages of exhumation of the high pressure metamorphic rocks and it does not cause the exhumation. Therefore, Niu et al. (2017) and Garzanti et al. (2018) warned that the slab breakoff models are mostly applied for a pure convenience in the literatures. They claimed necessity of objective re-evaluations of the tectonics based on solid lines of evidences.

Slab rupture, which is called as slab breakoff, slab detachment, slab tear, slab rip, slab window, or even slab fragmentation (Nolet, 2009), has been widely documented in the world present-day subduction zones by geophysical observations, such as seismic velocity and electrical conductivity measurements (Fig. 1-3). The first observation-based documentation of slab rupture came from studies of seismic tomography in the Mediterranean, in which ruptures at a depth of ~200 km beneath the southern Italy and Greece were imaged (Spakman, 1986; Spakman et al.,

1988). Above the slab ruptures, active volcanos at which less fractionated mafic magmas were erupted at ~6 Ma – present (e.g., Peccerillo, 2005; Armienti et al., 1988, 2004; El Azzouzi et al., 1999; Duggen et al., 2005). The slab ruptures reported so far are very diverse in terms of morphology, depth, spatial scale, and related volcanism (Nolet, 2009), as seen in that they are called in many different ways. It is not clear if they have an impact on the global thermal state of the mantle.

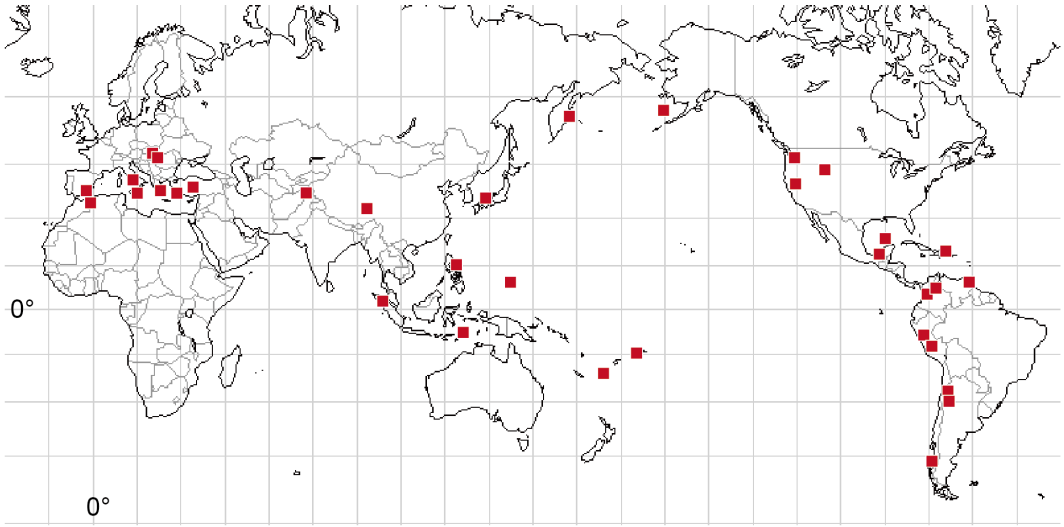

Fig. 1-3 Locations of present-day slab raptures (e.g., slab breakoff, slab detachment, slab tear, slab rip, slab window, and slab fragmentation) detected by geophysical observations, such as seismic velocity and electrical conductivity measurements from world subduction zones (Circum-Pacific belt: e.g., Fan et al., 2015; Liu et al., 2018; Sandiford, 2008; Miller et al., 2006; Obayashi et al., 2009; Cao et al., 2014; Sigloch et al., 2008; Bijwaard and Spakman., 2000; Gorbatov and Fukao, 2005; VanDecar et al., 2003; Vargas and Mann, 2013; Ávila and Dávila, 2018; Scire et al., 2015; Borgeaud et al., 2019; Lister et al., 2012; Levin et al., 2002. Alpine-Himalayan orogenic belt: e.g., Portner et al., 2018; Garcia-Castellanos and Villaseñor, 2011; Scarfì et al., 2018; Rosell et al., 2011; Spakman and Wortel, 2004; Bezada et al., 2013; Koulakov and Sobolev, 2006; Peng et al., 2016).

In this study, we propose the depth, source material, and mechanism of magma generation as solid lines of evidence for the slab breakoff. We will argue that decompressional melting of depleted mantle source at a depth of ~170 km in an arc environment provides strong evidence for the slab breakoff on the basis of our study of the Cambrian-Ordovician Hayachine-Miyamori ophiolite in northeast Japan. We further clarify the temporal change of the melting conditions during the slab breakoff on the time scale shorter than a few million years. We proposed that the slab breakoff frequently took place during Cambrian-Ordovician ophiolite pulse. We discussed that the episodicity in magmatisms in the Earth's thermal history is attributable not only to hot upwellings from the deep mantle, such as the core-mantle boundary and the mantle transition zone, but also by cold downwellings, such as frequent occurrences of slab breakoffs.

1.3 Outline of this thesis

The main part of this thesis following this introductory chapter (**Chapter 1**) consists of two chapters (**Chapter 2, 3**). **Chapter 2** is based on a paper entitled "Thermal state of the upper mantle and the origin of the Cambrian-Ordovician ophiolite pulse: Constraints from ultramafic dikes of the Hayachine-Miyamori ophiolite" published in *American Mineralogist*, volume 105, pp. 1778-1801, 2020, including additional discussion and modifying the structure. The newly developed estimation methods of the global MPT from arc environments is described in this chapter. "Slab breakoff model" is proposed for the origin of the Cambrian-Ordovician ophiolite pulse by applying the methods to the world ophiolites. **Chapter 3** is based on part of a conference proceeding entitled "Origin of the early Phanerozoic ophiolite pulse: constraints from cumulates and ultramafic dikes of the Hayachine-Miyamori ophiolite, northeast Japan" published in *Proceedings of the International Conference on Ophiolites and Oceanic Lithosphere*, pp.115-

117, 2020, supplemented with new data and careful discussions. In this chapter, temporal change in conditions of mantle melting on the time scale shorter than a few million years. is estimated from REE concentration of clinopyroxene in cumulus pile of the Hayachine-Miyamori ophiolite, on the basis of which mantle dynamics of the slab breakoff tectonics is discussed,

2. Thermal state of the upper mantle and the origin of the ophiolite pulse in the Cambrian-Ordovician time

2.1 Introduction

A secular change of the global thermal state of the mantle has been estimated from MPTs at restricted tectonic settings (non-arc environments, such as spreading centers; Herzberg et al., 2010; see, Fig. 1-1). This restriction of applicable tectonic environments guarantees that the global thermal state of the Earth is sampled by decompressional melting of either upper mantle that passively upwells along divergent margins, or deep mantle that actively upwells from a deep thermal boundary layer. Arc environments were avoided for this purpose because of: (1) involvement of water input from subducting slab into the magma generation environment and magma degassing during transportation to the surface and volcanic events which lead to technical difficulties in the estimation of MPTs, and (2) a thermal structure and flow pattern of the mantle wedge strongly affected by subduction of a slab, which could be in various thermal states depending on its age. These difficulties in application of the conventional methods to estimate a secular change of the global MPTs of the mantle from magma-related materials occurring in an arc environment must be overcome since there are several periods in the Earth's history when material records of primitive magmas are dominantly available from arc environments (Dilek and Furnes, 2011).

Ophiolite pulses, in which a large number of ophiolites formed in a confined period, are explained by highly active superplumes (superplume model; Ishiwatari, 1994; Dilek, 2003; Vaughan and Scarrow, 2003). However, the Cambrian-Ordovician pulse has two critical geological features that cannot be explained by such superplume model: scarcities of the LIPs (Ernst and Buchan, 2003) and the plume- and mid-ocean ridge-related ophiolites (Dilek and

Furnes, 2011; Furnes et al., 2014). In order to construct a model for the Cambrian-Ordovician ophiolite pulse and to seek a general model of ophiolite pulses through the Earth's history by considering the secular change of thermal state of the mantle, it is imperative to carefully evaluate dynamics involved in the formation of each ophiolite by examining the mechanisms of magma generation in the mantle, its MPT, and the controlling tectonics. It is, however, not easy to conduct this task for the Cambrian-Ordovician ophiolite pulse dominated by subduction related ophiolites (see Fig. 1-2b) because of the difficulties in the estimation of global MPT from arc volcanic rocks. Even if we could properly evaluate water content in the mantle to estimate MPTs, the estimated MTPs may represent a local thermal state of arc mantle wedges.

In this study, we extend the estimation methods of global MPTs proposed so far, whose application has been restricted to non-arc environments, to one applicable to arc environments. The novel approach is to use intrusive rocks, from which a proper melt composition, including its water content, can be estimated. We argue for a slab breakoff tectonic origin on the basis of the obtained magma generation conditions and the geological and petrologic data from the ophiolite. The MPTs are shown to represent the thermal state of the Cambrian-Ordovician upper mantle, which are comparable to the present day MPTs of the upper mantle. The implications of the MPTs and slab-breakoff tectonics for the origin of the Cambrian-Ordovician ophiolite pulse are discussed through compilation of major and trace element data from ophiolites of this age.

2.2 Previous studies of the Hayachine-Miyamori ophiolite

The Hayachine-Miyamori ophiolite, located in the South Kitakami Massif, northeast Japan (Fig. 2-1a), is composed of two complexes separated by the Hizume-Kesennuma fault.

They are the Miyamori complex distributed to the west and the Hayachine complex to the east of the fault (Fig. 2-1a). The two complexes consist mostly of peridotites, with lesser amounts of hornblende-rich mafic-ultramafic rocks and minor shallow intrusions and volcanic rocks. The ophiolite is divided into the Tectonite Member characterized by penetrative plastic deformation textures, and the Cumulate Member featuring cumulus textures without evidence of solid-state deformation (Fig. 2-1b). Their boundary is delineated within the Miyamori Complex and is an intrusive contact formed after the cessation of the main deformation of the Tectonite Member (Ozawa, 1983; 1984). The boundary strikes nearly parallel to the elongate distribution and layering of the Cumulate Member, striking ~N 40° W (Ozawa, 1984) (Fig. 2-1b). The Tectonite Member is further divided by Cr/(Cr + Al) ratio (Cr#) of spinel into the Chromite-bearing Ultramafic Suite (CRUS; Cr# > 0.4) and the Aluminous Spinel Ultramafic Suite (ASUS; Cr# < 0.4). The Hayachine complex is mostly composed of the ASUS. The Miyamori complex is mostly composed of the CRUS, and the rocks of ASUS occur as patches in the CRUS with sizes of several hundred meters to a kilometer (Ozawa, 1987b; Ozawa, 1988; Ozawa et al., 2015).

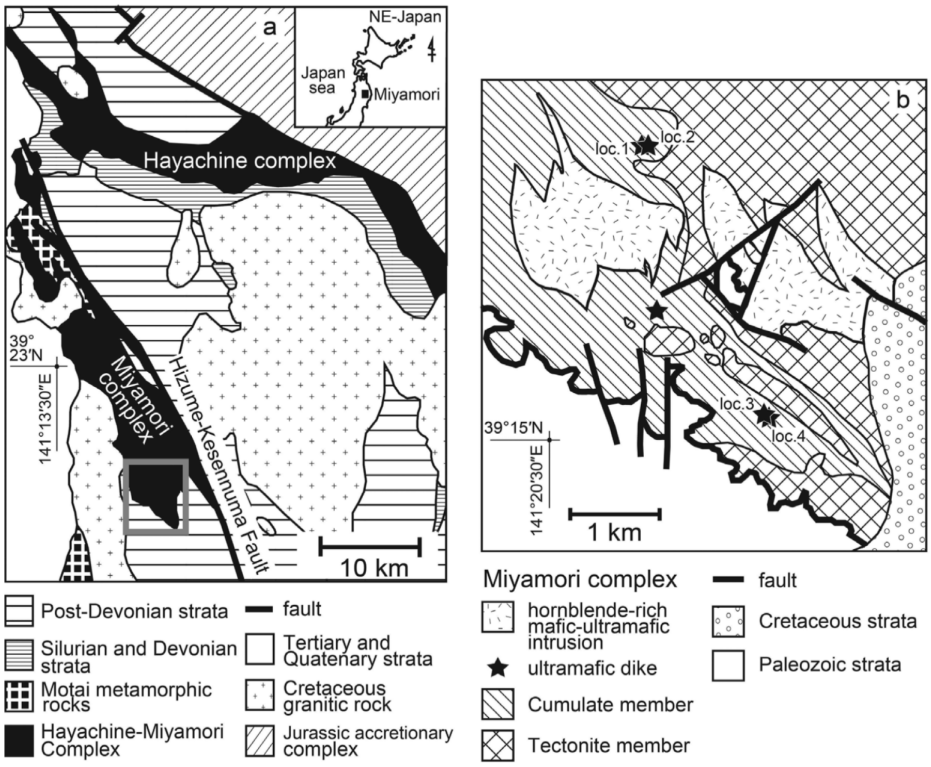

Fig.2-1 (a) Simplified geological map of the northwestern part of southern Kitakami Mountains showing distributions of the Miyamori and Hayachine ultramafic-mafic complexes in the Hayachine–Miyamori Ophiolite, Ordovician-Devonian strata, and Silurian-Devonian granitic rocks (after Ehiro and Suzuki, 2003; Kawamura at al., 2013; Ozawa, 1984; Maekawa, 1981). Gray rectangle in (a) represents the plot region of (b). (b) Geological map of the southern part of the Miyamori ultramafic-mafic complex located to the east of the Hizume-Kesennuma fault (modified after Ozawa et al., 2013). Localities of examined ultramafic dikes are shown by filled stars with locality numbers in (b). The dikes occur in the Cumulate Member near the contact with the Tectonite Member.

Ozawa (1984) showed that the Miyamori complex is a thrust sheet tectonically transported from the northwest to the current site over Paleozoic sedimentary rocks and metamorphic rocks distributed to the southwest of the Miyamori complex. The metamorphic rocks also occur in a tectonic window (1 km x 600 m) in the central part of the Miyamori complex, where pelitic schist, greenschist, epidote amphibolite, and amphibolite are distributed

from the west to the east in this order. These rocks could have been a metamorphic sole of the ophiolite as reported from beneath many ophiolites (Williams and Smyth, 1973; Jamieson, 1986) because of the short-distance transition of their metamorphic grade from the greenschist to amphibolite facies over the spatial scale of a few hundred meters. Their relationship with the ophiolite is, however, unclear due to the later tectonic disturbance.

The Hayachine-Miyamori ophiolite is one of the ophiolites belonging to the Cambrian-Ordovician ophiolite pulse. The exhumation and cooling of the ophiolite took place at ca. 450 Ma estimated by K-Ar ages of hornblende in hornblende-bearing mafic intrusive rocks (Ozawa et al., 1988; Shibata and Ozawa, 1992), and the magmatic events took place at 499 ± 65 Ma estimated by Sm-Nd isochron ages of clinopyroxene separated from lherzolite of the ASUS from the Hayachine complex (Yoshikawa and Ozawa, 2007; Ozawa et al., 2015). The Hizume-Kesennuma fault was active at least since the Jurassic time (Ehiro and Suzuki, 2003). The ophiolite is characterized by several features suggesting its formation in an arc environment, such as the presence of abundant amphibole and minor phlogopite in the mantle section with arc geochemical signatures, and is classified into the supra-subduction type according to Dilek and Furnes (2014). The geology, petrology, and geochemistry of the ophiolite have been extensively studied, and its tectonic history is well constrained in spite of intensive late-stage secondary processes, such as serpentinization, contact metamorphism by granite intrusions, and alteration since the Cambrian-Ordovician time (Ozawa, 1987a, 1988; Ozawa and Shimizu, 1995; Yoshikawa and Ozawa, 2007; Ozawa et al., 2015). The depth of formation of a magma body crystallizing the Cumulate Member in the already deformed Tectonite Member is estimated to be 18 ± 3 km (approx. 0.6 ± 0.1 GPa) according to the crystallization of plagioclase in equilibrium with olivine in the Cumulate Member at a high magmatic temperature and breakdown of plagioclase into

orthopyroxene and spinel-pargasite symplectite along with the contact with olivine at a low temperature (< ~800 °C; Ozawa, 1986). The pressure is too high for the depth of ultramafic cumulate sequences commonly reported from ophiolites, and suggests a thickened crust, though the crustal sections are mostly missing in the Hayachine-Miyamori ophiolites owing to tectonic processes during or after the emplacement. According to the geochemical features, such as TiO_2/K_2O in amphibole in ultramafic rocks, and Rb-Sr and Sm-Nd isotope systems for clinopyroxene in mafic and ultramafic rocks, it is inferred that the ASUS of the Hayachine complex was formed by decompressional melting of a depleted mantle in a back-arc basin environment, the CRUS by flux melting of the ASUS under strong influx of fluids from the subducting slab, and the Cumulate Member by decompressional melting of a depleted mantle (Ozawa, 1988; Ozawa and Shimizu, 1995; Yoshikawa and Ozawa, 2007).

From these extensive data and geological relationships with the surrounding Silurian-Devonian geological units, such as the Motai metamorphic rocks and the Hikami granitic rocks, Ozawa et al. (2015) proposed a tectonic model for the Hayachine-Miyamori ophiolite. The model consists of a series of events (1) – (4); (1) formation of the ASUS of the Hayachine complex by back-arc spreading in the Cambrian-Ordovician time (~500 Ma), (2) formation of the CRUS of the Miyamori complex by extensive flux melting accompanying slab rollback, (3) formation of the Cumulate Member by decompressional melting of the mantle triggered by slab breakoff, and (4) exhumation of the ophiolite at ~450 Ma.

2.3 Geology of ultramafic intrusive rocks

The ultramafic intrusive rocks, which have a picritic composition, occur in the Cumulate Member and never crosscut younger intrusive rocks such as the hornblende-rich mafic-ultramafic rocks and the andesite-rhyolite porphyries in the Miyamori complex (Fig. 2-1b). The ultramafic intrusive rocks are planar in morphology, sharply defined with a thickness of 0.5 to 30 cm, and strike from N47 °W to N10 °E, which is mostly oblique to the layered structure of the Cumulate Member. They crosscut the layering and weak foliation of the host rock and have many branches (Figs. 2-2a and 2-2c). They are coarse-grained and porphyritic (Figs. 2-2b and 2-3a) and do not have chilled margins in terms of grain size. Phenocrysts, mostly olivine with a minor amount of clinopyroxene, are either heterogeneously or homogeneously distributed in the dikes. In the former case, phenocrysts are symmetrically concentrated in the center, and their abundance gradually decreases towards the margin (Table 2-1, Figs. 2-2a, 2-2b, and 2-2c). The phenocrysts show shape-preferred orientation exclusively in the marginal zone with elongate axes lying nearly parallel to the dike wall (Fig. 2-2c). In the latter case, the homogeneously distributed phenocrysts show less distinct shape-preferred orientation in the dikes.

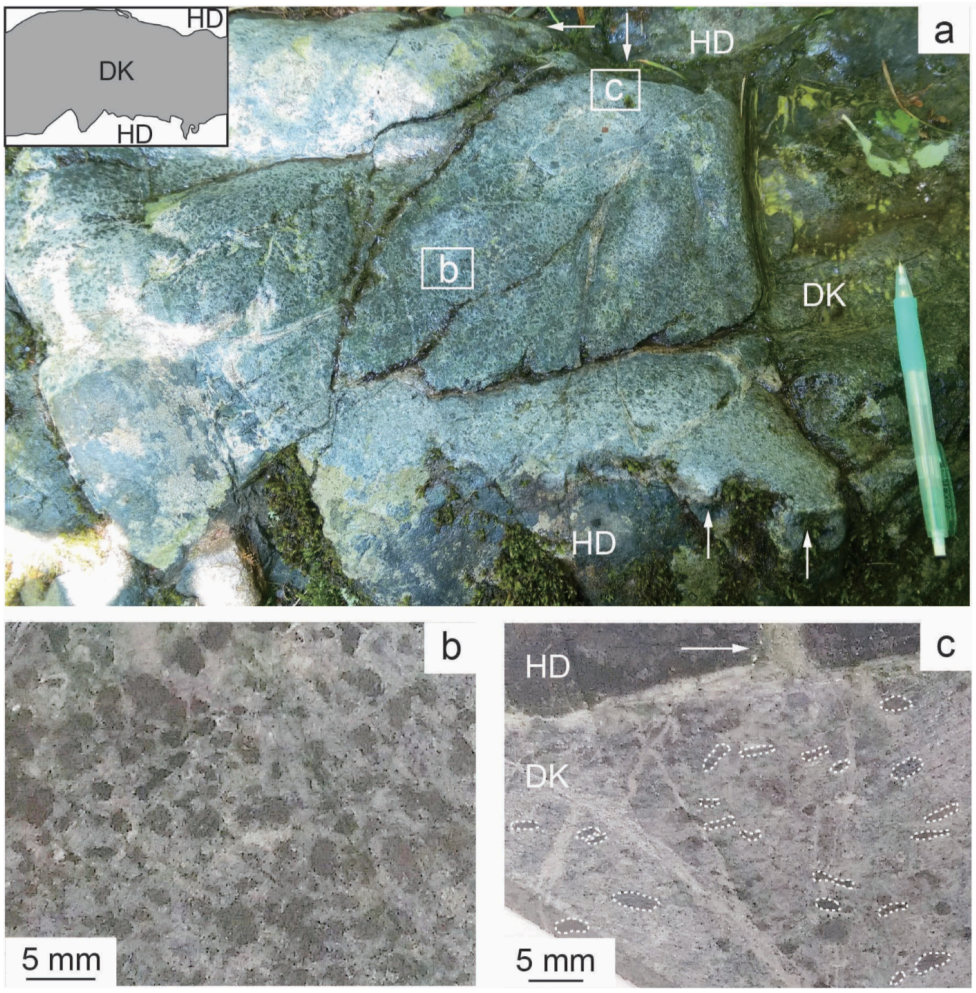

Fig. 2-2: (a) Field occurrence of the ultramafic dike (DK) in the host dunite (HD) at locality #1 in Fig. 2-1b. The inset in the upper left corner shows an outline of the dike. This dike shows porphyritic texture with olivine (dark spots) and minor clinopyroxene phenocrysts set in the matrix. It shows zoning in phenocryst modes; olivine phenocrysts are abundant in the central darker zone and fewer in the brighter marginal zones. The dike has short branches, indicated with arrows. (b): A view of a polished slab taken from the central part of the dike (a rectangle marked with b in (a)) showing abundant phenocrysts (~ 46 vol%; Table 2-1) with euhedral-subhedral morphology. (c): A view of a polished slab in the marginal part of the dike (a rectangle marked with c in (a)) showing a smaller amount of phenocrysts (~20 vol%; Table 2-1) and their shape-preferred orientation (outlined with white dashed lines) elongate parallel to the contact. A few millimeter-thick branch, shown with a white arrow, is present.

These facts clearly show that the magmas intruded into the solid host rocks of the Cumulate Member have solidified as dikes or veins. The Cumulate Member is the latest main lithology in the evolution of the Hayachine-Miyamori ophiolite before the formation of hornblende-bearing mafic-ultramafic intrusive rocks (Ozawa et al., 2015). The formation of the ultramafic intrusive rocks, "ultramafic dikes" hereafter, is one of the latest events in the ophiolite evolution. We found five outcrops of this type of intrusive rocks (Fig. 2-1b) and collected samples from four thick dikes at four outcrops, two of which are covered with river gravels of a recent flooding and only rootless blocks are available.

2.4 Petrography

The absence of chilled margins near the contact with their hosts suggests that the intrusion took place at a fairly high temperature and possibly at high pressure, which must be clarified. Moreover, the dikes contain secondary minerals locally forming veins, which sharply cut the primary igneous textures. This indicates that the dikes may have undergone secondary processes such as metamorphism and/or alteration, which could have modified the igneous chemical and textural features. In this section, we describe petrographic features related to igneous processes first to clarify the intrusion environment, and then describe secondary features in order to evaluate the effect of secondary processes.

2.4.1 Igneous textures

Phenocrysts in the dikes are composed mainly of euhedral - subhedral olivine with a subordinate amount of euhedral clinopyroxene, which is absent in some dikes (Table 2-1). The

size of phenocrysts is up to a few millimeters (Figs. 2-2b and 2-3a). Olivine is partially preserved everywhere in the dikes which show a homogeneous phenocryst distribution, though the extent of replacement with serpentine is variable (Table 2-1). Olivine is preserved at the margin and in the center but not at the edge of the dikes which show a central phenocryst concentration (Table 2-1). There is a tendency that the matrix-dominant lithology is more susceptible to secondary processes and form hydrous phases such as serpentine and chlorite. The olivine phenocrysts locally include chrome spinel and are partially rimmed by orthopyroxene (Figs. 2-3a, 2-3b, and 2-4).

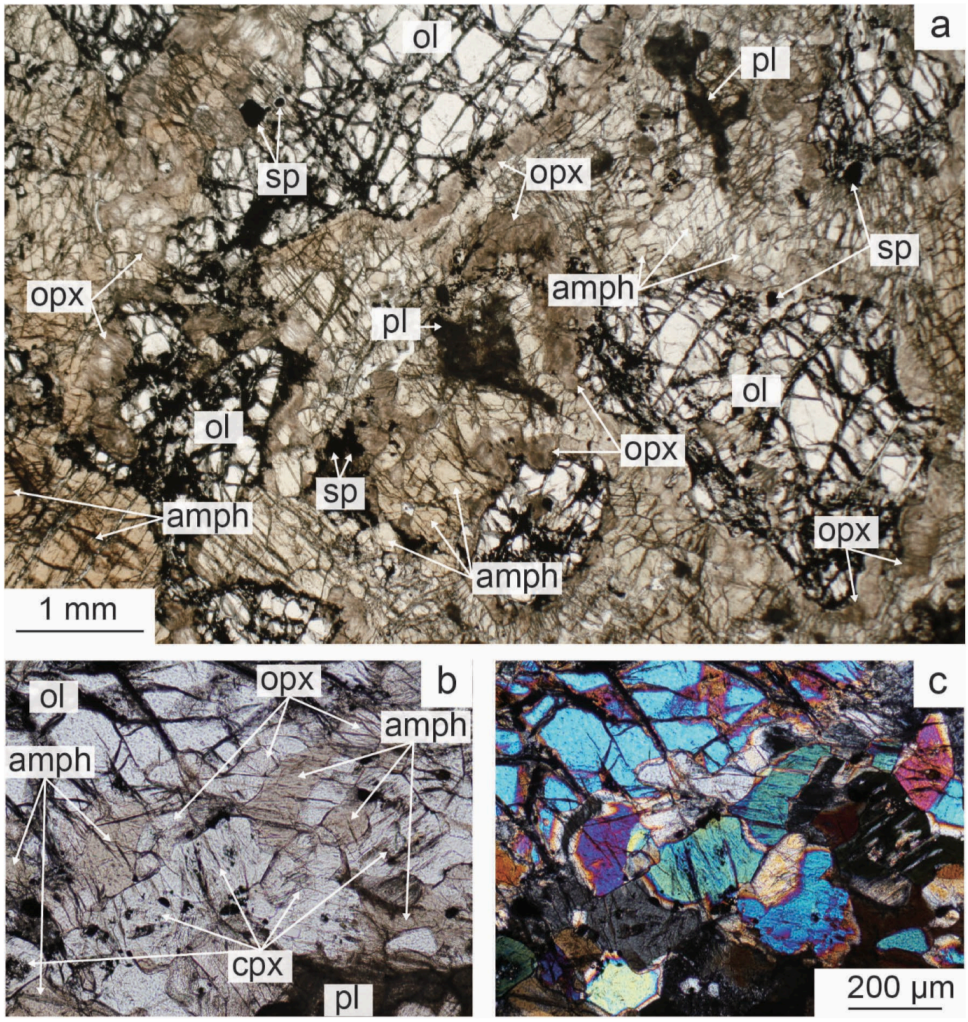

Fig. 2-3: Photomicrograph of thin sections made from ultramafic dikes (DKSH2 and RYO1): (a) Wide view of the center of DKSH2 in an open nicol, (b) magnified view of the area between an olivine phenocryst and a plagioclase pseudomorph in RYO1 under open nicol, and (c) that under crossed nicols. In (a), olivine (ol) phenocrysts are euhedral to subhedral and set in the matrix consisting mostly of polycrystalline amphibole (amph). Orthopyroxene (opx), partially (or totally) altered into darker fine-grained aggregate, occur rimming olivine, and plagioclase pseudomorph (pl) occur in the middle of the amphibole matrix. Euhedral-subhedral chromian spinel (sp) grains are included in olivine or amphibole. In (b) and (c), orthopyroxene is mostly unaltered and occur rimming the olivine phenocryst.

The matrix filling interstitial part of phenocrysts consists of anhedral amphibole and clinopyroxene with minor chrome spinel and dusty fine-grained aggregate after plagioclase (Table 2-1). Amphibole is the most dominant matrix phase (Table 2-1; Figs. 2-3a, 2-3b, and 2-3c) and its size ranges from several tens of microns to 1 mm. It forms a polycrystalline aggregate of a few millimeters across and is in direct contact with olivine phenocrysts partially intervening thin orthopyroxene rim. The amphibole locally includes euhedral chrome spinel. The clinopyroxene forms equigranular aggregates, which show a patchy distribution in amphibole or plagioclase pseudomorph. The grain size of clinopyroxene is from several tens to hundreds of microns and tends to be smaller than that of amphibole.

All plagioclase crystals are replaced by aggregates of secondary minerals, but the aggregates can be identified as plagioclase pseudomorphs as explained below. The plagioclase pseudomorphs, up to a few millimeters across, are present only in the center of dikes (Table 2-1). The pseudomorphs show an anhedral outline, occur in the middle of polycrystalline amphibole, and are locally in contact with clinopyroxene, but are never in direct contact with olivine (Figs. 2-3a, 2-3b, and 2-3c). Such features of plagioclase occurrence are the same as those observed in plagioclase-bearing peridotites of the Cumulate Member (Ozawa, 1986). Spinel shows two different modes of occurrence, which is intimately related to the color difference under an optical microscope which reflects chemical compositions. Brownish chromite spinel is euhedral to subhedral with grain sizes up to 1 mm. It is either included in olivine or occurs in amphibole aggregates. Greenish aluminous spinel showing anhedral and locally vermicular morphology occurs in amphibole surrounding plagioclase (Fig. 2-4). The texture is essentially the same as that of a reaction zone consisting of an inner zone of aluminous spinel-pargasite symplectite and an outer zone of orthopyroxene around plagioclase in plagioclase-bearing wehrlite of the Cumulate

member (Ozawa, 1986). The texture suggests a reaction between olivine phenocrysts and fractionated interstitial melt after or during the crystallization of plagioclase from the interstitial melt, which may have taken place in the last stage of solidification of the dikes at the same pressure estimated for the Cumulate Member formation, ~0.6 ± 0.1 GPa (Ozawa et al., 2015).

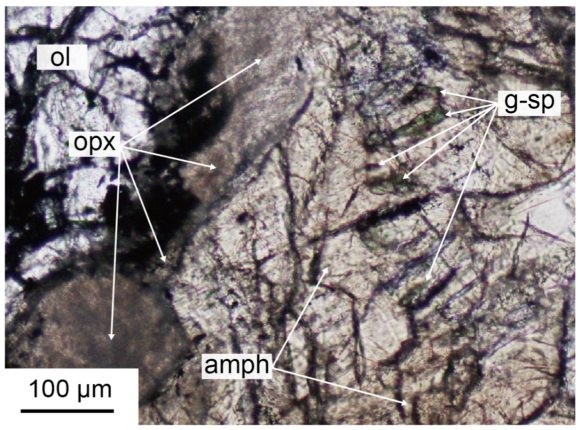

Fig. 2-4: Photomicrograph (open nicol) of a thin section made from DKSH2. Orthopyroxene (opx) is totally altered into darker fine-grained aggregate. Anhedral green spinel (g-sp) grains are vermicular in morphology and included in amphibole grains (amph).

Orthopyroxene exclusively occurs rimming olivine phenocrysts with thickness of a few hundred μm (Figs. 2-3a, 2-3b, and 2-4) and is less abundant near the edge of dikes than in the dike center (Table 2-1). The dikes have a selvage of orthopyroxene aggregates with a thickness of ~ 0.1 mm along the contact with the host peridotite. The same relationship between pyroxenite dikes and harzburgite host was reported from the Tectonite Member by Ozawa (1994), who attributed the texture to a reaction of hydrous melt transported through fractures with the wall rock under heat loss. The same textural relationship between the olivine phenocrysts with

orthopyroxene rim suggests a reaction between the olivine crystals and a magma flowing through fractures before its complete solidification filling the fractures as dikes. The systematic spatial variation of the thickness of orthopyroxene rim on olivine phenocrysts suggests a more extensive reaction in the dike center than in the margin. There are no vesicles or miarolitic cavities, suggesting that no vesiculation occurs during the solidification of the dikes (Figs. 2-2a, 2-2b, and 2-3a).

Table 2-1: Whole-rock chemical compositions, igneous modal compositions, alteration degrees of examined ultramafic dikes.

Dike	DKSH1			DKSH2					RYO1	RYO2
Locality no.	#1			#2					#3	#4
Phenocryst distribution	zoned [1]			homogeneous					homogeneous	zoned [1]
Position	edge	margin	center	edge	margin		center		rootless rock	rootless rock
Sample	DKSH1ES	DKSH1MI	DKSH1CI	DKSH2EI	DKSH2MI	DKSH2MW	DKSH2CI	DKSH2CW	RYO1I	RYO2I
(wt%)										
SiO_2	40.14	41.63	42.59	42.86	42.76	42.62	42.81	42.53	43.41	41.22
TiO_2	1.07	0.44	0.45	0.68	0.69	0.66	0.76	0.62	0.56	0.56
Al_2O_3	6.55	5.90	4.32	4.24	5.27	7.50	4.64	7.39	7.43	8.42
Fe_2O_3	13.82	12.24	11.83	11.23	11.17	11.50	11.38	11.43	9.98	9.32
MnO	0.15	0.19	0.23	0.19	0.18	0.17	0.19	0.18	0.18	0.21
MgO	25.24	29.75	31.67	32.38	30.31	27.99	30.97	28.13	22.25	19.38
CaO	13.01	9.64	8.86	8.39	9.43	8.61	9.15	8.79	15.94	20.86
Na_2O	0.01	0.16	0.03	0.00	0.14	0.83	0.06	0.81	0.23	0.00
K_2O	0.01	0.03	0.02	0.02	0.03	0.11	0.03	0.11	0.01	0.00
P_2O_5	0.01	0.01	0.01	0.01	0.01	0.01	0.01	0.01	0.03	0.03
Total	100.00	100.00	100.00	100.00	100.00	100.00	100.00	100.00	100.00	100.00
Loss on ignition	6.26	5.22	5.40	6.35	5.43	2.72	6.10	3.02	4.39	5.87
(ppm)										
Ni	599	927	983	943	919	836	931	780	498	379
Cr	1406	1588	1729	1570	1457	1376	1534	1277	1529	1371
Ba	96	110	101	98	119	112	104	133	94	93
U	0.04	0.01	0.08	0.02	0.04	0.13	0.04	0.08	0.02	0.01
Nb	1.22	0.48	0.63	0.89	1.09	1.35	1.30	1.11	0.60	0.73
Ta	0.07	0.03	0.04	0.06	0.07	0.07	0.09	0.07	0.06	0.05
La	1.68	1.44	1.48	0.93	1.07	1.07	1.40	1.06	1.05	0.74
Ce	4.08	3.17	3.11	2.90	3.25	3.15	4.05	3.08	2.78	2.59
Pr	0.81	0.52	0.48	0.58	0.61	0.62	0.76	0.59	0.53	0.48
Pb	0.34	0.30	0.32	0.61	0.86	0.86	1.04	0.79	1.85	0.87
Sr	309	146	146	175	195	198	164	223	87	70
Nd	4.90	2.61	2.53	3.66	3.97	4.00	4.40	3.58	3.37	3.18
Hf	0.91	0.47	0.49	0.63	0.68	0.68	0.76	0.62	0.68	0.58
Zr	20.45	13.20	13.73	14.99	16.45	17.20	20.13	16.44	16.89	14.47
Sm	1.83	0.82	0.87	1.26	1.41	1.30	1.46	1.19	1.20	1.27
Eu	0.71	0.36	0.42	0.40	0.50	0.52	0.63	0.48	0.44	0.50
Gd	2.58	1.27	1.26	1.71	1.84	1.77	2.07	1.69	1.72	1.69
Tb	0.45	0.21	0.20	0.28	0.31	0.30	0.34	0.27	0.28	0.30
Dy	3.03	1.48	1.54	1.97	2.07	2.01	2.42	1.87	1.92	2.09
Y	15.09	7.86	8.12	9.99	10.69	10.33	12.31	9.63	10.57	9.94
Ho	0.62	0.31	0.31	0.40	0.42	0.40	0.48	0.39	0.40	0.44
Er	1.73	0.88	0.90	1.13	1.20	1.15	1.38	1.06	1.17	1.17
Tm	0.24	0.12	0.13	0.15	0.17	0.16	0.19	0.15	0.15	0.15
Yb	1.55	0.83	0.83	1.01	1.12	1.08	1.27	0.97	0.98	1.00
Lu	0.22	0.12	0.12	0.15	0.16	0.16	0.18	0.15	0.14	0.15
Modal composition (vol%)										
Phenocrysts										
olivine	14.00	25.67	31.19	34.83	25.31		27.18		14.20	7.65
orthopyroxene [2]	3.50	14.01	11.76	2.52	13.07		10.95		9.03	12.24
clinopyroxene	2.46	1.38	2.75	-					7.53	4.12
Total	19.96	41.06	45.70	37.35	38.38		38.13		30.76	24.01
Matrix										
amphibole	36.77	41.49	41.14	60.66	56.50		54.52		29.79	18.82
clinopyroxene	36.01	14.20	7.61	0.13	1.87		2.34		15.71	24.41
orthopyroxene	-			1.32	-		-		3.91	7.17
plagioclase	-	1.72	2.69	-	2.02		2.40		18.41	25.29
spinel	7.26	1.52	2.87	0.53	1.23		2.61		1.42	0.29
Total	80.04	58.94	54.30	62.65	61.62		61.87		69.24	75.99
Extent of replacement by secondary low-temperature minerals [3]										
Overall	strong	intermediate	intermediate	intermediate	intermediate	weak	intermediate	weak	intermediate	intermediate
Phenocrysts										
olivine	×	○	○	○	○	○	○	○	△	△
orthopyroxene	×	×	×	×	×	△	×	△	○	○
clinopyroxene	△	○	○	-	-	-	-	-	○	○
Matrix										
amphibole	×	×	×	×	×	○	×	○	△	△
clinopyroxene	△	○	○	○	○	○	○	○	○	○
orthopyroxene	-	-	-	×	-	-	-	-	○	○
plagioclase	-	×	×	-	×	×	×	×	×	×
spinel	△	○	○	○	○	○	○	○	○	○

[1] Phenocrysts are concentrated in the dike center.

[2] Orthopyroxene always occurs rimming olivine phenocrysts.The original modal abundance of olivine phenocryst is thus olivine + orthopyroxene rim

[3] ○, weak (< 20 %); △, intermediate (20 - 60 %); ×, extensive (60 - 100 %).

2.4.2 Textures related to secondary low-temperature processes

Igneous textures were modified in various degrees by low-temperature processes, which are defined in this paper as low-temperature (< ~700 °C) metamorphism and/or alteration with introduction of fluids to form hydrous phases such as serpentine, chlorite, and tremolite associated with crystallization of magnetite and spindle-shaped diopside. We hereafter use "alteration" to denote this process. The orthopyroxene is partially (or totally) replaced by fine-grained aggregates of tremolite and diopside while keeping the primary grain outline (orthopyroxene pseudomorph; Fig. 2-3a) in samples taken from outcrop (DKSH1 and DKSH2). Some rootless rocks from the dikes (RYO1 and RYO2), however, have fresh orthopyroxene (Figs. 2-3b and 2-3c). The aggregates of tremolite and diopside are partly replaced by chlorite. Amphibole is less susceptible to the alteration, but is replaced by tremolite, diopside, chlorite, and serpentine particularly at the dike margin. Plagioclase pseudomorph consists of fine-grained grossular, but the original outline of plagioclase is preserved. In spite of the complete replacement, the origin of the grossular aggregate as plagioclase is supported by its trace element patterns, which are shown below. Olivine phenocrysts are replaced partially or completely by serpentine and magnetite. Such replacement is limited in fresh samples to the formation of serpentine and magnetite along minor fractures in olivine (Figs. 2-3a and 2-3b). These textures suggest multistage open-system alteration reactions after the complete solidification of the dike.

The extent of the replacement of each primary mineral by secondary phases was qualitatively evaluated under an optical microscope, and three levels of alteration were distinguished: weak, intermediate, and extensive (Table 2-1). This information was used to classify alteration degrees of the samples into weak, intermediate, and strong (Table 2-1). The

one sample with strong alteration is from the edge of dike DKSH1. Weakly altered samples are from the marginal and central parts of dike DKSH2, which was used to examine alteration processes in detail. A more quantitative parameter for alteration is the mass loss on ignition, which is described below.

2.5 Analytical methods

Several slabs were obtained sequentially from the center to edge of two dikes DKSH2, which has a homogeneous phenocryst distribution, and DKSH1, which shows a high concentration of phenocrysts in the center (Table 2-1; Figs. 2-2a and 2-2b). Two samples of rootless blocks from locality #3 (RYO1) with a homogeneous phenocryst distribution and locality #4 (RYO2) with a zoned phenocryst distribution at sample scale (~15 cm) were also examined (Table 2-1). Each slab sample (100 - 150 g) was rinsed for 15 minutes in deionized water and methanol using an ultrasonic vibrator and was dried in an oven at 80 °C for 12 hours. The dried slab samples were crushed to chips of ~5 mm diameter by a tungsten mortar. The chips were crushed to powder by the rod mill: Retsch Vibratory Disc Mill RS 200 with an agate rod for several minutes. The powder samples of 1.5 - 2.0 g were put in the oven and heated at 120 °C for 12 hours to outgas the absorbed water. Following this procedure, the powder samples were ignited in a programable multistage heater in a Muffle Furnace of Yamato FO510 to outgas the water and other volatile components in the crystal structures at several temperatures and for the respective durations: 100 °C for 10 minutes, 500 °C for 30 minutes, 800 °C for 30 minutes, and 1000 °C for 6 hours. The mass loss including water in samples is regarded as a loss on ignition (LOI in wt%). Thin section observation of the examined samples shows that only a

minor amount of carbonates and sulfides are present (< ~2 vol% in total). Therefore, the contribution of these minerals to the LOI is negligible.

Major and trace element concentrations of the whole-rock samples were measured with an X-ray Fluorescence Spectrometer (XRF): PANalytical Axio at the Department of Earth and Planetary Science, the University of Tokyo by the glass bead method for major elements and the pressed powder method for trace elements. The analytical procedures have been described by Yoshida and Takahashi (1997). The glass beads were prepared as follows. The powder samples and the flux of anhydrous lithium tetraborate were weighed 0.4 g (< 0.1 % in error) and 4 g (< 0.1 % in error), respectively and were mixed. The mixed powder and a drop of lithium iodide were put in a platinum crucible and heated with a fuse sampler, Tokyo Kagaku TK−4100, to obtain glass bead.

Major element concentrations in minerals were measured with an electron probe microanalyzer (EPMA; JEOL JXA−8900L), at the Department of Earth and Planetary Science, the University of Tokyo. The adopted analytical conditions for olivine, pyroxene, amphibole, and spinel are: a focused beam, an acceleration voltage of 15 kV, a beam current of 12 nA on a Faraday cup, and 30 s counting time for peak and 15 s for background on both sides of each peak. The beam diameter of 50 μm is adopted for analyses of the core of plagioclase pseudomorph replaced by fine-grained mineral aggregates to obtain the bulk composition. We adopted an acceleration voltage of 25 kV and a beam current of 50 nA on a Faraday cup and 100 s counting time for peak and 50 s for background on both sides of each peak for trace elements in olivine (NiO and MnO). The correction method to obtain wt% from peak intensity after correcting background is ZAF.

Trace elements in the whole-rock samples were measured on the glass beads prepared for the XRF analyses with a Thermo Fisher Scientific iCAP Q inductively coupled plasma mass spectrometer (ICP-MS) coupled with a CETAC LSX-213 G2+ Nd:YAG laser ablation (LA) system at the Department of Earth and Planetary Science, the University of Tokyo. The analytical procedures described by Itano and Iizuka (2017) were adopted. The glass beads were cut vertically into the disks and the cut surface was polished with diamond paste (1μm size). The laser beam with a spot size of 50 μm, a shot frequency of 10 Hz, and a scan rate of 5 μm/s in line analysis were used. Analyzed elements are Ca, Cr, Mn, Ni, Sr, Y, Zr, Nb, Ba, La, Ce, Pr, Nd, Sm, Eu, Gd, Tb, Dy, Ho, Er, Tm, Yb, Lu, Hf, Ta, Pb, and U. The obtained signal intensities of trace element data were corrected for gas blank, and calibrated against NIST SRM 613 (Hollocher and Ruiz, 1995). Trace element concentrations on each sample were normalized using the Ca concentrations of the glass beads measured with XRF as an internal standard.

Trace element concentrations of amphibole and clinopyroxene in thin sections samples polished with diamond paste (1 μm size) were measured with the LA-ICP-MS. Focused-laser with a spot size of 40 μm and a shot frequency of 5 Hz were used. The integration time is 60 seconds, including 20 seconds gas blank measurement. Analyzed elements are Ca, Sr, Y, Zr, Nb, Ba, La, Ce, Pr, Nd, Sm, Eu, Gd, Tb, Dy, Ho, Er, Tm, Yb, Lu, Hf, Ta, Pb, and U. The correction procedures of obtained signal intensities are basically the same as those adopted for the whole-rock analyses described above. The Ca concentration measured by EPMA on each analysis spot was used as an internal standard.

Nd and Sr isotope ratios in the whole-rock samples and clinopyroxenes were measured with a Thermo Fisher Scientific Neptune plus multiple collector ICP−MS at the Graduate School

of Science, Hokkaido University. Clinopyroxene grains were carefully handpicked from coarsely crushed samples of the ultramafic dikes under a binocular microscope. They were powdered by an agate mortar. The analytical procedures for chemical separation followed the methods used in Pin et al. (1994) and Noguchi et al. (2011) for Sr, Pin et al. (1994) and Pin and Zalduegui (1997) for Nd. Mass fractionation factors for Sr and Nd were calculated using $^{86}Sr/^{88}Sr = 0.1194$ and $^{146}Nd/^{144}Nd = 0.7219$, respectively. Additional corrections were performed by applying a standard bracketing method using NIST987 and JNdi-1 for Sr and Nd isotopic analyses, respectively. The data were finally normalized to $^{87}Sr/^{86}Sr = 0.710214$ for NIST 987, and $^{143}Nd/^{144}Nd = 0.512117$ for JNdi-1. The isotopic ratios of the GSJ standard JB-3, measured during the course of this study, were $^{87}Sr/^{86}Sr = 0.703384 \pm 0.000024$ (n = 32, 2σ), $^{143}Nd/^{144}Nd = 0.513065 \pm 0.000011$ (n = 23, 2σ). The Rb/Sr and Sm/Nd ratios of whole-rock samples were measured by ICP-MS using a Thermo Fisher X-series at the Graduate School of Science, Hokkaido University. The analytical uncertainties are typically 0.7 % for the Rb/Sr ratios and 0.5 % for the Sm/Nd ratios.

2.6 Whole-rock chemistry

2.6.1 Major elements

The whole-rock major element oxide contents including the loss on ignition (LOI) of dike samples are listed in Table 2-1. The MgO contents of the slab samples vary from 19.4 to 32.4 wt%, Al_2O_3 from 4.2 to 8.4 wt%, Fe_2O_3* (total Fe as Fe_2O_3) 9.3 to 13.8 wt% and the LOI from 2.7 to 6.4 wt%. (Table 2-1, Fig. 2-5). The weakly altered samples from dike DKSH2 show lower values of LOI than the extensively altered samples, though they have the same igneous modal compositions (Table 2-1).

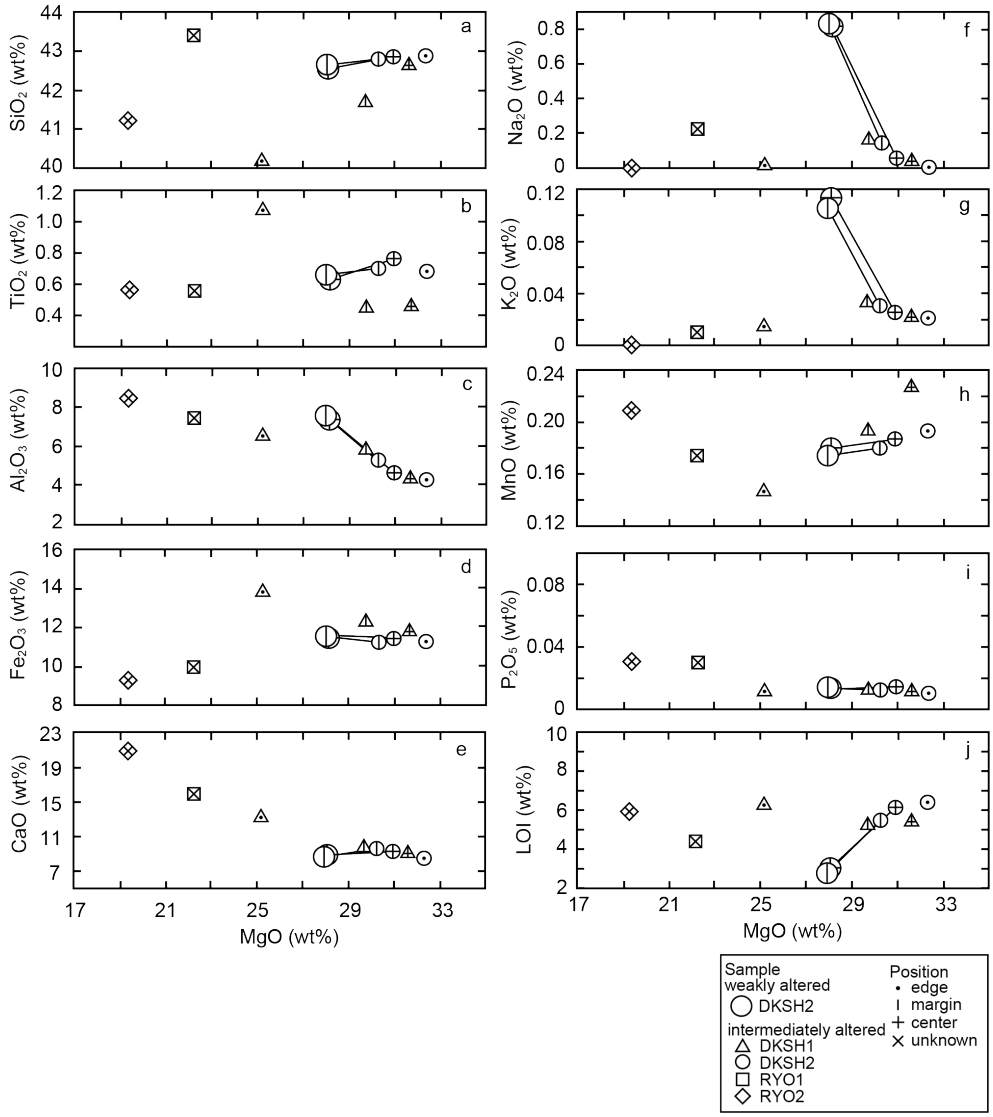

Fig. 2-5: Whole-rock SiO_2, TiO_2, Al_2O_3, Fe_2O_3, CaO, Na_2O, K_2O, MnO, and P_2O_5 contents and loss on ignition (LOI) in wt% of examined samples of dikes plotted against MgO wt%. Triangles, circles, squares, and diamonds indicate examined dikes: DKSH1, DKSH2, RYO1, and RYO2, respectively (Fig. 2-1b; Table 2-1). Symbols with a dot, vertical line, plus, and cross denote samples from the edge, margin, and center of dikes, and rootless block without information on sample position in the dike, respectively. Large symbols indicate weakly altered, and small symbols indicate samples showing intermediate or strong alteration. The solid lines connect two pairs of samples with different degrees of alteration, but the other features, such as sampling location in the dike and igneous modal abundance, are the same.

2.6.2 Rare earth and other trace elements

The whole-rock concentrations of rare earth element (REE) and other trace elements of dike samples are listed in Table 2-1. The CI-chondrite normalized trace element and REE patterns of the samples are plotted in Figs. 2-6a, 2-6b, 2-6c, and 2-6d. The dikes have essentially the same trace element patterns, which are characterized by strong positive anomalies of Ba and Sr, a strong negative anomaly of Pb, and weak negative anomalies of Hf and Zr relative to the REEs, and U, Nb, Ta lying on a smooth extension of the REE variations (Fig. 2-6a). The REE patterns are essentially the same for all samples and are characterized by smooth overall variations: a depletion of light rare earth elements (LREE), and a weak depletion of heavy rare earth elements (HREE) (Figs. 2-6c and 2-6d). The abundances of REEs in the dikes having homogeneous phenocryst distributions are nearly constant (Fig. 2-6c), but those of the dikes having a central enrichment of phenocrysts are high in the edge and margin and low in the center while keeping the same variation pattern (Fig. 2-6d).

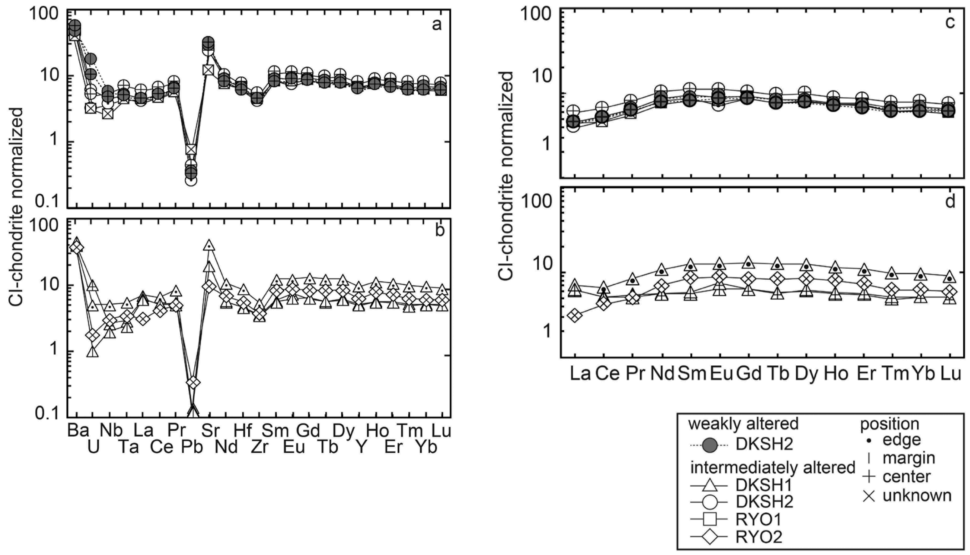

Fig. 2-6: CI-chondrite normalized whole-rock trace element and rare earth element (REE) patterns of 10 samples from 4 dikes (Fig. 2-1b, Table 2-1). Six samples are from dikes with homogeneous phenocryst distribution, shown in (a) and (c), and four samples from dikes zoned in terms of phenocryst abundance, shown in (b) and (d). The CI-chondrite composition is after McDonough and Sun (1995). Triangles, circles, squares, and diamonds indicate examined dikes: DKSH1, DKSH2, RYO1, and RYO2, respectively. Symbols with a dot, vertical line, plus, and cross denote samples from the edge, margin, and center of dikes, and rootless block without information on sample position in the dike, respectively. Shaded symbols with a dashed line indicate samples with a weak alteration.

2.6.3 Isotope ratios

The whole-rock $^{87}Sr/^{86}Sr$ and $^{143}Nd/^{144}Nd$ ratios of samples from four dikes are listed in Table 2-2 and are plotted in Fig. 2-7. The $^{143}Nd/^{144}Nd$ ratios are similar irrespective of localities and positions within each dike and range from 0.512975 to 0.513079. There is a systematic difference of Sr isotopes depending on the degree of alteration in samples from dike DKSH2, as

shown in Fig. 2-7a. The strongly and intermediately altered samples with high LOI have higher ^{87}Sr / ^{86}Sr ratios than the less altered samples with low LOI. The lines that join samples with different degrees of alteration in the $^{87}Sr/^{86}Sr$ and $^{143}Nd/^{144}Nd$ diagram (Fig. 2-7a) are nearly horizontal, which indicates that secondary processes shifted $^{87}Sr/^{86}Sr$ to higher values but did not affect the Nd isotope ratios. The least altered samples of the dikes with homogeneous phenocryst distribution (DKSH2MW and DKSH2CW) have low ^{87}Sr / ^{86}Sr ratios, which are thought to represent the primary values before the alteration. The range of the initial εNd of four dikes and the values of the initial $^{87}Sr/^{86}Sr$ of DKSH2MW and DKSH2CW are 6.0 - 7.1 and ~0.7032, respectively and plot just at the lower end of the Cambrian-Ordovician mid-ocean ridge basalt (MORB) field (Yoshikawa and Nakamura, 2000; εNd, 7 - 12; ^{87}Sr / ^{86}Sr, 0.7018 - 0.7027).

Table 2-2: Sm–Nd and Rb–Sr isotopic compositions of selected samples from four ultramafic dikes.

Dike	Sample	$^{87}Rb/^{86}Sr$	$^{147}Sm/^{144}Nd$	$^{143}Nd/^{144}Nd$		$^{87}Sr/^{86}Sr$		Sr_I [1]	εNd_I [1]
					2σ (10^{-6})		2σ (10^{-6})		
Whole rock									
DKSH1	DKSH1ES	0.0023	0.224	0.513031	4.7	0.703511	9.8	0.703495	6.0
	DKSH1MI	0.0063	0.199	0.512975	7.9	0.703432	12.8	0.703387	6.4
	DKSH1CI	0.0026	0.200	0.512986	9.1	0.703458	12.4	0.703440	6.6
DKSH2	DKSH2EI	0.0013	0.202	0.513020	5.8	0.703498	12.0	0.703489	7.1
	DKSH2MI	0.0019	0.204	0.513021	5.9	0.703432	14.1	0.703419	7.0
	DKSH2MW	0.0070	0.212	0.513021	5.3	0.703219	9.0	0.703169	6.5
	DKSH2CI	0.0027	0.204	0.513009	5.7	0.703456	8.8	0.703437	6.8
	DKSH2CW	0.0091	0.211	0.513013	5.8	0.703234	10.8	0.703169	6.4
RYO1	RYO1I	0.0121	0.215	0.513047	6.6	0.703693	9.9	0.703607	6.8
RYO2	RYO2I	0.0177	0.225	0.513079	7.6	0.703955	15.6	0.703829	6.8
Separated clinopyroxene									
RYO1	CPXRYO1I	0.0075	0.228	0.513055	6.8	0.703701	12.4	0.703648	6.1

[1] Sr_I and εNd_I are initial $^{87}Sr/^{86}Sr$ and initial $^{143}Nd/^{144}Nd$, respectively at 499Ma (Ozawa et al., 2015).

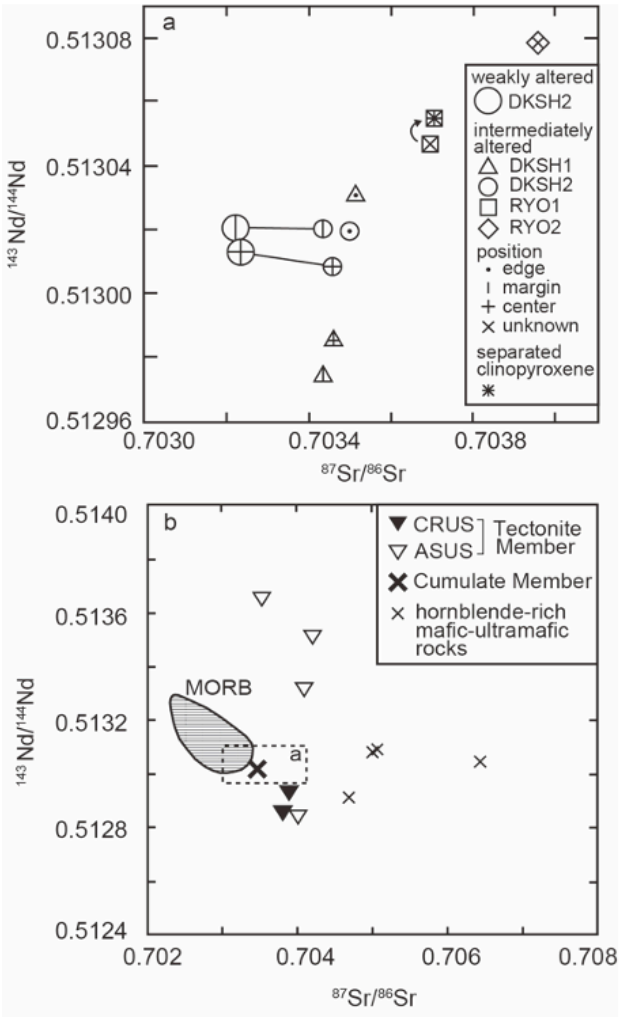

Fig. 2-7: Present-day values of $^{87}Sr/^{86}Sr$ and $^{143}Nd/^{144}Nd$ of whole-rocks and separated clinopyroxene phenocrysts for examined 4 ultramafic dikes (a) and other mafic and ultramafic rocks in the Hayachine-Miyamori ophiolite from the literature (b). Symbols and paring lines in (a) are the same as those used in Fig. 2-5 except for star in the square, which denotes clinopyroxene separated from a sample indicated by arrows. Plotted in (b) are literature data for pyroxenes separated from the chromite-bearing Ultramafic Suite (CRUS) (solid inverted triangle), aluminous spinel-bearing Ultramafic Suite (ASUS) (open inverted triangle) (Yoshikawa and Ozawa, 2007), the Cumulate Member of the Miyamori complex (thick cross) (Ozawa et al., 2015) and the hornblende-rich mafic-ultramafic rocks (cross) (Shibata and Ozawa, 1992). The rectangle in (b) represents the plot region of (a). The area for mid-ocean ridge basalt (MORB) in (b) is according to the compilation by Yoshikawa and Nakamura (2000).

2.7 Mineral chemistry

Cation ratios of minerals are abbreviated as follows: Mg# = Mg/(Mg + Fe^{2+}), Cr# = Cr/(Cr + Al). The total iron is assumed to be Fe^{2+}, except for spinel, orthopyroxene, clinopyroxene and amphibole, for which ferric iron contents were calculated from stoichiometry constraints with charge balance considerations. The procedure for amphibole is from Leake et al. (1997).

2.7.1 Olivine

Olivine in the dikes and their host peridotites is homogeneous in Mg# on a grain scale (a few millimeters). A variation in Mg# on the scale of 10 cm is, however, observed not only in the dikes but also in the host peridotites. This is well documented in dikes with a homogeneous phenocryst distribution as shown in Fig. 2-8 for dike DKSH2 because of the limited alteration near the contact. The Mg# decreases from 0.90 to 0.87 over the distance of 50 mm from the dunite host to the contact and from 0.87 to 0.83 over the distance of 54 mm from the contact to the dike center (Fig. 2-8a). Olivines in the dikes are heterogeneous in NiO content on a grain scale, which is manifested by the larger scatter in composition at a given distance than that of Mg# in Fig. 2-8a. It shows variation across the contact with the host dunite as in the case of Mg# (Fig. 2-8b), but the spatial extent of variation is narrower than that of Mg# (cf. Figs. 2-8a and 2-8b). The average NiO content in olivine at the center of the dike is 0.21 wt% with a standard deviation of 0.01 wt% in 1σ. It is 0.35 wt% with a standard deviation of 0.01 wt% in 1σ in the host dunite.

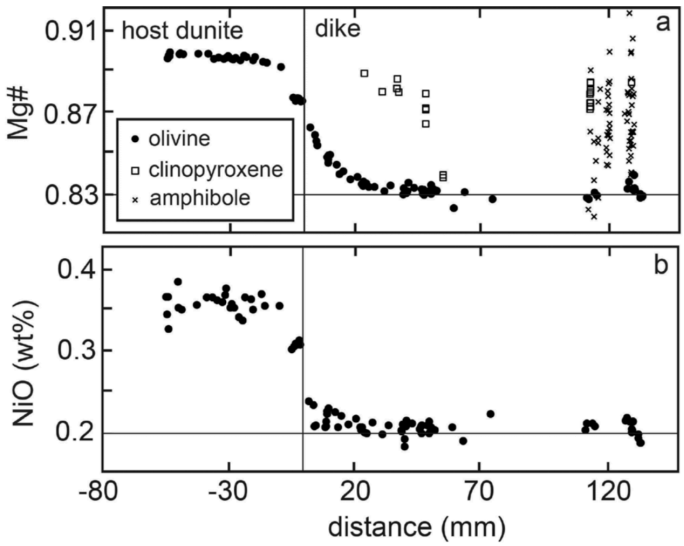

Fig. 2-8: Spatial variations of Mg# of minerals (a) and NiO wt% in olivine (b) crossing the contact between ultramafic dikes and host dunite for DKSH2 (locality #2; Fig. 2-1b). The distance is measured from the boundary taken positive towards the center of the dike and negative towards the dunite host. Vertical lines indicate the positions of the dike-host boundary, where the igneous modal abundance abruptly changes. Horizontal lines indicate the lowest grain-averaged values of the central homogeneous part of DKSH2, which are 0.83 in Mg# and 0.20 wt% in NiO.

2.7.2 Spinel

Spinel is present in all samples and shows diverse chemical composition, particularly in terms of tetravalent cations (Table 2-1; Fig. 2-9). It shows zoning in each grain. Euhedral spinel grains show concentric zoning with decreases in Cr# and $Fe^{3+}/(Cr + Al + Fe^{3+})$ from the core to the rim (see Figs. 2-10a and 2-10b). The Cr# and $Fe^{3+}/(Cr + Al + Fe^{3+})$ vary from 0.37 and 0.14 at the grain center to 0.13 and 0.05 at the rim, respectively. The largest euhedral spinel grain

registers the highest Cr# and $Fe^{3+}/(Cr + Al + Fe^{3+})$ at the core. Subhedral and anhedral spinel grains occurring in adjacent to plagioclase pseudomorphs are rich in Al and poor in Cr and Fe^{3+}. Their Cr# range 0.00 - 0.03 and $Fe^{3+}/(Cr + Al + Fe^{3+})$ 0.01 – 0.02.

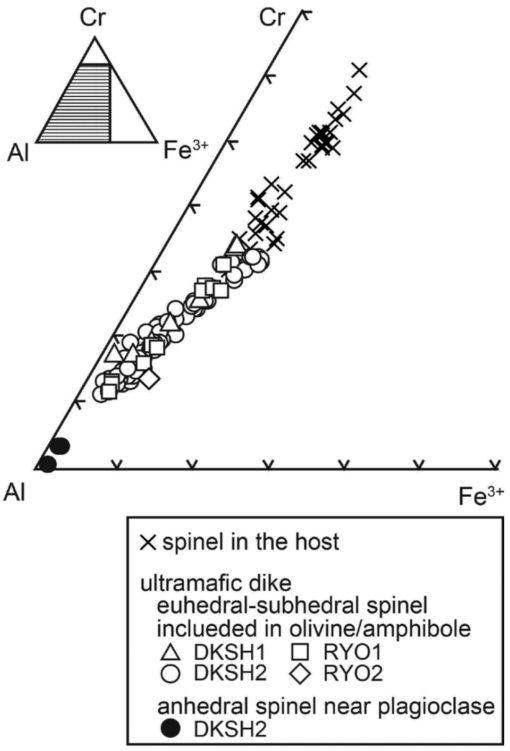

Fig. 2-9: Chemical compositions of spinel plotted in the triangular diagram of Cr, Al, and Fe^{3+} in examined four ultramafic dikes. Triangles, circles, squares, triangles, and diamonds are the same as those used in Fig. 2-5. Open and solid symbols indicate euhedral-subhedral grain included in olivine/amphibole and anhedral grain occurring near plagioclase, respectively. Cross indicates spinel in the host dunite.

The Cr# in large grains of such spinel shows an asymmetric zoning pattern, which increases from the rim closer to plagioclase to the opposite rim (see Figs. 2-10c and 2-10d).

Small green spinel, locally vermicular in morphology, is particularly aluminous, and it is almost Cr-free in an extreme case (Figs. 2-9 and 2-4).

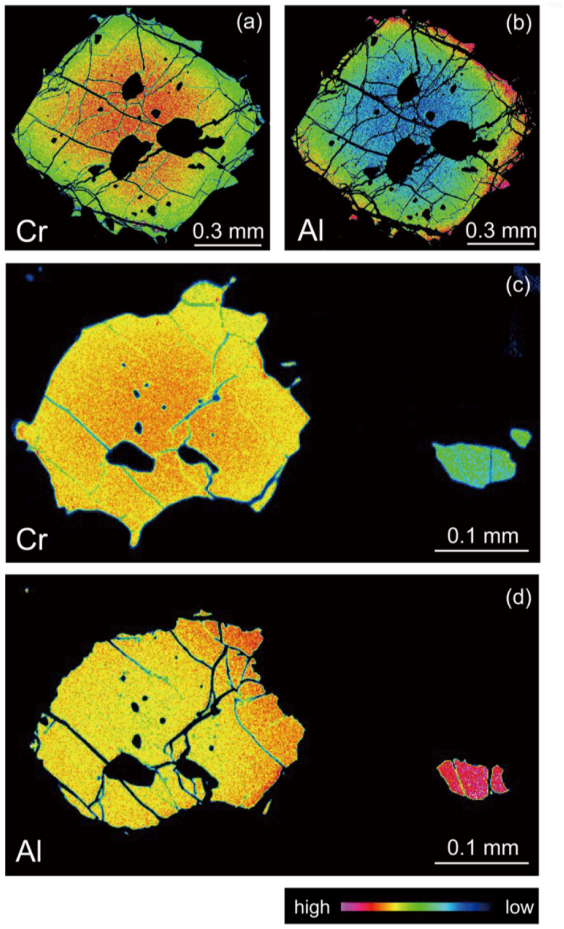

Fig. 2-10: X-ray intensity maps of a euhedral spinel grain for Cr (a) and Al (b) and subhedral to anhedral grains for Cr (c) and Al (d) in dike DKSH2. Black spots in spinel grains are clinopyroxene inclusions. The spinel grains in (c) and (d) occur near a plagioclase pseudomorph, which is 1 mm far right of the smaller grain. Note that the large euhedral spinel grain in (a) and (b) shows a concentric Al-Cr zoning with decreasing Cr# from the core to the rim (from 0.37 at the core to 0.07 at the rim). Note also that the large subhedral spinel grain in (c) and (d) shows asymmetric zoning in Al and Cr with notable enrichment of Al towards the rim closer to the small very Al-rich and Cr-poor spinel grain on the right, which is greenish in color. A part of the small spinel grain is replaced by ferritechromite owing to low-temperature alteration, and is very low in Al with keeping Cr, which results in its disappearance in (d).

2.7.3 Amphibole

Amphibole is present in all the dikes but is completely replaced by secondary minerals near the contact with the host peridotites (Table 2-1). All the amphiboles are classified as pargasite according to Leake et al. (1997) (Fig. 2-11). Amphibole in the dike center is homogeneous in Mg# on a grain scale (~1 mm). The Mg# of amphibole varies from 0.82 to 0.92 depending on the local modal abundance of olivine phenocrysts: the Mg# tends to be higher near olivine phenocrysts. A variation of Mg# across the contact with the host peridotite cannot be clarified because of the complete alteration of amphibole near the contact (Fig. 2-8a). The TiO_2 / K_2O weight ratios of amphibole, shown in Fig. 2-12, are within the range for normal mid-ocean ridge basalts (NMORB) and are similar to the values of ASUS of the Hayachine complex (Ozawa, 1988) and the Cumulate Member of the Miyamori complex (Ozawa et al., 2015). The ratio is clearly distinct from those of CRUS in the Miyamori complex, which is comparable to the ratio of high magnesian andesite (Ozawa, 1988).

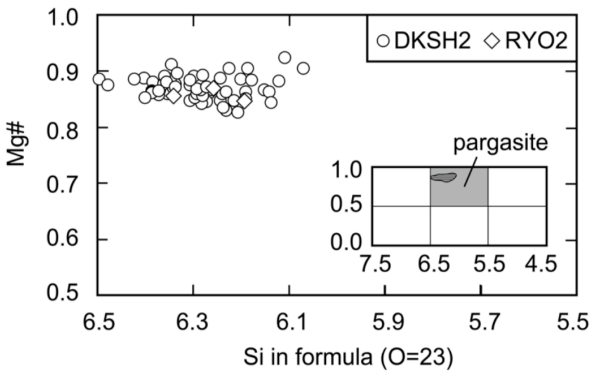

Fig. 2-11: Chemical compositions of amphibole forming the matrix in the examined dikes plotted in classification diagram after Leake et al. (1997). Circle and diamond are the same as those used in Fig. 2-5. They are all classified as pargasite with wide variations in Si (6.0 - 6.5) and Mg# (0.82 - 0.92).

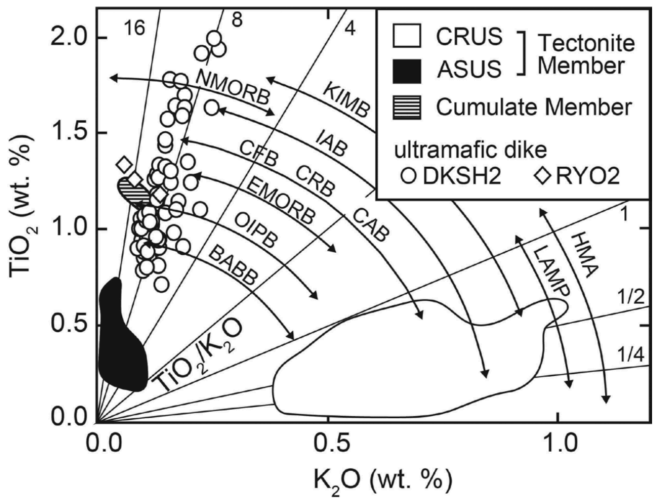

Fig. 2-12: TiO_2/K_2O ratio of amphibole in wt% forming the matrix of examined ultramafic dikes. The data fields for amphibole from the aluminous Spinel Ultramafic Suite (ASUS), the Chromite-bearing Ultramafic Suite (CRUS), and the Cumulate Member (Cumulate) of the Hayachine-Miyamori ophiolite (Ozawa, 1988) are also shown. The ranges of magma compositions from various tectonic settings are after Ozawa (1988). Circle and diamond are the same as those used in Fig. 2-5. The data of amphibole in the ultramafic dikes are plotted in the field of normal mid-ocean ridge basalt. Abbreviations: NMORB, normal mid-ocean ridge basalt; OIPB, oceanic intra-plate basalt; BABB, back-arc basin basalt; EMORB, enriched mid-ocean ridge basalt; IAB, island arc basalt; CFB, continental flood basalt; CRB, continental rift basalt; CAB, continental alkali basalt; KIMB, kimberlite; HMA, high magnesian andesite; LAMP, lamproite.

Chondrite-normalized trace element patterns of 7 amphibole grains in weakly altered samples of dike DKSH2 are plotted in Fig. 2-13a. The patterns have peculiar features of a substantial decline from middle rare earth elements (MREEs) to light rare earth elements (LREEs), a slight decline from MREEs to heavy rare earth elements (HREEs), positive anomalies of some of highly incompatible elements (Ba and Sr), a strong negative anomaly of Pb and weak negative anomalies of Hf and Zr relative to rare earth elements (REEs).

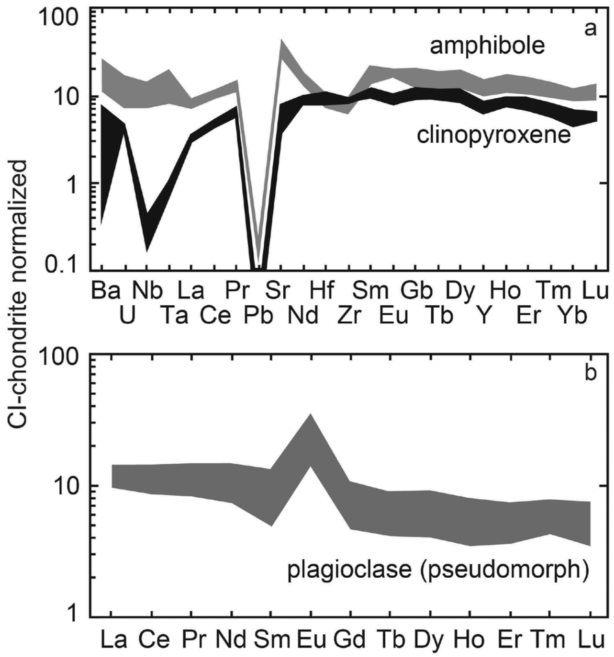

Fig. 2-13: CI-chondrite normalized trace element patterns of clinopyroxene and amphibole (a) and rare earth element (REE) pattern of plagioclase pseudomorph (fine-grained aggregate mostly consisting of grossular) (b) in weakly altered dike DKSH2. These minerals consist of the matrix of olivine and clinopyroxene phenocrysts. The ranges of 7 analyses of amphibole from 2 samples (DKSH2MW and DKSH2CW), 5 analyses of clinopyroxene from 2 samples (DKSH2MW, DKSH2CW), and 4 analyses of plagioclase pseudomorph from 1 sample (DKSH2CW) are shown by filled or shaded areas. The REE pattern of plagioclase pseudomorph in (b) has a remarkable positive Eu anomaly and depletion in heavy REEs, which confirms the plagioclase origin of the aggregate. The CI-chondrite composition is after McDonough and Sun (1995).

2.7.4 Orthopyroxene

Orthopyroxene survived alteration in the least altered dikes (Table 2-1; RYO1 and RYO2) is homogeneous on a few hundred-micrometer scale and has Mg#, Cr#, Al_2O_3 and CaO wt% ranging from 0.82 to 0.84, 0.01 to 0.03, 2.1 to 3.1 wt%, 0.47 to 0.67 wt%, respectively. The spatial chemical variations of orthopyroxene on the scale of ~10cm in the dikes and their host peridotite cannot be clarified because of the extensive alteration.

2.7.5 Clinopyroxene

Clinopyroxene phenocrysts, that occur in some of the dikes (Table 2-1; DKSH1, RYO1, and RYO2), have chemical zoning in terms of Mg#, Cr#, Al_2O_3, and CaO. The core tends to have higher Mg#, Cr#, and lower Al_2O_3, CaO wt% than the rim. The Mg#, Cr#, Al_2O_3, and CaO wt% vary from 0.86 to 0.88, 0.03 to 0.10, 2.9 to 5.1 wt%, 21.4 to 23.5 wt%, respectively. The $^{87}Sr/^{86}Sr$ and $^{143}Nd/^{144}Nd$ ratios of separated clinopyroxene from dike RYO1 are 0.513055 and 0.703701, respectively, which are similar to those of the whole rock (Fig. 2-7a).

The Mg#, Cr#, Al_2O_3 and CaO wt% of matrix clinopyroxenes show variations on a few hundred micrometers scale, ranging from 0.83 to 0.89, 0.03 to 0.08, 2.7 to 4.9 wt%, 21.1 to 23.5 wt%, respectively. The Mg# shows a wide variation from the dike center to the host dunite (Fig. 2-8a), though the variation is not so distinct as exhibited by olivine. This is partly due to the variability of the Mg# depending on the local modal abundance of olivine phenocrysts. Spindle-shaped clinopyroxene, which is inferred to have crystallized during alteration according to its occurrence and morphology, has the highest CaO (~24.4 wt%) and lowest Al_2O_3 (~0.4 wt%) contents and classified as diopside.

Chondrite-normalized trace element patterns of matrix clinopyroxene from weakly altered dike DKSH2 are plotted in Fig. 2-13a. All of 5 analyses are essentially the same except for Ba, which shows a large variation. The trace element patterns are characterized by a depletion of Ta, strong negative anomalies of Pb and Nb. The REE abundance of matrix clinopyroxene is lower than that of the matrix amphibole. Their patterns are distinct in that clinopyroxene has a more sloped CI-chondrite normalized variations of LREEs and HREEs than amphibole.

2.7.6 Plagioclase (pseudomorph)

Trace element patterns of fine-grained aggregate which consist mostly of grossular in a weakly altered sample DKSH2CW are characterized by distinct Eu positive anomaly and depletion of HREEs, which are typical for plagioclase (Fig. 2-13b). This clearly supports that the aggregate is an alteration product of plagioclase (pseudomorph).

2.8 Magma generation condition and mechanism

In this section, after showing that melt compositions are restorable from the dikes, we will take the following steps to estimate magma generation conditions, melting mechanisms, and mantle potential temperatures on the basis of the data presented above. (1) We first restore the original whole-rock compositions for major and trace elements by correcting for alteration modification. (2) We estimate the intruded melt compositions by correcting for subsolidus modifications and olivine accumulation. (3) We estimate primary melt compositions in equilibrium with the mantle by adding olivine to the intruded melts. (4) We use the primary melt compositions to estimate melting mechanism, mantle source composition, melting/melt

segregation conditions, and solidus conditions. (5) We finally estimate mantle potential temperatures. (6) Additionally, we evaluate the openness of the melting system.

2.8.1 Melt compositions preserved in the ultramafic dikes

2.8.1.1 Flow differentiation

The examined dikes are similar in their field occurrences, petrography, whole-rock chemical compositions, mineral chemical compositions, and isotopic compositions, as described above, irrespective of the phenocryst distribution in each dike. It is, therefore, expected that they formed in a series of intrusion events from a common magma and that the phenocryst distribution was controlled by intrusion and solidification processes. The high concentration of phenocrysts in the dike center and shape-preferred orientation of the olivine phenocrysts in the marginal zone indicate the operation of flow differentiation owing to a velocity gradient in flowing dikes, which is known as "Bagnold effect" (Bagnold, 1954; Komar, 1972). The homogeneous distribution and less distinct shape-preferred orientation of phenocrysts in some dikes can be explained by a turbulent flow associated with a high Reynolds number. The distributions of phenocrysts in the dikes suggest that the magmas were injected as crystal-laden magmas which solidified in a closed system on a short time scale to maintain the distribution of phenocrysts under the gravitational field irrespective of the zoned or homogeneous distribution.

2.8.1.2 Mg-Fe interdiffusion

Examination of the variation of Mg# of olivine across the contacts between the host peridotite and the dike (Fig. 2-8a) also supports such rapid solidification. The area ratio of the Mg-Fe profile of olivine in the dike and the host sides (Fig. 2-8a) is 0.69 : 0.31, which is clearly different from 1:1. The host peridotite is mainly composed of olivine (~99 wt%), whereas the dike side is composed of olivine phenocrysts (~37.0 wt%) and matrix minerals (amphibole, ~58.3 wt%; orthopyroxene, ~3.9 wt%; and clinopyroxene, ~0.1 wt%; Table 2-3) which are calculated from the igneous modal composition of the DKSH2EI in vol% (Table 2-1). Taking the igneous modal abundance of the dike side into consideration, it is shown that the mass balance of MgO is maintained in a closed system, within a uncertainty smaller than ~15% (Table 2-3). Therefore, the Mg-Fe profile in the homogeneous-type dike is due to subsolidus diffusional Mg-Fe exchange after the solidification of the magma on a time scale much longer than Fe-Mg exchange involving magma over 10 cm. The Mg# profile across the contact is asymmetric and characterized by a shorter tail on the host dunite side and a longer tale within the dike (Fig. 2-8a). This feature is attributable to Mg-Fe interdiffusion with composition dependence and the difference in igneous modal abundance. This is consistent with the much narrower variation of NiO content in olivine than that of Mg# because the Ni diffusion is slower than the Fe-Mg interdiffusion (Fig. 2-8b; Petry et al., 2004; Dohmen and Chakraborty, 2007). It is highly plausible that the melt composition in the dikes is preserved with limited interaction with the wall rocks by rapid solidification after the magma intrusion. The time scale for the development of the Mg# profile in the dunite host over the 50 mm distance is roughly estimated to be one million to a few millions years with the assumption of the effective temperatures ranging 1100 – 1300 ℃ by using Mg-Fe interdiffusion coefficients (Dohmen and Chakraborty, 2007).

Table 2-3: Results of examination of mass balance of MgO between the dike (DKSH2) and its host dunite from the Mg# profile crossing their contact shown in Fig. 2-8.

	host dunite	dike (DKSH2)
Observed zoning profile		
variation width (mm)	50	54
area ratio of the profile	0.31	0.69
Mg#		
mean of all analyses	0.90	0.84
mean at a flat segment far away from the contact	0.90	0.83
Modal abundance (wt%)		
olivine	99.9	37.0
amphibole	-	58.3
clinopyroxene	-	0.1
orthopyroxene	-	3.9
MgO mass balance		
olivine	1.00	0.75
amphibole	-	0.36
clinopyroxene	-	0.00
orthopyroxene	-	0.04
Total	1.00	1.15

Notes: The mass of MgO lost from the host with the initial Mg# = 0.9, which is the homogeneous Mg# of olivine in the host away from the contact, and the mass gained by the dike with assumed initial Mg# = 0.83, which is the mean Mg# at the dike center, are calculated. If the former is given as unity, the latter is calculated to be 1.15, which implies that the diffusional Mg-Fe exchange between the dike and the host took place almost in a closed system under subsolidus condition.

2.8.2 Restoration of original whole-rock compositions for major elements

2.8.2.1 Subsolidus modifications due to alteration.

The presence of secondary hydrous minerals, such as serpentine, diopside, and chlorite, as described in the petrography section, indicates that the dikes suffered from alteration. In order to clarify if the formation of secondary hydrous phases modified the whole-rock compositions, we

compared two pairs of samples from dike DKSH2, which show a different degree of alteration while keeping the same igneous modal abundances (Table 2-1). Loss on ignition (LOI) was used as a quantitative measure of the degree of alteration, and the effects of alteration were examined by plotting oxide wt% data against the LOI (Fig. 2-14). A vector defined by a pair of samples with a difference in LOI and oxide contents is regarded as a trend of alteration. The obtained mean alteration vectors from the two sample pairs are listed in Table 2-4. The initial whole-rock water contents for each sample can be estimated from the water content of pargasite (~2.5 wt%) and its modal abundances (Tables 2-1 and 2-5). We obtained whole-rock compositions prior to alteration for nine samples by extrapolating the whole-rock data to the initial whole-rock water contents. The corrected compositions are listed in Table 2-5.

Table 2-4: Slopes defined by the difference in oxide contents of two samples from dike DKSH2 with a large contrast in degree of alteration in the diagram of oxides wt% plotted against loss on ignition (LOI) (Fig. 2-14). The slope values represent relative changes of major oxide wt% to an increase in the LOI.

	slopes ($\times 10^{-2}$)
SiO_2	- 7.03
TiO_2	- 2.86
Al_2O_3	85.75
Fe_2O_3	6.88
MnO	- 0.22
MgO	- 88.61
CaO	- 21.08
Na_2O	24.91
K_2O	2.82
P_2O_5	0.01
NiO	- 0.50
Cr_2O_3	- 0.08

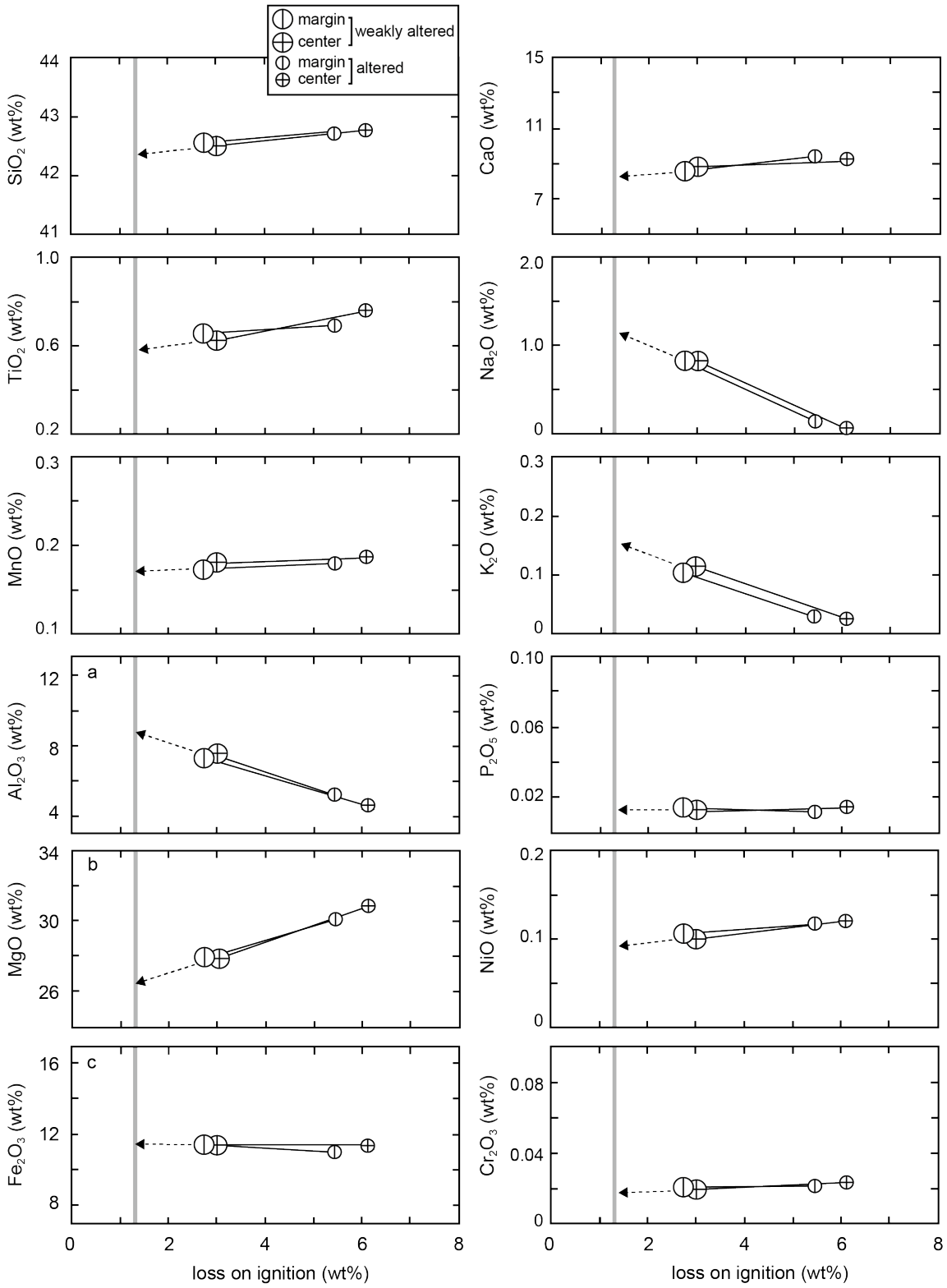
margin
center
weakly altered
margin
center
altered
SiO2 (wt%)
CaO (wt%)
TiO2 (wt%)
Na2O (wt%)
MnO (wt%)
K2O (wt%)
a
Al2O3 (wt%)
P2O5 (wt%)
b
MgO (wt%)
NiO (wt%)
c
Fe2O3 (wt%)
Cr2O3 (wt%)
loss on ignition (wt%)
loss on ignition (wt%)

Fig. 2-14: Whole-rock SiO_2, TiO_2, MnO, Al_2O_3, MgO, Fe_2O_3, CaO, Na_2O, K_2O, P_2O_5, NiO, Cr_2O_3 contents of two pairs of samples from dike DKSH2 plotted against their loss on ignition (LOI). Each pair, connected by a solid line, was sampled within ~4 cm distant in the same dike and has the same igneous modal composition and texture but a difference in alteration degree (Table 2-1). Symbols with a vertical line and a cross indicate margin and center of the dike, respectively. Data with large symbols are from less altered, and those with small symbols are from more altered samples. The gray vertical bands indicate the range of initial water content (1.31 - 1.36 wt%) estimated from the water contents of amphibole and the igneous modal abundances of each sample. Correction of alteration was made by linearly extrapolating the tie lines to the expected initial water content as shown by the dashed arrows. The restored original major elements contents (open circles) and the mean slopes of the tie lines are listed in Tables 2-4 and 2-5, respectively.

2.8.2.2 Subsolidus high-temperature modifications due to elemental exchange with the host.

The variation of the Mg# of olivine observed near the contact of dike DKSH2 and the host (Fig. 2-8) shows that the whole-rock MgO and FeO concentrations in the dike were modified by subsolidus diffusion at high temperatures as discussed above. Figure 2-8 shows that the modification is limited to within 4 cm from the contact with the host. Most of the samples including the rootless blocks with more than 10 cm size were, therefore, not affected by the diffusional exchange. However, the whole-rock chemical compositions of the samples near the contact (DKSH1ES and DKSH2EI; Table 2-1) were shifted from the values that these rocks had soon after the dike solidification. The whole-rock composition of sample DKSH2EI before the subsolidus high-temperature modification was restored by using the initial olivine Mg# in the

center (~0.83, Fig. 2-8a), which was not modified by this modification, and the igneous modal abundance (Table 2-5). The same procedure cannot be applied to DKSH1ES because of its extensive alteration. The restored composition for DKSH2EI is lower in MgO and higher in FeO (Table 2-5). The whole-rock major element compositions corrected for the alteration and diffusional elemental exchange with the host are plotted in Fig. 2-15 excepting sample DKSH1ES.

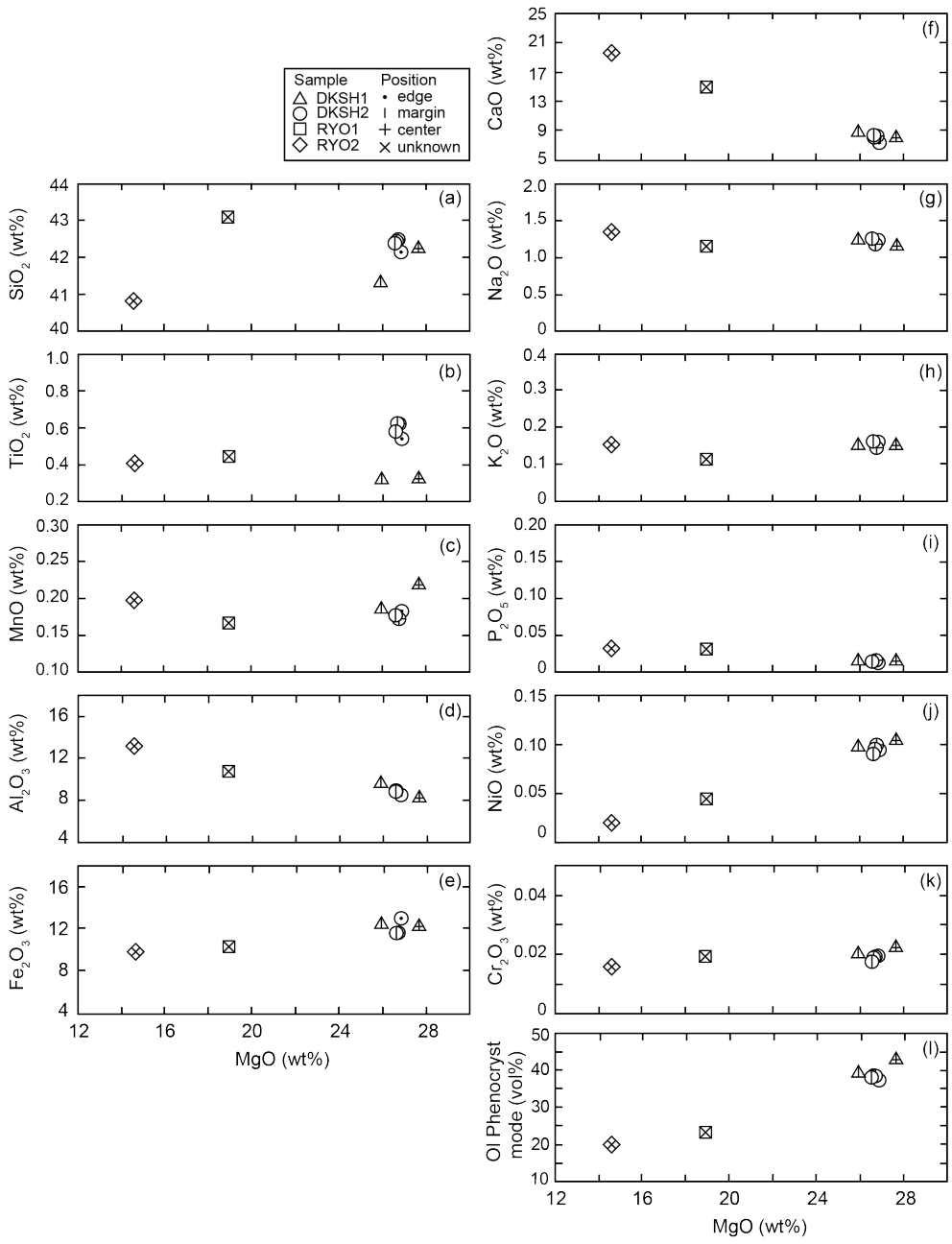

Fig. 2-15: (a) – (k) Alteration-corrected whole-rock SiO_2, TiO_2, MnO, Al_2O_3, Fe_2O_3, CaO, Na_2O, K_2O, P_2O_5, NiO, Cr_2O_3 contents plotted against MgO for nine samples of the examined four dikes. (l) Original modal abundances of olivine phenocryst are also plotted against the MgO. Triangles, circles, squares, and diamonds indicate examined dikes: DKSH1, DKSH2, RYO1, and RYO2, respectively. Symbols with a dot, vertical line, plus, and cross denote samples from the edge, margin, and center of dikes, and rootless block without information on sample position in the dike, respectively.

Table 2-5: Major element contents of the examined four dike samples after the correction of alteration (ALT) and after the correction of high-temperature diffusional modification (High-T).

Dike	DKSH1			DKSH2						RYO1	RYO2
Sample	DKSH1ES	DKSH1MI	DKSH1CI	DKSH2EI		DKSH2MI	DKSH2MW	DKSH2CI	DKSH2CW	RYO1I	RYO2I
Correction	ALT	ALT	ALT	ALT	ALT & High-T	ALT	ALT	ALT	ALT	ALT	ALT
(wt%)											
SiO_2	39.73	41.28	42.22	42.46	42.13	42.42	42.47	42.42	42.36	43.11	40.81
TiO_2	0.92	0.31	0.32	0.54	0.53	0.58	0.62	0.62	0.57	0.45	0.41
Al_2O_3	11.06	9.53	8.11	8.42	8.40	8.75	8.66	8.75	8.84	10.62	13.05
Fe_2O_3	14.17	12.51	12.12	11.55	13.04	11.44	11.58	11.70	11.53	10.23	9.69
MnO	0.13	0.18	0.22	0.18	0.18	0.17	0.17	0.18	0.18	0.17	0.20
MgO	20.54	25.96	27.69	28.00	26.89	26.66	26.75	26.68	26.58	18.92	14.57
CaO	11.89	8.73	7.91	7.35	7.33	8.56	8.31	8.13	8.41	15.14	19.71
Na_2O	1.32	1.21	1.13	1.22	1.22	1.16	1.17	1.25	1.24	1.16	1.35
K_2O	0.16	0.15	0.15	0.16	0.16	0.14	0.14	0.16	0.16	0.12	0.15
P_2O_5	0.01	0.01	0.01	0.01	0.01	0.01	0.01	0.01	0.01	0.03	0.03
NiO	0.05	0.10	0.10	0.10	0.09	0.10	0.10	0.09	0.09	0.04	0.02
Cr_2O_3	0.02	0.02	0.02	0.02	0.02	0.02	0.02	0.02	0.02	0.02	0.02
Total	100.00	100.00	100.00	100.00	100.00	100.00	100.00	100.00	100.00	100.00	100.00
Amphibole abundance	39.32	39.39	38.95	58.29	-	54.41	54.41	52.32	52.32	31.55	19.34
H_2O [1]	0.98	0.98	0.97	1.46	-	1.36	1.36	1.31	1.31	0.79	0.48

Notes: The latter correction is necessary for DKSH1ES and DKSH2EI sampled taken from the dike edges, but the DKSH1ES is too altered to make the reliable correction as done for DKSH2EI. Major element oxides are recalculated to 100 wt % volatile free.

[1] Whole-lock water content calculated from the water content of amphibole (2.5wt%) and its modal abundance.

2.8.3 Estimation of intruded melt compositions for major elements and igneous olivine compositions.

The liquid composition of magmas intruded into fractures and frozen as ultramafic dikes is not simply the whole-rock compositions after the corrections made above. This is because the dikes contain a large number of phenocrysts. The liquid parts of the magmas including phenocrysts at the time of intrusions are called “intruded melt”, hereafter. The MgO concentrations of whole rocks corrected for alteration and elemental exchange with the host vary

from 14.6 to 27.7 wt% and show negative and linear overall correlations with Al_2O_3, CaO, NiO, Cr_2O_3, P_2O_5, at nearly constant FeO concentrations (Fig. 2-15; Table 2-5) as in the case of Hawaiian basalts (e.g., Rhodes and Vollinger, 2004; Putirka, 2005). The negative correlations with MnO, Na_2O, and K_2O are also recognized, though they are weak. The overall correlations among these oxide wt% and the correlation of phenocryst abundances with MgO contents (Fig. 2-15l) suggest that the linear relationships are due to a binary mixing of the phenocrysts and an intruded melt. However, such linear correlations are not clear in MgO-SiO_2 and MgO-TiO_2 plots (Fig. 2-15; Table 2-5). These relationships may indicate that the end components of mixing, either phenocrysts or melt or the both do not have exactly the same compositions for all the dikes. We thus estimated a melt end component for each dike assuming that the other component is olivine crystals. Contribution of clinopyroxene phenocrysts may be negligible because of their small amounts observed in the dikes (Table 2-1).

We need to know the accurate abundance and composition of olivine crystals to properly estimate the intruded melt compositions. Although we can obtain the average amount of olivine crystals loaded in the intruded magma by integrating the heterogeneously distributed olivine phenocrysts over the dike width if necessary, we cannot easily estimate the chemical composition of the olivine phenocrysts at the time of intrusion. The measured Mg# of olivine (~0.83, Fig 2-8a), the lowest value in the dikes, does not represent an igneous composition. This is because the current compositions of olivine phenocrysts are not those in equilibrium with the intruded melt owing to the modification through elemental exchange with the interstitial melt and further with the other constituent minerals at subsolidus by diffusion over the grain scale. The scale of diffusional exchange between olivine phenocrysts and the surrounding melt in the dikes after the cessation of magma transportation is smaller than the sample scale. On the basis of this limitation

of olivine-melt interaction, we can estimate the olivine and host melt composition at high temperature from the measured whole-rock composition listed in Table 2-5 and the olivine phenocryst-matrix ratio listed in Table 2-1 by taking the following steps. The important assumption is that the olivine phenocrysts and the intruded melt were in equilibrium at the time of intrusion, which is supported by the olivine composition homogeneous in grains and consistent in samples excepting the sample from the dike margin.

Step1: We assume a Mg#, NiO and MnO content for olivine in equilibrium with a hypothetical intruded melt, starting with the measured $Mg\#_X$, NiO_X, and MnO_X for example. Step2: We subtract the observed amount of all olivine phenocrysts with the assumed $Mg\#_X$, NiO_X, and MnO_X contents from a whole-rock composition (Tables 2-1 and 2-5). After subtracting phenocrysts, we obtain a hypothetical intruded melt as a residue of the subtraction. This is called $melt_Z$. Step3: We calculate a Mg#, NiO, and MnO content for an olivine in equilibrium with the $melt_Z$ using the partition coefficients of Mg, Fe, Ni, and Mn between olivine and melt (Beattie et al., 1991; Kinzler et al.,1990). The calculated contents are called $Mg\#_Y$, NiO_Y, and MnO_Y. Step4: We check if the values of $Mg\#_X$, NiO_X, and MnO_X, and those of $Mg\#_Y$, NiO_Y, and MnO_Y, are respectively the same. If we assumed appropriate values of Mg#, NiO, and MnO of olivine in Step1, these values of X and Y should be the same. However, this is usually not the case. Step5: When the values of Y are different from those of X, then we go back to Step 1 and assume slightly different values of X, and go to Step 2. By repeating Step1 to Step5 until the X and Y sets of olivine compositions coincide, we obtain the intruded melt composition and the Mg#, NiO, and MnO contents of olivine in equilibrium with the intruded melt. The ratios of Fe^{3+}/ total Fe of the intruded melts are assumed to be ~0.13, which was estimated by applying the olivine-orthopyroxene-spinel oxygen geobarometry to our samples (Ballhaus et al., 1991; Sack et al.,

1980; O'Neill, 1987). The results are listed in Table 2-6. The estimated Mg#, NiO, and MnO contents of olivine vary from 0.85 to 0.89, 0.08 to 0.21, and 0.17 to 0.32, respectively.

The examined dikes show no features suggesting vesiculation during solidification, as mentioned above. This observation and the estimated emplacement pressure of the host Cumulate Member (~0.6 GPa; Ozawa, 1986) suggest that the intruded melts were undersaturated with water, which was retained in hydrous phases without degassing. Since the initial hydrous mineral in the dikes is pargasite with ~2.5 wt% water, we estimated the initial water content for each dike by using the modal abundance of pargasite (Table 2-6). The estimated water contents in the intruded melt vary from 0.6 to 2.3 wt%. Even for the maximum estimate (2.3 H_2O wt%), the saturation pressure of the intruded melt is < ~0.1 GPa according to VOLATILECALC (Newman and Lowenstern, 2002), which is distinctively lower than the pressure of solidification of the dikes.

Table 2-6: Major and trace element contents of intruded melts and chemical composition of olivine phenocrysts in equilibrium with the melts estimated for each examined dike.

Dike	DKSH1		DKSH2		RYO1	RYO2
		1SE [1]		1SE [1]		
Intruded melt						
Major oxides (wt%)						
SiO_2	43.52	0.64	44.19	0.05	44.58	41.46
TiO_2	0.56	0.02	0.98	0.02	0.62	0.53
Al_2O_3	15.78	0.51	14.64	0.08	14.64	16.89
FeO	9.57	0.09	9.57	0.26	7.38	6.40
MnO	0.20	0.01	0.18	0.00	0.15	0.17
MgO	11.43	0.10	12.76	0.12	8.72	5.98
CaO	14.89	0.15	13.73	0.31	20.86	25.50
Na_2O	2.10	0.00	2.03	0.03	1.59	1.74
K_2O	0.27	0.00	0.26	0.01	0.16	0.20
P_2O_5	0.02	0.00	0.02	0.00	0.04	0.04
Fe_2O_3	1.60	0.02	1.59	0.04	1.23	1.07
NiO	0.02	0.00	0.02	0.00	0.01	0.00
Cr_2O_3	0.03	0.00	0.03	0.00	0.02	0.02
Total	100.00		100.00		100.00	100.00
H_2O	1.74	0.04	2.27	0.05	1.08	0.62
Trace elements (ppm)						
Ba	187	1	189	9	128	120
U	0.08	0.04	0.10	0.03	0.03	0.02
Nb	0.99	0.12	1.91	0.12	0.82	0.94
Ta	0.06	0.01	0.12	0.01	0.08	0.06
La	2.59	0.08	1.85	0.11	1.43	0.95
Ce	5.58	0.10	5.49	0.29	3.79	3.33
Pr	0.89	0.00	1.05	0.05	0.72	0.61
Pb	0.55	0.03	1.39	0.10	2.53	1.12
Sr	259	6	319	15	119	89
Nd	4.56	0.07	6.54	0.29	4.60	4.08
Hf	0.85	0.03	1.13	0.04	0.92	0.75
Zr	23.9	0.9	28.4	1.2	23.1	18.6
Sm	1.50	0.06	2.21	0.11	1.64	1.64
Eu	0.69	0.05	0.85	0.05	0.61	0.64
Gd	2.25	0.05	3.03	0.10	2.35	2.17
Tb	0.37	0.01	0.50	0.02	0.38	0.39
Dy	2.69	0.10	3.46	0.14	2.63	2.68
Y	14.2	0.5	17.7	0.7	14.4	12.8
Ho	0.55	0.02	0.70	0.03	0.55	0.56
Er	1.59	0.05	1.97	0.08	1.59	1.50
Tm	0.22	0.01	0.27	0.01	0.21	0.20
Yb	1.47	0.04	1.82	0.08	1.34	1.28
Lu	0.22	0.01	0.27	0.01	0.19	0.19
Olivine in equilibrium with intruded melt						
Mg#	0.88	0.00	0.89	0.00	0.88	0.85
NiO (wt%)	0.21	0.00	0.21	0.01	0.14	0.08
MnO (wt%)	0.20	0.02	0.17	0.00	0.21	0.32
Abundance (wt%)	43.6	2.0	40.1	0.3	26.8	22.2

Notes: For two dikes (DKSH2 and DKSH1) mean values and their standard errors (±1SE) are listed.

Major element oxides are recalculated to 100 wt % volatile free.

[1] standard error of the mean

2.8.4 Estimation of intruded melt compositions for trace elements

The rare earth element (REE) concentrations of the measured samples do not show any systematic relationships with the degree of alteration or LOI (Fig. 2-6c). Therefore, we infer that the REE in dike samples were not modified by secondary processes, and we calculated the REE of the intruded melts from the raw whole-rock data by subtracting the contribution of the phenocrysts (Table 2-6).

We also estimated most of the trace elements of the intruded melts in the same way as the REEs (Table 2-6). However, some trace elements, particularly fluid-mobile incompatible elements, which are prone to secondary open processes such as alteration, show variations controlled by the degree of alteration or LOI. Our samples contain secondary minerals replacing primary minerals and occurring in veinlets cross-cutting the primary textures. These indicate some corrections must be made for these elements. We calculated the whole-rock compositions of intruded melt from the trace element and the igneous modal abundances of matrix minerals for the least altered dike, DKSH2, whose matrix is composed mostly of amphibole and clinopyroxene (> 97 %; Table 2-1). The results are listed in Table 2-7 and plotted in Fig. 2-16. The calculated trace element patterns of the intruded melt are smooth, and several positive anomalies of, Ba, U, and Sr noted in the whole-rock data are subdued.

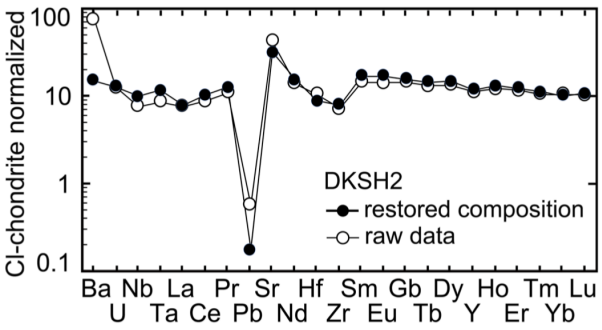

Fig. 2-16: Chondrite-normalized trace element patterns of the intruded melts for the dike (DKSH2) estimated from amphibole and clinopyroxene compositions and their modal abundances in the matrix (solid circles, Table 2-7) and the bulk composition directory measured with ICP-MS (open circles; DKSH2 in Table 2-6).

Table 2-7: Concentrations of highly incompatible trace elements in amphibole and clinopyroxene consisting the matrix of DKSH2.

	Amphibole		Clinopyroxene		estimated matrix	
	Average	1SE [1]	Average	1SE [1]		1SE [1]
(ppm)						
Ba	38.4	3.0	5.4	2.7	37.1	2.9
U	0.11	0.01	0.04	0.00	0.10	0.01
Nb	2.57	0.18	0.07	0.01	2.47	0.17
Ta	0.17	0.02	0.01	0.00	0.17	0.02
Pb	0.44	0.03	0.06	0.01	0.42	0.03
Sr	243	11	36	5	235	10
Hf	0.94	0.04	1.01	0.04	0.94	0.04
Zr	31.1	1.3	33.2	0.5	31.2	1.3

Notes: The trace element concentrations of the matrix estimated from the weight fraction and chemical compositions of the amphibole and clinopyroxene listed in the first and second columns, respectively, are shown in the last column.

[1] standard error of the mean

2.8.5 Estimation of primary melt compositions

It is very plausible that a melt frozen in the form of the matrix of ultramafic dikes underwent fractional crystallization during its ascent from the melting/melt segregation depth in the deeper mantle to the intrusion site, which is apparent by the presence of abundant olivine and clinopyroxene phenocrysts. We have to evaluate this process in order to estimate the composition of a primary melt generated in the mantle. Because fractionation of olivine, the most plausible fractionated mineral, strongly affects Mg#, MnO, and NiO of olivine in equilibrium with the melt, these parameters are used as proxies for the extent of fractionation. We have to know the mantle composition in order to adopt the proxies. The ranges of Mg#, NiO and MnO of olivine in the upper mantle are known as the olivine mantle array estimated from compiled data of mantle xenoliths (Takahashi et al., 1987) (Fig. 2-17). The NiO contents of olivine for a given value of Mg# varies by ~0.08 wt%, which corresponds to the width of the array. We adopt the lowest edge of the array data field (e.g., NiO wt% = 0.36 at Mg#, 0.90). This is because olivine in the mantle xenoliths analyzed by Takahashi et al. (1987) underwent various degrees of subsolidus Ni exchange with pyroxenes and spinel, which increases NiO in olivine depending on the subsolidus thermal history. Even if we use the NiO content in the middle of the olivine mantle array field, the estimated MgO content in the primary melt increases by less than 0.6 wt%, which does not alter our conclusion on melting conditions as discussed below. The amount of fractionated olivine and the primary melt compositions for each dike are estimated by repeatedly adding olivine phenocrysts with a chemical composition in equilibrium with the melt in 0.1 wt% step until the olivine composition reaches the olivine mantle array. We used Beattie et al. (1991) and Kinzler et al. (1990) for olivine-melt partition relationships for Mg-Fe, Ni, and Mn. Starting melt compositions are the above estimated intruded melt compositions (Table 2-6). The estimated amounts of fractionated olivine for the four dikes are listed in Table 2-8. The major element

compositions of the estimated primary melts are also listed in Table 2-8. Even if we adopt the half width of the olivine mantle array as the uncertainty of the mantle NiO (~0.04 NiO wt%), the error in the MgO of the primary melt is < 1.0 wt%.

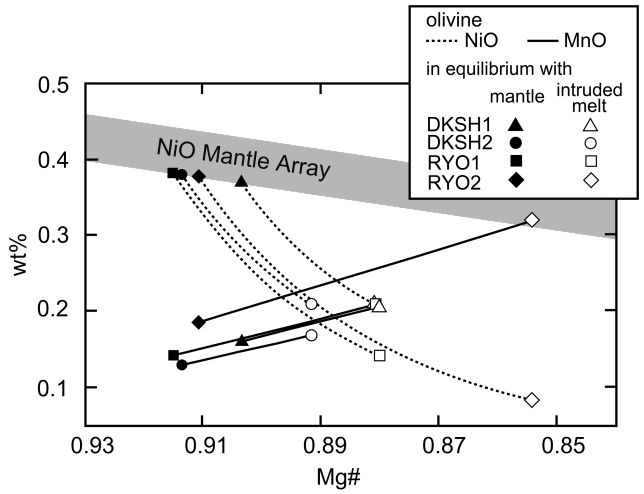

Fig. 2-17: Relationships of NiO and MnO wt% against Mg# of olivine to show our estimation procedure for constraining olivine compositions in equilibrium with residual peridotites after production of the primary melts for the examined 4 ultramafic dikes (DKSH1, triangle; DKSH2, circle; RYO1, square; and RYO2, diamond). Open symbols represent olivine compositions in equilibrium with the intruded melts (Table 2-6). Starting from these compositions, compositions of olivine in equilibrium with the residual peridotite (solid symbols) are estimated by adding olivine according to the maximum olivine fractionation model as shown by dashed lines for NiO and solid lines for MnO until reaching the lower edge of the olivine mantle array for Mg#-NiO after Takahashi et al. (1987) (shaded region) by using partition coefficients after Beattie et al. (1991) and Kinzler et al. (1990).

The water and rare earth and trace element concentrations in the primary melts are also corrected for olivine addition. The results are listed in Table 2-8 and plotted in Fig. 2-18. The chondrite-normalized ratios of Dy and Yb ((Dy/Yb)n) of the primary melt of the four dikes are

1.22 - 1.40 and larger than the range of the compiled literature data of the present-day NMORB and normal back-arc basin basalts (NBABB) (0.95 - 1.20) (see below for discussion on (Dy/Yb)n).

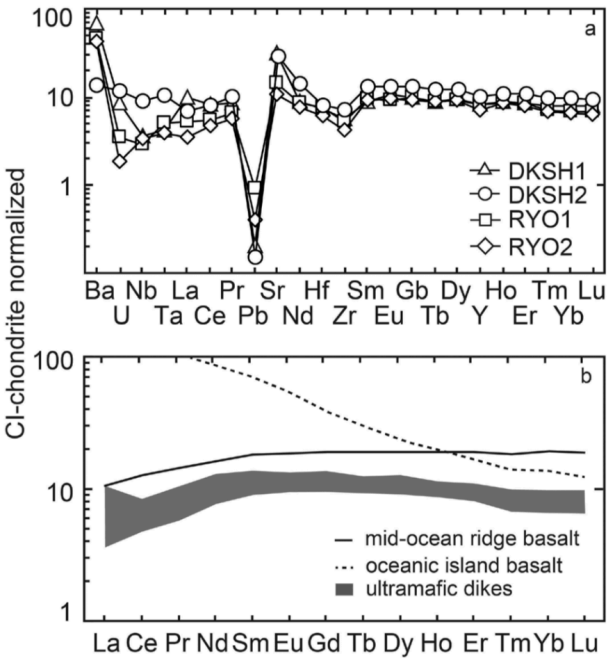

Fig. 2-18: Chondrite-normalized trace element patterns in primary melts being in equilibrium with mantle peridotite estimated for the four dikes (a), and the range of chondrite-normalized rare earth element (REE) pattern (b). The REE patterns of mid-ocean ridge basalts and ocean island basalts after Sun and McDonough (1989) are shown in (b) for comparison. Triangles, circles, squares, and diamonds in (a) indicate examined dikes: DKSH1, DKSH2, RYO1, and RYO2, respectively.

Table 2-8: Major and trace element concentrations and normative composition of the primary melts in equilibrium with the residual peridotites estimated for each examined dike.

Dike	DKSH1		DKSH2		RYO1	RYO2
		1SE [1]		1SE [1]		
Primary melt						
Major oxides (wt%)						
SiO_2	43.28	0.58	43.85	0.06	44.15	41.36
TiO_2	0.51	0.01	0.88	0.02	0.55	0.46
Al_2O_3	14.37	0.50	13.13	0.10	12.94	14.66
FeO	9.64	0.10	9.54	0.25	7.64	6.98
MnO	0.20	0.01	0.18	0.00	0.16	0.18
MgO	14.74	0.18	16.52	0.19	13.37	11.54
CaO	13.56	0.17	12.31	0.30	18.45	22.13
Na_2O	1.92	0.00	1.82	0.02	1.41	1.51
K_2O	0.24	0.00	0.23	0.00	0.14	0.17
P_2O_5	0.02	0.00	0.02	0.00	0.04	0.04
Fe_2O_3	1.45	0.02	1.43	0.04	1.09	0.93
NiO	0.04	0.00	0.05	0.00	0.04	0.03
Cr_2O_3	0.03	0.00	0.02	0.00	0.02	0.02
Total	100.00		100.00		100.00	100.00
H_2O	1.59	0.03	2.05	0.04	0.96	0.54
Trace elements (ppm)						
Ba	171	2	33	3	114	105
U	0.07	0.04	0.09	0.01	0.03	0.02
Nb	0.91	0.11	2.23	0.15	0.73	0.82
Ta	0.06	0.01	0.15	0.01	0.07	0.05
La	2.37	0.07	1.67	0.10	1.28	0.83
Ce	5.10	0.08	4.95	0.26	3.38	2.91
Pr	0.81	0.01	0.95	0.04	0.64	0.54
Pb	0.51	0.03	0.38	0.03	2.25	0.98
Sr	236	5	212	9	106	78
Nd	4.17	0.05	5.90	0.21	4.10	3.57
Hf	0.78	0.03	0.85	0.04	0.82	0.65
Zr	21.88	0.80	28.14	1.14	20.56	16.28
Sm	1.37	0.05	1.99	0.10	1.46	1.43
Eu	0.63	0.05	0.76	0.05	0.54	0.56
Gd	2.05	0.04	2.73	0.09	2.09	1.90
Tb	0.33	0.01	0.45	0.02	0.34	0.34
Dy	2.46	0.09	3.12	0.12	2.34	2.35
Y	12.98	0.44	15.93	0.62	12.86	11.18
Ho	0.50	0.01	0.63	0.02	0.49	0.49
Er	1.45	0.05	1.78	0.07	1.42	1.31
Tm	0.20	0.01	0.25	0.01	0.18	0.17
Yb	1.35	0.03	1.64	0.07	1.20	1.12
Lu	0.20	0.00	0.24	0.01	0.17	0.17
Norm components[2]						
Ne'	23.3	0.5	20.9	0.4	23.3	22.7
Qtz'	0.3	0.2	2.1	0.4	0.0	0.0
Ol'	76.4	0.7	77.0	0.3	76.7	77.3
Olivine in equilibrium with primary melt						
Mg#	0.90	0.00	0.91	0.00	0.91	0.91
NiO (wt%)	0.37	0.00	0.38	0.00	0.38	0.38
MnO (wt%)	0.16	0.01	0.13	0.00	0.14	0.19
Added mass (wt%)	9.4	0.2	10.9	0.4	12.3	14.2

Notes: The chemical compositions of olivine in the residual peridotites are also listed. The mean values and their ±1SE are shown for two dikes (DKSH2 and DKSH1) with multiple samples (Table 1). Major element oxides of the estimated primary melts are recalculated to 100 wt % volatile free.

[1] standard error of the mean

[2] C. I. P. W norm mineral components calculated from primary melt (Ne'= nepheline + 0.6albite, Ol'= olivine + 0.75orthopyroxene and Qtz'= Quartz + 0.4albite + 0.25orthopyroxene)

2.8.5 Estimation of melting mechanisms and mantle source compositions

The estimated primary melt compositions from the ultramafic dikes reflect the melting/melt segregation conditions: pressure, temperature, degree of melting/melt segregation, and mantle source compositions. Melt segregation processes could also affect the composition. We constrained the mantle source composition and the segregation processes on the basis of the REE compositions of the primary melts estimated from the four dikes (DKSH1, DKSH2, RYO1, and RYO2). They are modeled with a one-dimensional steady-state decompressional melting model (Ozawa, 2001) using published partition coefficients (Table 2-9) (Fig. 2-19). The modeling conditions are summarized in Table 2-10, and their complete lists are available in Tables A1 – A4. Careful examination of the accumulated melt compositions in the near fractional melting models without any fluid influx for the four dikes show the followings. (1) Melting must have taken place in the garnet stability field irrespective of whether the mantle source is the primitive mantle (PM) or MORB mantle source (MM) in order to reproduce the weak decline of heavy rare earth elements (HREE). The extent of melting in the garnet stability field ranges from 75 to 100% of the total melting, if a near fractional melting model with complete melt accumulation is assumed (Table 2-10). (2) A depleted mantle source, such as a MORB mantle source (MM), is required in order to better fit the pattern of the middle rare earth elements. (3) There are two possible models to better reproduce light rare earth elements (LREE): instantaneous melt formed by near fractional melting of the MORB mantle source or accumulated melt formed by fractional melting of a slightly more depleted mantle source, such as the depleted MORB mantle source (DMM). The modeling results are essentially the same for the four examined dikes (Fig. 2-19 and Table 2-10).

Table 2-9: Partition coefficients of rare earth and other trace elements between melts and minerals used in the melting models. The data are after Beattie (1993, 1994), Hart and Dunn (1993), Green (1994), McKenzie and O'Nions (1991), Kennedy et al. (1993), Matsui et al. (1977), Ozawa and Shimizu (1995), Hauri et al. (1994), Jenner et al. (1993), Johnson (1994), Frey (1969), Skulski et al. (1994), Kelemen et al. (1990), Dunn and Sen (1994), Kelemen and Dunn (1992), Nicholls and Harris (1990), Irving and Frey (1984), Fujimaki et al. (1984), Colson et al. (1988), and Nikogosyan and Sobolev (1997).

	olivine	spinel	orthopyroxene	clinopyroxene	garnet
Ba	0.000032	0.	0.0035	0.0006	0.0007
U	0.000018	0.	0.0017	0.00361	0.00918
Nb	0.0001	0.02	0.003	0.0077	0.015
Ta	0.00007	0.02	0.003	0.0102	0.02
Pb	0.00048	0.	0.0013	0.072	0.0005
Sr	0.0015	0.	0.007	0.1283	0.006
Hf	0.0038	0.02	0.01	0.256	0.24
Zr	0.007	0.02	0.021	0.123	0.5
La	0.000028	0.01	0.0025	0.054	0.0015
Ce	0.000038	0.01	0.005	0.086	0.008
Pr	0.0008	0.01	0.0048	0.15	0.054
Nd	0.00042	0.01	0.0068	0.19	0.087
Sm	0.0013	0.008	0.01	0.29	0.7
Eu	0.0016	0.007	0.013	0.31	0.9
Gd	0.0055	0.006	0.016	0.3	1.19
Tb	0.0041	0.009	0.019	0.31	1.5
Dy	0.01	0.01	0.022	0.33	2.2
Ho	0.007	0.009	0.026	0.31	3.3
Er	0.0087	0.01	0.03	0.29	3.6
Tm	0.009	0.01	0.12	0.26	3.5
Yb	0.017	0.008	0.05	0.28	3.9
Lu	0.02	0.02	0.06	0.28	3.8

The CRUS of the Tectonite Member of the Miyamori complex was inferred to have formed by fluxed fractional melting of the mantle wedge under extensive influx of a slab-derived fluid from the subducting slab strongly enriched in LREE and with anomalies of several trace elements (Ozawa and Shimizu, 1995; Yoshikawa and Ozawa, 2007). On the other hand, the REE and trace element patterns of the ultramafic dikes, as well as rocks of the Cumulate Member, do

not indicate any involvement of such fluids at all. The TiO_2/K_2O ratios of pargasite (Fig. 2-12), REE modeling results (Fig. 2-19), initial Nd and Sr isotope ratios of the whole-rock and separated clinopyroxene of the ultramafic dikes and the Cumulate Member (Yoshikawa and Ozawa, 2007) consistently show that they were derived from a depleted mantle, such as the MORB mantle source, with insignificant involvement of any types of H_2O/CO_2-rich fluids or exotic melts. The most plausible melting mechanism is, therefore, adiabatic decompressional melting, if the wide occurrence of such MORB-type mantle material in the uppermost mantle (Cipriani et al., 2004; Workman and Hart, 2005) is taken into consideration.

Table 2-10: Percentage of melting in the garnet stability field (PMGF) in the total melting degree that reproduces the rare earth element pattern of primary melt for each dike (Fig. 2-19) by a steady-state one-dimensional decompressional melting model (Ozawa, 2001).

Dike	Strength of melt separation	Mantle source [1]	PMGF (%)
DKSH1	accumulated	PM	95.7
		MS	88.7
		DMS	87.3
	instantaneous	MS	99.9
DKSH2	accumulated	PM	89.2
		MS	76.6
		DMS	75.5
	instantaneous	MS	99.9
RYO1	accumulated	PM	97.2
		MS	90.1
		DMS	93.0
	instantaneous	MS	99.9
RYO2	accumulated	PM	98.0
		MS	93.9
		DMS	93.9
	instantaneous	MS	99.9

Notes: The PMGFs are optimized for several sets of two of the model parameters: strength of melt separation shown in the first column and mantle source shown in the second column.

[1] PM, primitive mantle; MS, MORB mantle source; DMS, depleted MORB mantle source.

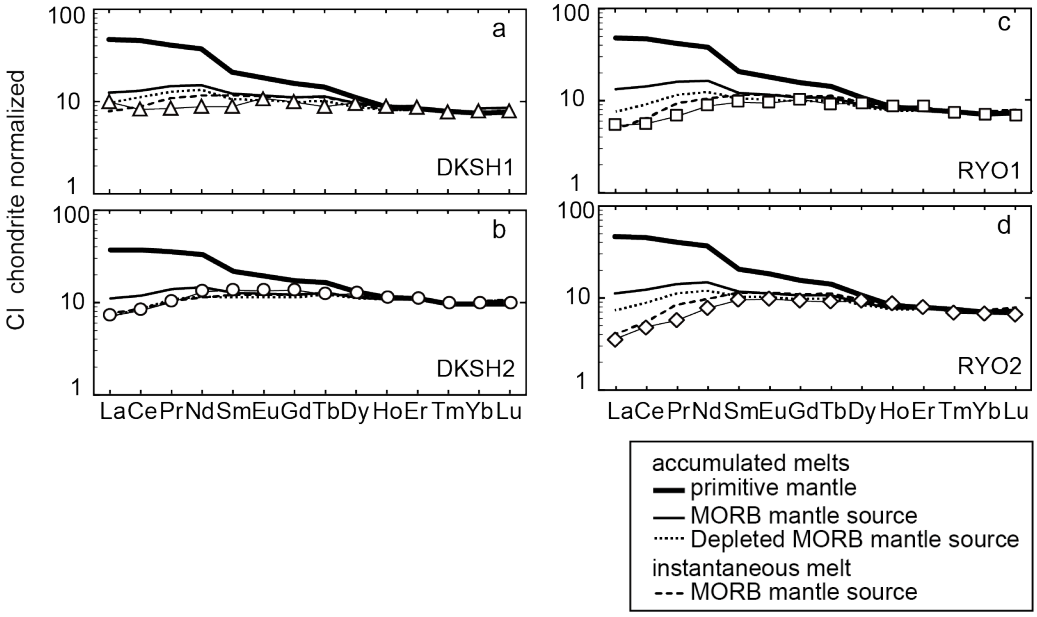

Fig. 2-19: Comparison of the chondrite-normalized rare earth element (REE) patterns of modeled and observed (solid lines with symbols; see Fig. 2-15) of the primary melts in equilibrium with mantle peridotite for four dikes (DKSH1, (a); DKSH2, (b); RYO1, (c); and RYO2, (d)). The adopted models are based on a one-dimensional steady-state decompressional melting model of Ozawa (2001) with adjustment of model parameters to best reproduce the observation. Effects of two of the most critical model parameters, mantle source composition and strength of melt separation, are shown for accumulated melt and primitive mantle, thick solid line; accumulated melt and MORB mantle source, solid line; accumulated and depleted MORB mantle source, dotted line; and instantaneous melt and MORB mantle source, dashed line (Table 2-10). The complete lists of optimized model parameters are listed in Tables A1 – A4 for the examined four dikes. The REE abundances in the primitive mantle are after McDonough and Sun (1995), and those of the mantle source of mid-ocean ridge basalt (MORB) and depleted MORB are after Workman and Hart (2005). The CI-chondrite composition is after McDonough and Sun (1995).

2.8.6 Estimation of melt segregation and solidus conditions and mantle potential temperatures

We estimated the melting/melt segregation pressure by plotting the estimated primary melt compositions in the Ne'-Ol'-Qtz' ternary norm diagram (Ne'= nepheline + 0.6 albite, Ol'= olivine + 0.75 orthopyroxene and Qtz'= Quartz + 0.4 albite + 0.25 orthopyroxene) according to the method of Irvine and Barager (1971).

The major elements compositions are strongly controlled by pressure and temperature conditions but relatively weakly dependent on the source composition, which is close to the depleted mantle in our case as discussed above from the geochemical data. We extended the pressure isopleths in the Ne'-Ol'-Qtz' ternary norm diagram constructed by Sakuyama et al. (2009) for pressures < 3 GPa to higher pressures > 3 GPa on the basis of melting experiments made at 3 and 6 GPa (Walter, 1998) (Fig. 2-20). We chose the 3 GPa results of Walter (1998) because the experiments were conducted by using piston-cylinder experimental apparatus, though we ignored one outlier with the highest SiO_2 content, which is peculiar in that orthopyroxene was not present in the residue (Walter, 1998). The 3 GPa isopleth based on Walter (1998) lies on the extension of that of Sakuyama et al. (2009) for lower degree of melting (Fig. 2-20). We chose the results of 6 GPa of Walter (1998) conducted by using multi-anvil high-pressure apparatuses because the results give a consistent trend in the ternary plot systematically decreasing Ne' with temperature and melting degree. We did not use the results of 5 and 7 GPa of Walter (1998), which are mostly overlapping with those of 6 GPa experiments. They give very scattered results in the ternary plot and are contrasting to the consistent results of 6 GPa experiments (Fig. 2-20). The isopleths for 4 and 5 GPa isopleths shown with dashed lines are obtained by a linear interpolation of 3 and 6 GPa isopleths, which is consistent with 4 GPa experimental results (Fig. 2-20).

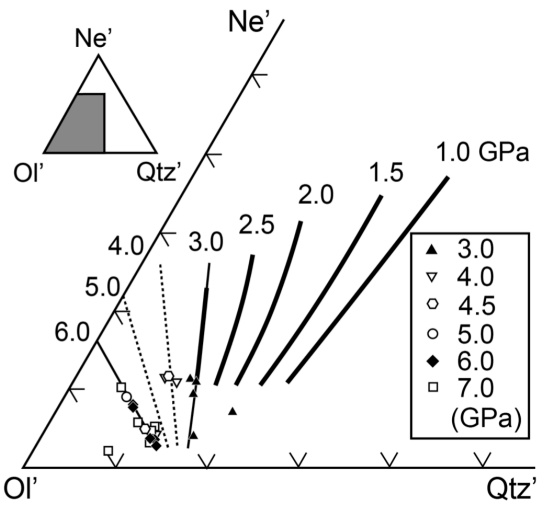

Fig. 2-20: Pressure isopleths in the Ne'-Ol'-Qtz' ternary normative composition for primary melts experimentally reproduced under anhydrous conditions to be in equilibrium with mantle peridotites. The isopleths for pressure ≤ 3.0 GPa shown with thick solid lines after Sakuyama et al. (2009), those for pressure at 3.0 and 6.0 GPa shown with solid lines are obtained by fitting experimental results at these pressures after Walter (1998) and extending the trend to the lower degree of melting region. The isopleths for 4 and 5 GPa isopleths shown with dashed lines are obtained by a linear interpolation of 3 and 6 GPa isopleths. Ne'= nepheline + 0.6 albite, Ol'= olivine + 0.75 orthopyroxene and Qtz'= Quartz + 0.4 albite + 0.25 orthopyroxene (Irvine and Barager, 1971)

The normative values of the primary melt compositions of the dikes are listed in Table 2-8, and plotted in Fig. 2-21. The estimated melting pressures for primary melt compositions of the dikes are listed in Table 2-10. If we adopt the middle of the olivine mantle array for the NiO content of the mantle (Fig. 2-17), the estimated pressures increase by 0.1 GPa, which is within the uncertainty of our pressure estimation.

There are barometers based on Si-activity models (Putirka, 2008; Lee et al., 2009). We applied the model of Putirka (2008) to melt compositions produced in experiments at 6 GPa by

Walter (1998) and found that the barometers give lower pressure (4.1 – 4.9 GPa). Moreover, there is a negative correlation between the difference of experimental and calculated pressures (ΔP) and temperatures (e.g., ΔP = +1.1 GPa at 1800 °C and +1.9 GPa at 1710 °C). Therefore, these barometers may not be applicable to pressures close to 6.0 GPa particularly for temperatures lower than ~1700 °C, the condition of which can be realized by the decline of solidus owing to the presence of water. We, therefore, use Fig. 2-21 to estimate melt segregation pressures.

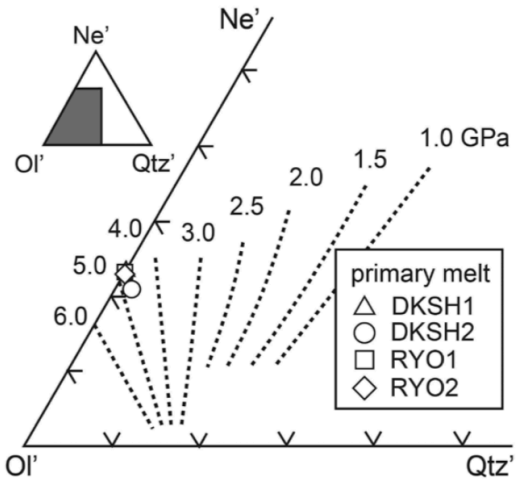

Fig. 2-21: Normative composition of the primary melts estimated from 4 dikes (Table 2-8; DKSH1, open triangle; DKSH2, open circle; RYO1, open square; and RYO2, open diamond) plotted in the Ne'-Ol'-Qtz' ternary diagram barometer (Fig. 2-20).

Melting/melt segregation temperature is firstly estimated for the dry case by applying thermometer based on MgO content in the primary melt (Sakuyama et al., 2014):

$$T = 1080.7 + 54.75(-0.27074P^2 + 2.21634P - 0.99731) + 15.08MgO \qquad (1),$$

where T is the temperature in °C, P is the pressure in GPa, and MgO is MgO content of the melt in wt%. The estimates for the dry case are listed in Table 2-11. The presence of amphibole in the dikes, however, indicates an involvement of water in the melting. The water contents of primary melts constrained above are used to correct the effect of water on melting pressures according to Sakuyama et al. (2009) by the following formula after Tatsumi et al. (1983):

$$P^{wet} = P^{dry} + H_2O^{primary} \times \frac{0.5}{3.0} \quad (2),$$

where P^{wet} and P^{dry} are melting pressures in the wet and dry cases, respectively, in GPa and $H_2O^{primary}$ is the H_2O content in the melt in wt%, and the effect on temperature according to Medard and Grove (2008):

$$T^{dry} - T^{wet} = 40.4C_{H2O}^{melt} - 2.97\left(C_{H2O}^{melt}\right)^2 + 0.0761\left(C_{H2O}^{melt}\right)^3 \quad (3),$$

where T^{wet} and T^{dry} are melting temperatures in the wet and dry cases, respectively, in ℃, and $C^{melt}{}_{H2O}$ is the H_2O content in the melt in wt%. The melt segregation temperatures and pressures corrected for the water effects are 1420 – 1430 °C and 4.9 – 5.0 GPa, respectively, and are listed in Table 2-11. Degrees of melting were estimated for the four dikes by two methods. One is based on the dependence of Ne' on melting degree, which is constrained from melting experiments on depleted mantle compositions (0.28 – 0.30 Na_2O wt%) with reports of melt fractions (Walter 1998, Laporte et al. 2004, and Hirose and Kushiro 1993, with the correction made by Hirschmann 2000) (Fig. 2-22). This method gives 7.1 – 8.7 ± 3.5 % of degree of melting for the four dikes (DKSH1, DKSH2, RYO1, and RYO2) (Fig. 2-22 and Table 2-11). The other is based on the relationships between (Nd/Sm)n and (Dy/Yb)n using the open-system fractional melting model (Ozawa, 2001) and the partition coefficients listed in Table 2-9, and yields a degree of melting of 13.7 – 20.0 ± 3.8 % (Table 2-11). The water concentrations in the mantle

source thus range from 0.04 ± 0.02 to 0.18 ± 0.07 wt% for a 7.1 – 8.7 % degree of melting, and from 0.11 ± 0.02 to 0.31 ± 0.08 wt% for a 13.7 – 20.0 wt% degree of melting. It is expected that such amounts of water present in the mantle source at ~5 GPa is mostly partitioned into the melt once the solidus is reached because of the extremely high solubility of the melt at such high pressure (e.g., ~27 H_2Owt% at 3 GPa, Hodges (1974)), and that the melting degree does not increase much with further decompression. The plausible ranges of the degree of melting and water content in the source will be constrained below by comparing the solidus conditions with the water-preset solidi.

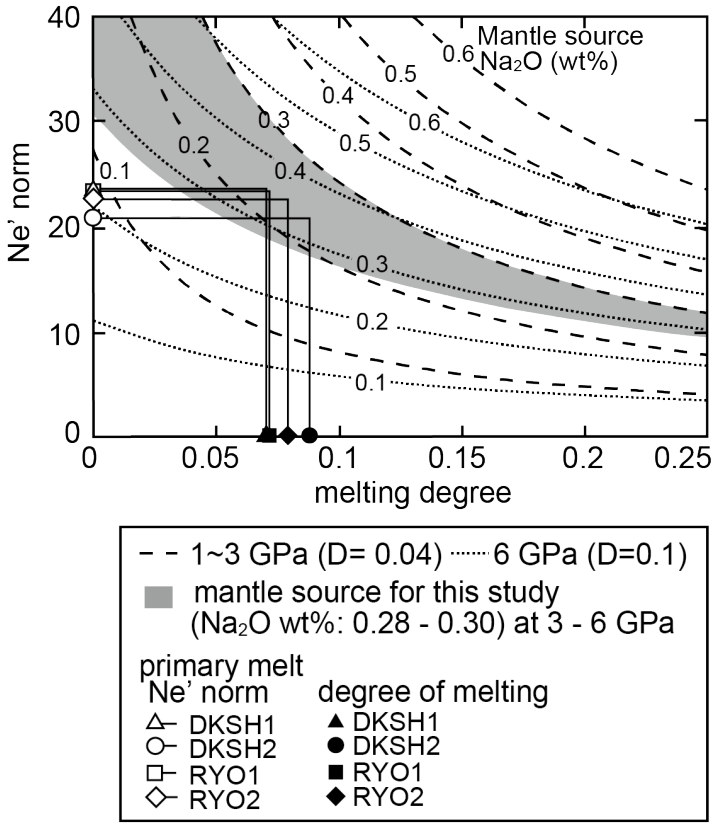

Fig. 2-22: Relationship between normative values of Ne' of primary melt (C_m) and degree of melting (f) for a given Na_2O content of mantle source (C_s) at two pressure ranges (1 – 3 GPa, dashed lines, and 4 – 6 GPa, dotted lines). The dashed lines ($C_m = aC_s/(0.04+0.96f)$, a=11) are based on the experiments at 1 – 3 GPa (Laporte et al, (2004); Hirose and Kushiro (1993) recalculated according to Hirschmann (2000)) and the dotted lines ($C_m = aC_s/(0.1 + 0.9f)$, a =11) are based on experiments at 4 – 6 GPa (Walter, 1998). The gray region represents the range for the MORB mantle source (0.28 – 0.3 Na_2O wt%: Workman and Hart, 2005; Takahashi, 1986) at 3 – 6 GPa. Open and solid symbols connected with each other represent Na_2O content of the primary melts and estimated degrees of melting for four dikes (DKSH1, triangle; DKSH2, circle; RYO1, square; and RYO2, diamond).

From the melting/melt segregation conditions, we further estimated solidus conditions by assuming adiabatic (decompressional) melting, which is the plausible melting mechanism, as discussed above. We extrapolate the melt segregation conditions to the solidus by the melting

degrees obtained above by the two methods and the latent heat of melting according to the following equation after Asimow et al. (1997):

$$\left(\frac{\partial T}{\partial P}\right)_S = \frac{T\{\alpha^s V^s + F(\alpha^{lq} V^{lq} - \alpha^s V^s)\} + \Delta H \left(\frac{\partial F}{\partial T}\right)_P \left(\frac{\partial T}{\partial P}\right)_F}{C_p^s + F\Delta C_p + \Delta H \left(\frac{\partial F}{\partial T}\right)_P} \qquad (4),$$

where T is the temperature in K, P is the pressure in GPa, F is the melting degree, ΔH is the enthalpy change of melting reaction in J/Mol, α^s, and α^{lq} are the thermal expansions for solid and melt, respectively, in 1/K, V^s, and V^{lq} are the partial molar volumes for solid and melt, respectively, in J/GPa, and Cp^s and Cp^{lq} are the isobaric heat capacities for solid and melt, respectively, in J/Mol/K. We used expressions for thermal expansion, molar volume, heat capacity, and enthalpy of fusion according to Lange and Carmichael (1987), Fei (1995), Berman and Brown (1985), Berman (1998), Stebbins et al. (1984), Kojitani and Akaogi (1997). The calculated adiabatic gradients and parameters used in the estimation procedures are listed in Table A5 after King (1957), Krupka et al. (1985), Robie et al. (1982a, 1982b), Haselton and Westrum (1980).

All the solidus conditions calculated by using the degrees of melting estimated by the two methods are plotted between the water-present solidi for 0.05 and 0.1 H_2O wt% after Katz et al. (2003) (~0.08 wt%; Fig. 2-23). The water content of 0.08 wt% in the source is, however, more consistent with that based on the degree of melting estimated from the Ne' norm (0.04 ± 0.02 to 0.18 ± 0.07 wt% H_2O in the source) than that estimated from the REE contents (0.11 ± 0.02 to 0.31 ± 0.08 wt% H_2O). The higher melting degree based on the REE modeling may be attributed to a slightly more depleted source or more effective melt separation. We thus accepted the former estimates for the solidus conditions more plausible, which range from 1440 – 1460 ± 30 °C and 5.3 – 5.4 ± 1.0 GPa (Table 2-11). The errors are estimated by propagating the largest uncertainty

in the estimation of the melting pressures and temperatures. The solidus temperatures are higher than those of melt segregation by 20 to 25 °C according to Takahashi et al. (1993) (Table A5). The estimated solidus pressure indicates that the melting initiated deeper than ~170 km. These deep melting conditions are consistent with the conditions of high-pressure melting inferred from the REE patterns of primary melts (> 75 % of the total melting in the garnet stability field > ~2.5 GPa).

The estimated mantle potential temperatures (MPTs) range 1340 – 1360 ± 40 °C (Table 2-11) by extrapolating the solidus condition to the surface along the adiabatic slope of the solid mantle, 18 °C/GPa (Katsura et al., 2009). The errors are estimated by propagating the uncertainty in the estimation of the solidus temperature and pressure. It should be noted that the decompressional melting at a depth as deep as ~170 km under the globally similar thermal state of the upper mantle as documented in this study requires the initial presence of H_2O-rich fluid or introduction during the melting, which will be discussed next. Even if decompression took place at such a high pressure, dry mantle under the global thermal state did not melt. It also should be noted that the estimation of water content in mantle-derived magmas is imperative and requisite to estimate MPTs in arc environment.

Table 2-11: Segregation conditions (pressures, temperatures, and degrees of melting) of estimated primary melts for the examined four dikes and their solidus conditions (pressures and temperatures) and mantle potential temperatures.

Dike	DKSH1	DKSH2	RYO1	RYO2	1SE
Segregation conditions					
before H_2O correction					
T (℃)	1490	1510	1470	1440	30
P (GPa)	4.7	4.7	4.8	4.9	1.0
after H_2O correction					
T (℃)	1430	1430	1430	1420	30
P (GPa)	5.0	5.0	4.9	5.0	1.0
degree of melting [1] (wt%)					
Ne' norm	7.1	8.7	7.1	7.5	3.5
REE ratios	18.5	16.8	19.7	16.3	3.8
Solidus condition					
T (℃)	1440	1460	1450	1440	30
P (GPa)	5.3	5.4	5.3	5.3	1.0
Mantle potential temperature (℃)	1350	1360	1350	1340	40

Notes: The solidus conditions were estimated by assuming an adiabatic decompressional melting. The standard errors listed in the last column (1SE) were estimated by propagating the uncertainty in the pressure and temperature estimation, which overwhelms the other uncertainties.

[1] The degree of melting was estimated by two methods. One is based on the dependence of Ne' normative composition on melting degree (Ne' norm) and the other is based on the relationships between REE ratios (REE ratios). We adopted the melting degree based on the Ne' norm to calculate solidus conditions and potential temperatures. See the main text for the reasons and more details.

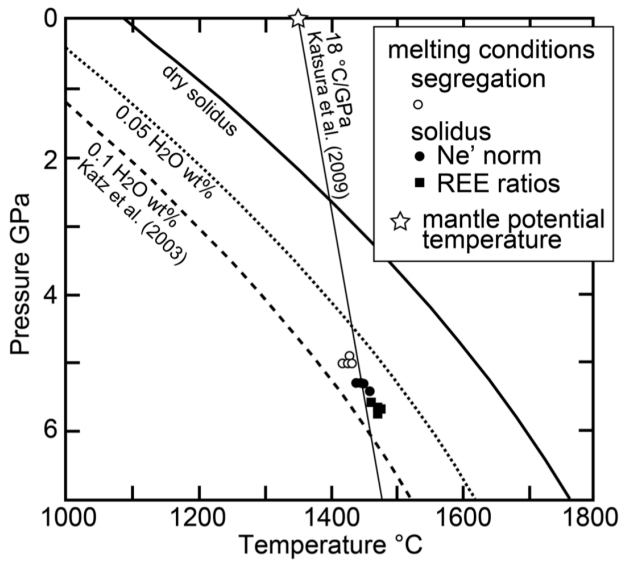

Fig. 2-23: Estimated melting conditions and mantle potential temperature (MPT) for the ultramafic dikes compared with the water-present solidi after Katz et al. (2003). The solidus conditions (solid circles and squares) are estimated from the segregation conditions (open circles: 1420 – 1430 °C, 4.9 – 5.0 GPa), the melting adiabats (Table A5), and the melting degrees estimated by two methods. We obtained the solidus conditions as 1440 – 1460 °C, 5.3 – 5.4 GPa, and 0.04 – 0.18 H_2Owt% in the mantle source (solid circles) by using melting degree of 7.1 – 8.7 % based on the Ne' norm (Fig. 2-22) and as 1460 -1480 °C, 5.6 – 5.8 GPa, and 0.11 – 0.31 H_2Owt% in the mantle source (solid squares) by using melting degree of 13.7 – 20.0 % based on the relationships between (Nd/Sm)n and (Dy/Yb)n. The solidus conditions are plotted along the water-present solidus for ~0.08 wt% H_2O according to Katz et al. (2003). The water content is more consistent with that calculated by using Ne' norm. We, therefore, accepted the former melting conditions more plausible, and the mean temperature and pressure (~1450 °C and ~5.3 GPa) give MPT of ~1350 °C by extrapolating to 1 bar along the solid mantle adiabat (18 °C/GPa; Katsura et al., 2009).

2.8.7 Evaluation of openness of the melting systems

We successfully reproduced the REE pattern of the estimated primary melt of dike DKSH2 by the near fractional melting model with the DMM source and without material influx

(Fig. 2-19). However, highly incompatible trace elements cannot be fitted reasonably well. The estimated water contents of the mantle source (0.04 – 0.18 wt%), which are notably higher than the MORB mantle source (~0.02 wt%: Dixon et al., 1998), indicate the presence of water as hydrous phase before melting or the influx of a H_2O-bearing agent during melting. Therefore, it is quite plausible that a water-bearing agent enriched in highly incompatible elements was added before and/or during melting processes. We estimated the ratios of the highly incompatible elements (Ba, Sr, Nb, and Ta) of the influxed agent required to reproduce those of the primary melt of dike DKSH2 by an open-system near fractional melting model (Ozawa, 2001) with the same model parameters adopted to reproduce less incompatible trace elements above except for assuming material influx before or during decompressional melting. The required chondrite-normalized ratios ((Ba/Nb)n, (Ba/Ta)n, (Sr/Nb)n, and (Sr/Ta)n) of the agent fall within a narrow range (2.1 – 4.5) irrespective of influx timing. The ratios of partition coefficients between solid mantle and water-rich fluids at low temperature (< 900 °C), for pairs of Ba-Nb, Ba-Ta, Sr-Nb, and Sr-Ta, are 12 – 110, 24 – 350, 5.0 – 6.1 and 12 – 19, respectively, and are much higher than for those of a hydrous silicate melt or a supercritical fluid (0.9 – 2.1, 1.3 – 2.9, 0.7 – 1.6 and 1.0 – 2.2, respectively, at 1200 °C) (Kessel et al., 2005). This implies that the water-rich agent should be a hydrous silicate melt or a supercritical fluid. The latter is stable at a pressure higher than ~4 GPa (Mibe et al., 2007), which is consistent with the estimated melting depth > ~130 km.

2.9 Discussion

2.9.1 Slab breakoff tectonics

2.9.1.1 Constraints for the tectonics in the Cambrian-Ordovician northeast Japan

The tectonic environment of the decompressional melting of the depleted mantle from ~170 km depth involving a limited influx of supercritical fluid is not realized in a mantle wedge at steady-state subduction. Therefore, the geochemical characteristics of the ultramafic dikes, distinct from such arc magmas, cannot be explained by melting in the mantle wedge (Table 2-12). Neither back-arc basin spreading nor ridge subduction setting are plausible tectonic environment for primary magmas of the ultramafic dikes because their depths of melting are as shallow as 30 – 100 km (e.g., Yamashita and Tatsumi, 1994; Wiens et al., 2006) (Table 2-12). A deep upwelling of hotter mantle producing hotspot magmatisms is not plausible because such intraplate magmatisms are characterized generally by an enriched mantle source (e.g., Sun and McDonough, 1989; Putirka, 2005; Ernst and Buchan, 2003) (Table 2-12). Hotspot volcanisms generated by melting of depleted mantle source derived from the deep mantle have been advocated to explain depleted geochemical signatures of some hotspot magmas (Kerr et al. 1995). However, such possibility for the ultramafic dikes of the Hayachine-Miyamori ophiolite would be argued against below by comparing the potential temperature estimated from the ultramafic dike with those estimated from mid-ocean ridge magmas. Therefore, any of these common tectonic environment for magma generation in the upper mantle are not responsible for the formation of primary magmas for the ultramafic dikes. The only remaining mechanism is slab breakoff tectonics, which induces mantle upwelling as counterflow of sinking slab. We call this as “slab breakoff model”.

The extensive flux melting of the mantle wedge forming the CRUS of the Tectonite Member had occurred in the Cambrian-Ordovician northeast Japan just before decompressional melting of the depleted mantle forming the Cumulate Member and the ultramafic dikes. Such

sudden change of the melting regimes from extensive flux melting to adiabatic decompressional melting of the depleted mantle at the depth of ~170 km is consistent with the slab breakoff model.

Table 2-12: The comparison of melting conditions (melting mechanism, mantle source, melting depth) for this study and those of representative magma generation environments. Data sources of [1], [2], [3], [4], [5], [6], and [7] are Kuritani et al. (2014a, 2014b), Till et al. (2012), Yamashita and Tatsumi (1994), Wiens et al. (2006), Putirka (2005), and Lee et al. (2009), respectively.

	This study	Steady-state arc		Mid-ocean ridge	Hotspot
		volcanic arc	back-arc		
Melting mechanism & Mantle source	decompressional melting of depleted mantle	flux melting of wedge mantle	decompressional melting of depleted mantle	decompressional melting of depleted mantle	decompressional melting of enriched mantle
Melting depth (km)	170	30 - 120	30 - 100	30 - 100	40 - 200
Data source	-	[1], [2], [3]	[4], [5]	[5], [6], [7]	[6], [7]

A slab breakoff model invokes a detachment of a subducting oceanic plate which induces upwelling of asthenosphere materials from above or beneath the subducting plate (Davies and von Blanckenburg, 1995). In the former case, distinct geochemical features of the mantle wedge must be inscribed in the primary melt, but it is not the case for the Cumulate Member and the ultramafic dikes as discussed above. Therefore, mantle upwelling must be dominated from the bottom side of the plate. This is consistent with results of geodynamic modeling of slab breakoff (Gerya et al., 2004; Menant et al., 2016), where a substantial upwelling takes place from beneath the subducting plate.

Ozawa et al. (2015) proposed a model that the Cumulate Member was crystallized from melts formed by decompressional melting of a sub-slab mantle triggered by a slab breakoff

during the Cambrian-Ordovician time in northeast Japan Arc. The slab breakoff model constrained in our study is not in conflict with this model. Figure 2-24 shows a tectonic model based on Ozawa et al. (2015) with our proposition of generation and transportation of the primary magma frozen as the ultramafic dikes in the Cumulate Member. The estimated relationships between the slab breakoff tectonics and deep upwelling of sub-slab mantle are generally recognized in the present-day subduction environments, as documented in the next section.

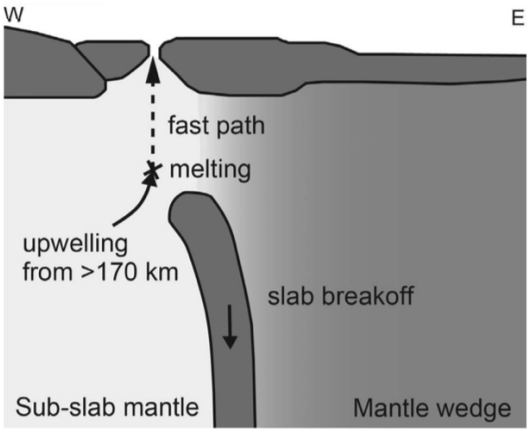

Fig. 2-24: Slab breakoff model in the latest stage of the Hayachine-Miyamori ophiolite evolution during the Cambrian-Ordovician time constrained by melt generation depths, mantle source compositions, and melting mechanism for the primary melt, the composition of which was estimated from the four ultramafic dikes in this study. Passive upwelling (thick arrow) of the sub-slab mantle from >170 km depth is assumed to have been triggered by slab breakoff (Ozawa et al., 2015). Thin gray arrow shows melt transport through a fast path. Abbreviations: E, east; W, west.

2.9.1.2 Present-day slab breakoffs

As mentioned in the general introduction, slab rupture, including slab breakoff, slab detachment, slab tear, slab window, and slab fragmentation, has been documented from the present-day subduction zones by geophysical observations (Nolet, 2009). Since the first documentation of slab rupture in the Mediterranean (Spakman, 1986; Spakman et al., 1988), slab ruptures have been reported from more than 30 worldwide subduction zones (see Fig. 1-3). Recent seismic tomography models imaged slab detachments at a depth of ~60 and ~130 km beneath the Mount Etna in southern Italy (Fig. 2-25a; Barreca et al., 2020; Scarfi et al., 2018), and a slab tear at ~120 km depth at the northern Central Kamchatka depression volcanic zones (CKDV) in the Kamchatka-Aleutian junction (Figs. 2-25b-1– b-3; Koulakov et al., 2020; Levin et al., 2002). Slab tear and slab detachment beneath southern Iberia in the western Mediterranean and northwestern Africa were imaged by seismic tomography models and electrical resistivity structure at depths shallower than ~50 to 300 km (Figs. 2-25c-1– c-4; e.g., Seber et al., 1996; de Lis Mancilla et al., 2015; Heit et al., 2017; Rosell et al., 2011; Garcia-Castellanos and Villasenor, 2011).

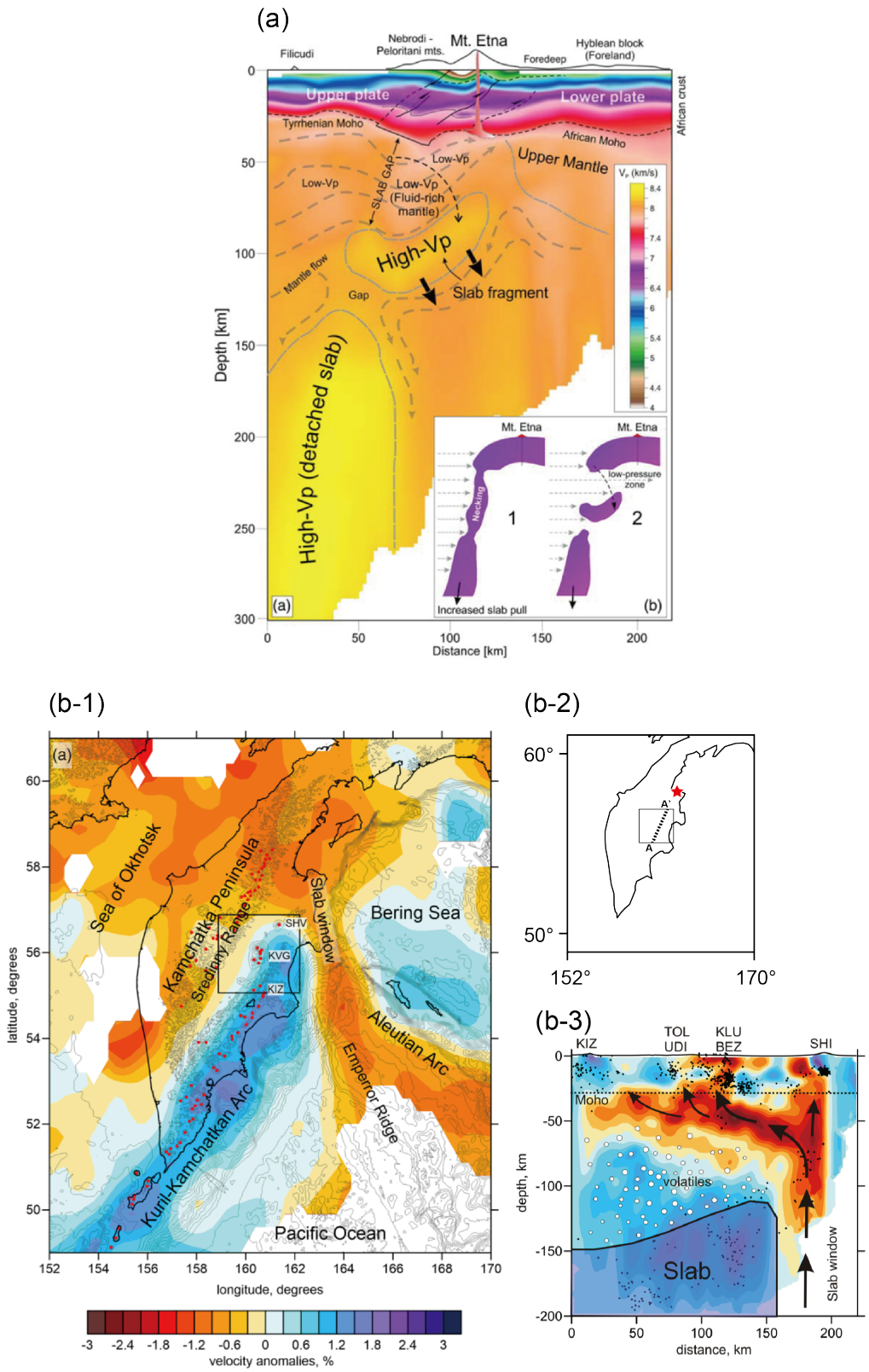
(a)
Filicudi
Nebrodi - Peloritani mts.
Mt. Etna
Foredeep
Hyblean block (Foreland)
Upper plate
Lower plate
African crust
Tyrrhenian Moho
African Moho
Upper Mantle
Low-Vp
SLAB GAP
Low-Vp (Fluid-rich mantle)
High-Vp
Slab fragment
Mantle flow
Gap
High-Vp (detached slab)
Depth [km]
Distance [km]
Mt. Etna
low-pressure zone
Necking
1
2
Increased slab pull
(a)
(b)
(b-1)
Sea of Okhotsk
Kamchatka Peninsula
Sredinny Range
Slab window
Bering Sea
SHV
KVG
KIZ
Aleutian Arc
Emperor Ridge
Kuril-Kamchatkan Arc
Pacific Ocean
latitude, degrees
longitude, degrees
velocity anomalies, %
(b-2)
60°
50°
152°
170°
A'
A
(b-3)
KIZ
TOL
UDI
KLU
BEZ
SHI
Moho
volatiles
Slab
Slab window
depth, km
distance, km

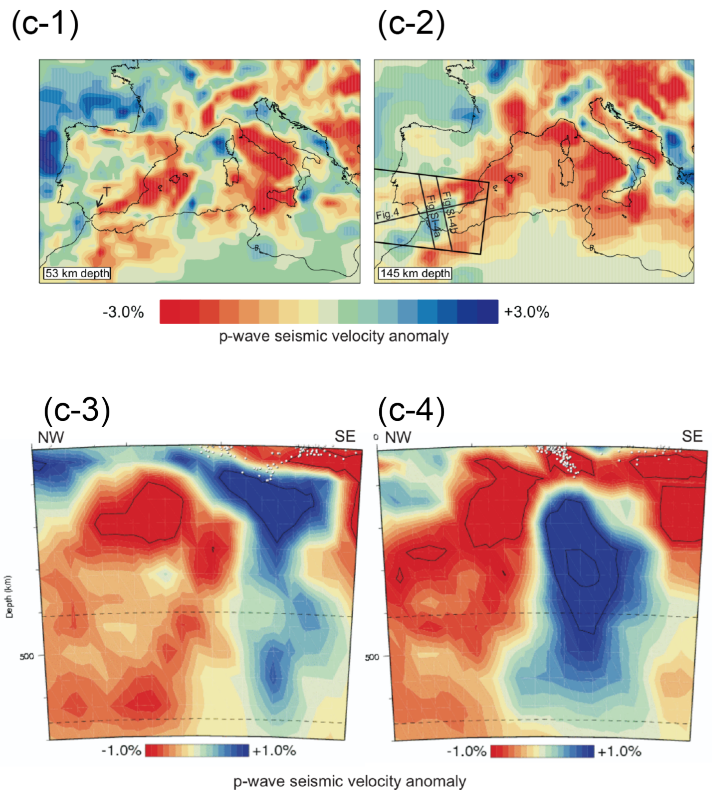

Fig. 2-25: Regional seismic tomography models in (a) southern Italy (Barreca et al., 2020; Scarfi et al., 2018), (b) Kamchatka-Aleutian junction (Koulakov et al., 2011), and (c) western Mediterranean (Garcia-Castellanos and Villasenor, 2011). (a) Tectonic interpretations of Barreca et al. (2020) shown in the vertical section of Vp model after Scarfi et al. (2018), in which fragmented slab and associated gap north of Mount Etna in southern Italy as illustrated by the inset based on the tomography. (b-1) A horizontal section at 150 km depth of the Vp model of surrounding area of the Kamchatka-Aleutian junction after Koulakov et al. (2011). Red dots indicate locations of monogenic cones (Churikova et al., 2015; Volynets et al., 1998). (b-2) Outline of the Kamchatka Peninsula in the same area of Fig. 2-25b-1. Red solid star indicates the Nachikinsky volcano. A square indicates the same region of the square marked in Fig. 2-25b-1. (b-3) A vertical section of the Vs model after Koulakov et al. (2020) along A - A' in Fig. 2-25b-2. Black arrows show trajectories of possible flow in the mantle wedge, and the dotted line shows approximate location of the Moho (Koulakov et al., 2020). (c-1) A horizontal slice of the tomographic model at 53 km depth in western Mediterranean after Garcia-Castellanos and Villasenor (2011) and (c-2) that at 145 km depth. (c-3) A vertical tomographic profile along "Fig. S1-4a" and (c-4) "Fig. S1-4b" marked in Fig. 2-25c-2. The location of lithospheric tearing is indicated by "T" in (c-1) (Garcia-Castellanos and Villasenor, 2011).

The magmas erupted at the Mount Etna (0.6 Ma – present; Fig. 2-25a) are chemically diverse ranging from tholeiite to alkali olivine basalts, both of which show enriched LREE, depleted HREE, and MORB-like isotopic ratios of Ne, He, C and Nd (Table 2-13; Peccerillo 2005; Nakai et al., 1997; Allard et al., 1997; Armienti et al., 1988, 2004; Marty et al., 1994). The tholeiite magmas and alkali olivine basalts are thought to have been generated at different depths by small degree of melting of depleted mantle via adiabatic decompression. The tectonic process responsible for the magma generation has been attributed to upwellings of sub-slab asthenosphere through the slab windows (e.g., Gvirtzman and Nur, 1999; Rosenbaum et al., 2008; Doglioni et a., 2001; Peccerillo, 2005; Armienti et al., 2004). Spatial geochemical variations of late Pleistocene–Holocene lavas erupted along the CKDV (Figs. 2-25b-1 – b-3) are clarified by Portnyagin et al. (2005, 2007). Alkali olivine basalts of the Nachikinsky volcano in the northern end of the CKDV show enriched LREE, depleted HREE, and MORB-like isotopic ratios of Sr, Nd, and O (Table 2-13), whereas the magmas erupted in the main southern part of the CKDV are characterized by the involvement of slab-derived fluid. The alkali olivine basalts of the Nachikinsky volcano are proposed to have formed by a low degree of melting of depleted garnet-bearing mantle (> ~75 km) by adiabatic decompression at temperature well exceeding 1300 ℃ (Portnyagin et al., 2005, 2007). Portnyagin et al. (2005, 2007) attributed the magma genesis to upwelling of asthenosphere through the slab window. The alkali olivine basalts of the southern Iberia and northwestern Africa erupted at 6.3 – 0.65 Ma (Figs. 2-25c-1 – c-4) show enriched LREE, depleted HREE, MORB- or HIMU-like isotopic ratios of Sr and Nd, and HIMU-like Pb isotopic ratios (Table 2-13; El Azzouzi et al.,1999; Duggen et al. 2005; Bosch et al., 2014). They are inferred to be products of low degree of partial melting of plume-contaminated mantle at

depths ranging from 40 to 100 km by decompressional melting (El Azzouzi et al.,1999; Duggen et al. 2005). The magma generation is attributed to upwelling of sub-slab asthenosphere through the windows.

Table 2-13: Representative present-day isotope ratios and REE and trace element ratios of lavas from the volcanos occurring above the slab raptures documented by geophysical observations in southern Italy, northwestern Africa, and Kamchatka. Data sources of [1], [2], [3], [4], [5], [6], [7], [8] and [9] are Armienti et al. (2004), Nakai et al. (1997), Allard et al. (1997), Marty et al. (1994), Bosch et al. (2014), El Azzouzi et al. (1999), Duggen et al. (2005), and Portnyagin et al. (2005, 2007), respectively.

Region	Southern Italy		Northwestern Africa		Kamchatka
Location	Mount Etna		Mount Atlas	Guilliz	Nachikinsky volcano
Sample	Tholeiite	Alkali olivine basalt	Alkali olivine basalt	Alkali olivine basalt	Alkali olivine basalt
$^{143}Nd/^{144}Nd$	0.512924	0.512954	0.512863	0.512905	0.512984
$^{87}Sr/^{86}Sr$	0.70315	0.70308	0.70337	0.70306	0.70330
$^{208}Pb/^{204}Pb$	39.110	39.440	39.334	38.736	37.837
$^{3}He/^{4}He$	6.38		-	-	-
$^{20}Ne/^{22}Ne$	10.69		-	-	-
$^{21}Ne/^{22}Ne$	0.0367		-	-	-
$\delta^{13}CO_2$	-4.0		-	-	-
$\delta^{18}O$	5.1		-	-	5.14
(Ba/Ti)n	2.98	9.07	8.72	7.97	2.16
(Ce/Nd)n	0.92	0.84	0.70	0.48	0.57
(Nd/Sm)n	1.41	1.66	1.89	1.71	1.34
(Dy/Yb)n	1.61	1.64	1.87	1.45	1.53
Data source	[1], [2], [3], [4]		[5]	[6], [7]	[8], [9]

We estimated melting pressures and MPTs of the tholeiite and alkali olivine basalt of the Mount Etna, whose whole-rock chemical compositions are listed in Table 2-14 (Armienti et al., 1988, 2004), alkali olivine basalt of the Nachikinsky volcano (Table 2-14; Portnyagin et al., 2005, 2007) and alkali olivine basalt of northwestern Africa (Table 2-14; El Azzouzi et al.,1999)

by the same methods adopted in the section **2.8**. The estimated pressures are ~1.8 GPa (~ 50 km) and ~3.4 GPa (~100 km) for the tholeiite and alkali olivine basalt of the Mount Etna, respectively, ~3.1 GPa (~90 km) for the Nachikinsky volcano, and ~3.7 GPa (~110 km) for the northwestern Africa by assuming water contents of 0.04 – 0.23 wt% in the mantle sources (Table 2-15). The estimated MPTs range from ~1300 to ~1370 °C (Table 2-15) by assuming the same range of water contents. These values are consistent with the geophysically imaged depths of slab detachments (Table 2-15). This indicates that decompressional melting induced by deep upwelling of sub-slab upper mantle to fill the gaps of ruptured slabs is actually taking place even in the present-day subduction zones.

Table 2-14: The least fractionated melt compositions of lavas from Mount Etna in southern Italy, Mount Atlas and Guilliz in northwestern Africa, and Nachikinsky volcano in Kamchatka. Their primary melt compositions are estimated by the same method used in section **2.8.5**. The primary melt composition for the Nachikinsky volcano is estimate after Portnyagin et al. (2007). Major element oxides are recalculated to 100 wt % volatile free and $Fe^{3+}/(Fe^{2+} + Fe^{3+}) = 0.1$. The chemical compositions of residue olivine constrained in the modeling are also listed.

Region	Southern Italy		Northwestern Africa		Kamchatka
Location	Mount Etna		Mount Atlas	Guilliz	Nachikinsky volcano
Type	Tholeiite	Alkali olivine basalt	Alkali olivine basalt	Alkali olivine basalt	Alkali olivine basalt
Sample	et167[1]	et75[1]	MA409[2]	KH41[3]	Mean[4]
Less fractionated magma					
Major oxides (wt%)					
SiO_2	49.36	47.94	46.40	44.95	48.46
TiO_2	1.48	1.61	2.21	3.25	2.09
Al_2O_3	17.26	16.43	12.41	13.15	14.84
FeO	8.65	8.94	9.85	8.85	10.18
MnO	0.15	0.20	0.20	0.18	0.09
MgO	8.76	7.83	12.16	9.15	9.59
CaO	9.30	11.78	10.13	12.23	9.59
Na_2O	3.21	2.54	3.16	2.88	3.26
K_2O	0.35	1.24	1.26	3.51	0.25
P_2O_5	0.38	0.36	0.90	0.69	0.36
Fe_2O_3	1.07	1.10	1.22	1.09	1.26
NiO	0.02	0.01	0.04	0.02	0.03
Cr_2O_3	-	0.02	0.07	0.05	-
Total	100.00	100.00	100.00	100.00	100.00
Primary melt					
Major oxides (wt%)					
SiO_2	48.87	45.75	46.40	43.81	45.71
TiO_2	1.43	1.31	2.21	2.97	1.72
Al_2O_3	16.70	13.43	12.41	12.04	12.21
FeO	8.72	9.17	9.85	8.87	9.76
MnO	0.15	0.20	0.20	0.18	0.08
MgO	9.76	14.10	12.16	11.48	14.95
CaO	9.00	9.63	10.13	11.19	7.91
Na_2O	3.11	2.07	3.16	2.63	2.68
K_2O	0.34	1.02	1.26	3.22	1.04
P_2O_5	0.37	0.30	0.90	0.63	0.30
Fe_2O_3	1.03	0.90	1.22	1.00	1.21
NiO	0.03	0.04	0.04	0.03	-
Cr_2O_3	-	0.01	0.07	0.05	-
Total	100.00	100.00	100.00	100.00	100.00
Norm components[5]					
Ne'	30.1	23.0	35.3	41.2	26.1
Qtz'	24.0	12.5	13.3	0.0	13.5
Ol'	45.9	64.5	51.4	58.8	60.4
Olivine in equilibrium with primary melt					
Mg#	0.87	0.90	0.88	0.89	0.90
Added mass (wt%)	2.8	17.7	0.0	6.8	13.1

[1]The data are after Armienti et al. (2004).
[2]The data are after Bosch et al. (2014).
[3]The data are after El Azzouzi et al. (1999).
[4] mean compositions of 20 melt inclusions and their primary melts calculated by Portnyagin et al. (2007)
[5] C. I. P. W norm mineral components calculated from primary melt (Ne'= nepheline + 0.6albite, Ol'= olivine + 0.75orthopyroxene and Qtz'= Quartz + 0.4albite + 0.25orthopyroxene)

Table 2-15: Segregation conditions (pressures, temperatures, and degrees of melting) of the estimated primary melts for the Mount Etna in southern Italy, Mount Atlas and Guilliz in northwestern Africa, and Nachikinsky volcano in Kamchatka, and their solidus conditions (pressures, temperatures, and water contents in source) and MPTs. The solidus conditions were estimated by assuming an adiabatic decompressional melting. Depths of the imaged slab ruptures inferred beneath the volcanos are also shown for comparison.

Region	Southern Italy		Northwestern Africa		Kamchatka
Location	Mount Etna		Mount Atlas	Guilliz	Nachikinsky volcano
Sample[1]	et167	et75	MA409	KH41	Mean
Segregation condition					
T (℃)	1290	1390	1380	1430	1380
P (GPa)	1.4	2.9	2.2	4.9	2.7
Degree of melting	0.07	0.11	0.06	0.04	0.09
Solidus condition					
T (℃)	1330	1430	1410	1450	1410
P (GPa)	1.8	3.4	2.4	5.3	3.1
Depth (km)	60	110	80	170	100
H_2O in source (wt%)	0.04	0.23	0.03	0.08	0.22
MPT (℃)	1300	1370	1360	1350	1360
Depths of slab ruptures (km)	~60 and ~130 [2]		~50 to ~300 [3]		~120 [4]

[1]Samples are same as in Table 2-13.

[2] The data afterBarreca et al. (2020) and Scarfi et al. (2018).

[3] The data after Garcia-Castellanos and Villasenor (2011), Heit et al. (2017), and de Lis Mancilla et al. (2015).

[4] The data are after Koulakov et al. (2020) and Levin et al. (2002).

2.9.2. The thermal state of the upper mantle

2.9.2.1 The present-day thermal state of the upper mantle

The present-day MPT varies from 1370 ± 49 °C for mid-ocean ridges to 1620 ± 55 °C for ocean island basalt (Putirka, 2005). The former magma generation is induced by passive upwelling, and the latter by active upwelling. Thus, the wide variation of the present-day MPT

implies the diversity in the depths of mantle upwelling. It should be noted that the estimated MPTs are within the range of 1350 – 1450 °C if the magma generation mechanism is restricted to passive upwelling regardless of whether it occurs beneath mid-ocean ridges or back-arc basins (Wiens et al., 2006). This implies that the upper mantle is globally in a fairly homogeneous thermal state, which might be maintained by small-scale convection underneath the plates (Richter and Parsons, 1975) as suggested by numerical modeling and geophysical observations, such as reduction of oceanic seismic anisotropy with age (van Hunen and Čadek, 2009) and significant deviation of the azimuthal anisotropy in the LVZ from the current plate motion direction (Takeo et al., 2018).

The small-scale convection is known to be unstable if the surface heat flux is as low as < 10 – 20 mW/m^2 (Solomatov and Moresi, 2000), which is 1/5 – 1/2 of the values for the present-day old oceanic lithosphere, 40 – 50 mW/m^2 (Furlong et al., 2013; Davaille and Jaupart, 1994; Lister et al., 1990). The heat flux to cause instability of small-scale convection are not affected by the various uncertainties (e.g., temperature, pressure, and grain size of the asthenosphere; Solomatov and Moresi, 2000). The thermal structures of subducted slabs estimated by global subduction zone thermal models (van Keken et al. 2012; Abers et al., 2013; Peacock 2003) show that the thermal gradient at the bottom of subducted slab above the sub-slab asthenosphere does not change from that of the oceanic lithosphere before subduction so far as the depth is shallower than ~300 km, even if a thin slab (~ 40 km thickness) is subducted. This implies that the heat flux at the bottom of sub-slab asthenosphere may be much greater than 10 – 20 mW/m^2. Therefore, the small-scale convections may be sustained at least in the sub-slab mantle shallower than 300 km.

2.9.2.2 The thermal state of the upper mantle in Cambrian-Ordovician periods

Ophiolites have been classified to subduction-related and subduction-unrelated according to the Th/Yb-Nb/Yb discrimination diagram of Pearce (2008) (e.g., Dilek and Furnes, 2011; Furnes et al., 2014). The subduction-unrelated ophiolites are plotted in the MORB- oceanic island basalt (OIB) array (Dilek and Furnes, 2011), and the subduction-related ophiolites are plotted above the array in the diagram (Dilek and Furnes, 2011; Furnes et al., 2014). The subduction-unrelated ophiolites classified as the mid-ocean ridge-type have the low TiO_2/Yb value in the TiO_2/Yb-Nb/Yb discrimination diagram for mafic rocks (Dilek and Furnes, 2011; Furnes et al., 2014). Examples of the Cambrian-Ordovician mid-ocean ridge-type ophiolites are the Isle de Groix (France; Bernard-Griffiths et al., 1986), Dongcaohe (North China; Tseng et al., 2007), Buqingshan (Qinghai-Tibet Plateau, China; Bian et al., 2004), and Ossa-Morena Zone (Spain; Pedro et al., 2010) (Tables 2-16 and 2-17).

We have estimated the Cambrian-Ordovician MPT of 1350 ± 40 °C in the northeast Japan arc from ultramafic dikes with the specification of melting mechanism as decompression melting of MORB mantle source from the sub-slab mantle. The MPTs in the same period at other region have been estimated from one of rare mid-ocean ridge-type ophiolites to be ~1360 °C (Kimura et al., 2017) and ~1440 °C (Herzberg et al., 2010) (Table 2-16) for the ~460 Ma Isle de Groix ophiolite, France (Bernard-Griffiths et al., 1986) from the estimated primary melt composition (Table 2-18). These MPT estimates distinct from each other were obtained by different methods (Table 2-18). Kimura et al. (2017) applied the OBS2 thermodynamic model to the REE compositions of a primary magma calculated from a mafic rock interpreted to be the MORB (Bernard-Griffiths et al., 1986). Herzberg et al. (2010) applied the relationship of MPTs and MgO

contents of primary magmas (PRIMELT2; Herzberg and Asimow, 2008; Herzberg et al., 2010) to the major and trace element compositions of a mafic rock (Bernard-Griffiths et al., 1986).

We estimated the MPTs for rare mid-ocean ridge-type ophiolites (Table 2-16) in the same age including the aforementioned Isle de Groix ophiolite from the estimated primary melt compositions (Table 2-17). They are Dongcaohe (North China; 500 Ma; Tseng et al., 2007), Buqingshan (Qinghai-Tibet Plateau, China; 470 Ma; Bian et al., 2004), and Ossa-Morena Zone ophiolite (Spain; 480 Ma; Pedro et al., 2010) (Table 2-16). The MPTs obtained by applying our method with assumption of dry decompressional melting range ~1330 – 1410 °C (Table 2-18). Our MPT estimate for the Isle de Groix is ~1410 °C, which is in the middle of the values obtained by Kimura et al. (2017) and Herzberg et al. (2010). The estimated segregation depths range from 60 – 70 km (Table 2-18), which is consistent with the depth of melt segregation for the present-day mid-ocean ridge basalt (e.g., Kinzler and Grove, 1992).

We conclude that the MPTs for the world mid-ocean ridge-type ophiolites of the Cambrian-Ordovician times are 1330 – 1410 °C, and that these MPTs are the same as the MPT for the Hayachine-Miyamori ophiolite from the Cambrian-Ordovician subduction zone. It is unique and important in that it represents MPT from arc environment. More strictly speaking, it represents a MPT of the shallower (< 170 km) sub-slab asthenospheric mantle, but reflects the global thermal state of the Cambrian-Ordovician upper mantle. This is because the thermal state of sub-slab mantle is similar to the normal oceanic sub-lithospheric mantle owing to small-scale convection as discussed above. The coincidence of the MPT estimate from the ultramafic dikes to that of the mantle beneath mid-ocean ridges of the Cambrian-Ordovician times strongly supports the inference that the thermal state of the upper mantle in Cambrian-Ordovician time was globally similar and that it is similar to that of the present-day upper mantle.

Table 2-16: Geological features of the mid-ocean ridge-type ophiolites, which have nearly the same formation ages of ~500 Ma as the Hayachine-Miyamori ophiolite (Isle de Groix, Bernard-Griffiths et al. (1986); Dongcaohe, Tseng et al. (2007); Buqingshan, Bian et al. (2004); Ossa-Morena Zone, Pedro et al. (2010)). Involved magma types and used data for the interpretations are also shown.

Region	Isle de Groix, France	Dongcaohe, North China	Buqingshan, Qinghai-Tibet Plateau, China	Ossa-Morena Zone, Spain
Age (Ma)	460	500	470	480
Ophiolite sequence				
Sediment cover	pelitic rock	-	clay, limestone, chert	chert
Extrusive rock	basaltic rock	basalt	basalt, picrite	basalt
Sheeted dike	-	gabbro, gabbronorite, diabase	diabase	diabase
Mafic cumulate	-	gabbro, troctolite	gabrro	pyroxenite, gabbro
Mantle section	-	dunite	harzburgite	dunite, wehrlite
Magma type	normal MORB − enriched MORB	normal MORB	normal MORB	normal MORB− enriched MORB
Used data	REEs, trace elements	REEs	REEs	REEs, trace elements

Table 2-17: Less fractionated magma and estimated primary melt compositions of the mid-ocean ridge-type ophiolites (Isle de Groix, Dongcaohe, Buqingshan, and Ossa-Morena Zone). Major element oxides are recalculated to 100 wt % volatile free and $Fe^{3+}/(Fe^{2+} + Fe^{3+}) = 0.1$. The chemical compositions of olivine in the residual peridotites are also listed.

Region	Isle de Groix, France	Dongcaohe, North China	Buqingshan, Qinghai-Tibet Plateau, China	Ossa-Morena Zone, Spain
Sample	7839[1]	BG-03A[2]	DL-3[3]	AF-18[4]
Type	Picrite	Basalt	Basalt	Basalt
Less fractionated magma				
Major oxides (wt%)				
SiO_2	46.97	51.83	48.26	49.62
TiO_2	1.19	1.37	1.09	1.48
Al_2O_3	15.38	14.50	18.23	16.86
FeO	9.29	10.21	8.57	8.75
MnO	0.15	0.20	0.20	0.15
MgO	13.51	7.50	9.72	9.71
CaO	10.57	9.21	9.12	7.72
Na_2O	1.53	3.30	3.49	4.41
K_2O	0.12	0.47	0.07	0.04
P_2O_5	0.13	0.12	0.07	0.18
Fe_2O_3	1.15	1.26	1.06	1.08
NiO	-	0.01	0.02	-
Cr_2O_3	-	0.02	0.08	-
Total	100.00	100.00	100.00	100.00
Primary melt				
Major oxides (wt%)				
SiO_2	49.26	50.09	48.21	48.67
TiO_2	1.61	1.17	1.08	1.32
Al_2O_3	13.62	12.33	18.12	15.04
FeO	9.61	10.71	8.59	8.95
MnO	0.16	0.21	0.20	0.15
MgO	14.96	13.22	9.94	13.88
CaO	6.19	7.84	9.07	6.89
Na_2O	3.32	2.81	3.47	3.93
K_2O	0.09	0.40	0.07	0.04
P_2O_5	0.17	0.10	0.07	0.16
Fe_2O_3	1.00	1.07	1.05	0.96
NiO	-	0.04	0.03	-
Cr_2O_3	-	0.01	0.08	-
Total	100.00	100.00	100.00	100.00
Norm components[5]				
Ne'	25.3	24.2	33.1	31.1
Qtz'	21.2	22.2	20.7	19.2
Ol'	53.4	53.6	46.2	49.7
Olivine in equilibrium with primary melt				
Mg #	0.91	0.88	0.88	0.91
Added mass (wt%)	7.8	16.2	0.6	11.4

[1]The data are after Bernard-Griffiths et al. (1986).
[2]The data are after Tseng et al. (2007).
[3]The data are after Bian et al. (2004).
[4]The data are after Pedro et al. (2010).
[5] C. I. P. W norm mineral components calculated from primary melt (Ne'= nepheline + 0.6albite, Ol'= olivine + 0.75orthopyroxene and Qtz'= Quartz + 0.4albite + 0.25orthopyroxene)

Table 2-18: Melting conditions and MPTs estimated from the mid-ocean ridge-type ophiolites formed during the Cambrian-Ordovician ophiolite pulse. We estimated the segregation conditions, solidus conditions, and MPTs for Dongcaohe (Tseng et al., 2007), Buqingshan (Bian et al., 2004), and Ossa-Morena Zone ophiolites (Pedro et al., 2010) by applying our method from the estimated primary magma compositions listed in Table 2-16. The MPTs of the Isle de Groix (Bernard-Griffiths et al., 1986) estimated by Kimura et al. (2017) and Herzberg et al. (2010) are also listed.

Region	Isle de Groix, France	Dongcaohe, North China	Buqingshan, Qinghai-Tibet Plateau, China	Ossa-Morena Zone, Spain
Previous studies				
MPTs (℃)				
Kimura et al. (2017)	1360	-	-	-
Herzberg et al. (2010)	1440	-	-	-
This study				
Segregation condition				
T (℃)	1400	1370	1330	1400
P (GPa)	1.6	1.5	1.6	1.7
Degree of melting	0.09	0.10	0.06	0.07
Solidus condition				
T (℃)	1450	1420	1360	1430
P (GPa)	2.0	2.0	1.9	2.1
Depth (km)	70	60	60	70
MPT (℃)	1410	1380	1330	1390

2.9.3 Origin of the Cambrian-Ordovician ophiolite pulse

The Cambrian-Ordovician ophiolites classified as subduction-related according to the Th/Yb-Nb/Yb discrimination diagram of Pearce (2008) have high Nb/Yb ratios above the MORB-OIB array (Dilek and Furnes, 2011; Furnes et al., 2014). These ophiolites, however, plot mostly in the MORB field in the V-Ti discrimination diagram of Shervais (1982) (Dilek and Furnes, 2011; Furnes et al., 2014). This implies that primary magmas for such ophiolites formed mostly by decompressional melting of a MORB mantle source under negligible influence of slab-

derived fluids. The plausible mechanisms to reproduce such features have been thought to be back-arc spreading (Dilek and Furnes, 2011; Furnes et al., 2014). These back-arc related ophiolites account for > 70 % of the Cambrian-Ordovician ophiolite pulse (Furnes et al., 2014).

We compiled data of volcanic or shallow-intrusive basaltic rocks from the Cambrian-Ordovician back-arc related ophiolites and examined the relationship between the chondrite-normalized ratio of Dy and Yb ((Dy/Yb)n) and that of Nd and Sm ((Nd/Sm)n). They are compared with primary melts formed by steady-state decompressional melting (Ozawa, 2001) of a MORB mantle source that ascent from various depths with a variable extent of melting in the garnet peridotite field, which is represented by PMGF (Figs. 2-26a and 2-26b). The data from the subduction-related Cambrian-Ordovician ophiolites have a similar range of (Nd/Sm)n as that of the present-day NMORB and NBABB, and a wide range of (Dy/Yb)n (0.97 – 1.39) with many data higher than (Dy/Yb)n of the present-day NMORB and NBABB (1.22 – 1.40; Figs. 2-26a and 2-26b). The predominance of magmas that have (Nd/Sm)n and (Dy/Yb)n ratios within the range of the present-day NMORB and NBABB suggests that the Cambrian-Ordovician NMORB or NBABB-like magmas were generated from the MORB mantle source at depths similar to the present-day spreading center (30 – 100 km, Kinzler and Grove,1992; Wiens et al., 2006). It also indicates that the thermal state of the Cambrian-Ordovician upper mantle was not distinct from that of the present-day upper mantle. These are consistent with our estimations of ~1350 °C MPT from the ultramafic dikes of the Hayachine-Miyamori ophiolite, and ~60 – 70 km solidus depths and ~1330 – 1410 °C MPTs from the world Cambrian-Ordovician MORB-type ophiolites (see, section **2.9.2**, Table 2-18).

The (Dy/Yb)n from some of the ophiolites are as high as that of the magmas filling ultramafic dikes in the Hayachine-Miyamori ophiolite (Dy/Yb)n (> 1.2) with (Nd/Sm)n < 1.0

(Fig. 2-26a). Such ophiolites are: Bymarka, Norway (Slagstad, 2003); Solund-Stavfijord, Norway (Furnes et al., 2012); Star Lake, Canada (Lissenberg et al., 2005); Cabo Oltegal Complex, Spain (Sánchez-Martínez et al., 2007); Kudi, China (Fang, 1998; Jiang et al., 1992; Wang et al., 2002). The presence of magmas characterized by the high (Dy/Yb)n (> 1.2) in these ophiolites indicates partial melting of MORB mantle source at depth as deep as ~170 km distinctively deeper than those of the Cambrian-Ordovician mid-ocean ridge-type ophiolites (Table 2-18). It is speculated that these magmas were generated by adiabatic decompression of sub-slab mantle caused by slab breakoff, though other magmas were generated at depths as shallow as those of MORB either through back-arc spreading or ridge subduction. This might have an implication on the Cambrian-Ordovician ophiolite pulse.

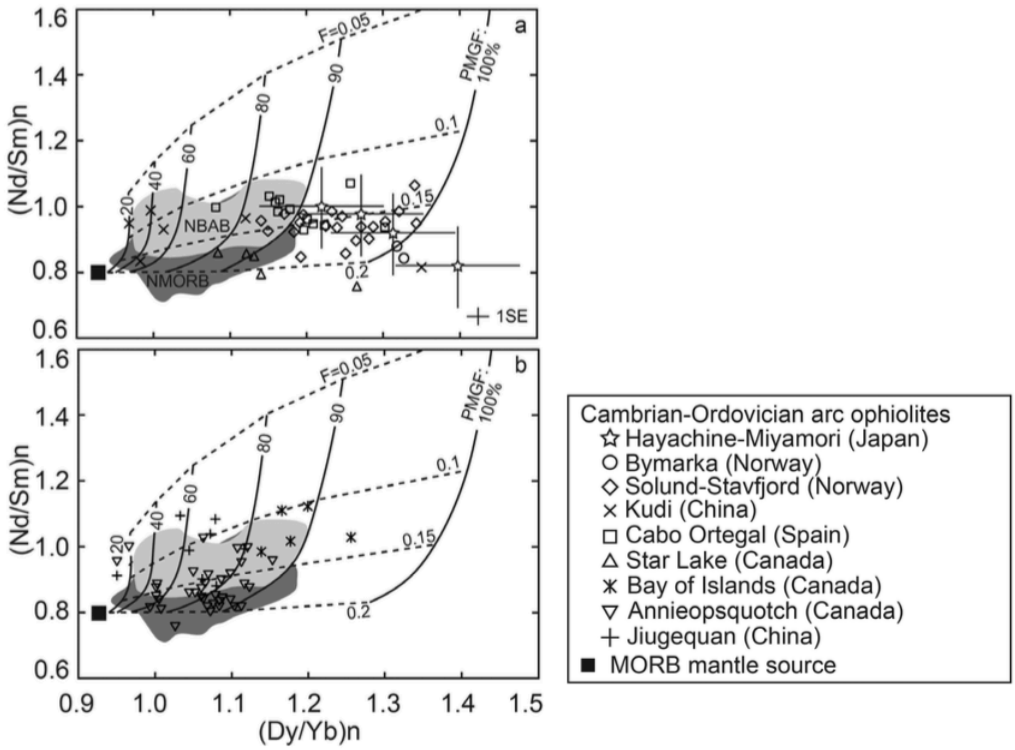

Fig.2-26: Relationship between chondrite normalized ratio of Nd and Sm ((Nd/Sm)n) and that of Dy/Yb ((Dy/Yb)n) for the ultramafic dikes (see Table 2-8) of the Hayachine-Miyamori ophiolite as stars with errors and the other Cambrian-Ordovician subduction-related ophiolites, which are (a) Bymarka (Slagstad, 2003); Solund-Stavfijord (Furnes et al., 2012); Kudi (Fang, 1998; Wang et al., 2002); Cabo Oltegal Complex (Sánchez-Martínez et al., 2007); Star Lake (Lissenberg et al., 2005), and (b) Bay of Islands (Kurth et al., 2005); Jiugequan (Xia and Song, 2010); Annieopsquotch (Lissenberg et al., 2005). Also shown are trends of accumulated partial melts produced by fractional melting of the MORB mantle source (Workman and Hart, 2005). The melting model assumed steady-state decompressional melting with continuous melt separation starting from various depths of the garnet stability field (Ozawa, 2001). The adopted melt separation rates (γ) are 0.99, 0.96, 1.00, and 1.00 for the reaction extents (t) of 0.001, 0.02, 0.15 and 0.2, respectively. Solid curves represent the weight percentage of the degree of melting in the garnet stability field in the total melting (PMGF), and the dashed curves represent the degree of total melting in weight fraction (F). Compiled literature data of the normal mid-ocean ridge basalts (NMORB) (Arevalo Jr. and McDonough, 2008; Arevalo Jr. et al., 2009; Davis et al., 2008; Hall et al., 2006; Mahoney et al., 2002; Nauret et al., 2006; Sims et al., 2002; Sun et al., 2003; Sun et al., 2008) and those of normal back-arc basin basalts (NBABB) (Arevalo Jr. and McDonough, 2008; Pearce et al., 2005; Pearce et al., 1994) are also shown for comparison. The CI-chondrite composition is after McDonough and Sun (1995).

An appropriate geodynamic model for the ophiolite pulse must explain the following geological and petrological features in the Cambrian-Ordovician time. First, the MPT of the Cambrian-Ordovician upper mantle is similar to that of the present-day upper mantle. Second, LIPs and plume-related ophiolites are scarce in contrast with the Jurassic-Cretaceous ophiolite pulse (Ernst and Buchan, 2003; Dilek and Furnes, 2011; Furnes et al., 2014). Third, U-Pb zircon ages that represent ages of acidic magmatic activity have a peak at 490 – 530 Ma (Hawkesworth et al., 2009). The first feature suggests that the thermal effect on the surface tectonics was the same as those of the present-day plate tectonics. The second feature cannot be explained by the superplume models (Ishiwatari, 1994; Dilek, 2003; Vaughan and Scarrow, 2003). The third feature suggests that the Cambrian-Ordovician ophiolite pulse corresponds to the period of the assembly of the Gondwana supercontinent (Hawkesworth et al., 2009; Campbell and Allen, 2008).

A subduction termination is accompanied by a slab breakoff and ophiolite exhumation and is highly expected during arc-continent collision which induces passive upwelling of the sub-slab mantle from over 100 km depth (Davies and von Blanckenburg, 1995; Gerya et al., 2004). We propose a new model for the origin of the Cambrian-Ordovician ophiolite pulse: the frequent occurrence of subduction termination followed by slab breakoff was the principal cause of the ophiolite pulse, which led to the formation of the Gondwana supercontinent (slab breakoff model). The slab breakoff induced the decompressional melting of the sub-slab mantle and subsequent obduction of the ophiolites. The mantle potential temperatures of Cambrian-Ordovician ophiolites are similar to the present-day value, but magmas were generated under a similar degree of melting by passive upwelling at various depths from similar to the present-day

mid-ocean ridge and back-arc basin environments to the depth ~170 km. This implies that the water content of the shallow Cambrian-Ordovician upper mantle was similar to the present-day value, but that the water content at depth ~170 km or deeper beneath the subducting slab was as high as 0.04 – 0.18 wt%.

The "slab breakoff model" could be applied to the other ophiolite pulses if deep melting signatures, such as high PMGF, and potential temperature comparable to the spreading ridge environment, are shown from basaltic rocks proposed to have been derived from back-arc spreading. The thermal state of the upper mantle during the Jurassic-Cretaceous pulse has been estimated to be 0 – 60 °C hotter than the present-day values (e.g., Machetel and Humler, 2003; Van Avendonk et al., 2016). Even if this is the case, the depth of decompressional melting beneath spreading ridge during the pulse is deeper only by < ~20 km than the present-day depth of melting beneath the mid-ocean ridge and back-arc basin (e.g., Katz et al., 2003; Herzberg et al., 2010). Because of this, the slab breakoff signatures characterized by deep melting at > 100 km depth can be used to identify tectonics responsible for decompressional melting during the Jurassic-Cretaceous ophiolite pulse on the basis of the REE proxies.

Komatiites reported from a Triassic-Jurassic back-arc related ophiolite, Othris ophiolite, Greece (e.g., Tsikouras et al., 2008; Baziotis et al., 2017), a Cretaceous komatiitic ophiolite, Gorgona Island, Colombia (e.g., Aitken and Echeverria, 1984), and picritic basalt from the Jurassic Sorachi-Ezo Belt, Hokkaido (e.g., Maekawa, 1983; Niida et al., 1999; Ichiyama et al., 2012) are plausible candidates for magmas formed by slab breakoff tectonics. These high Mg magmas are thought to have been derived from melting of high temperature deep mantle. The high MgO content and depleted HREEs are attributed to a high temperature and deep melting without careful examination of contribution of water. A significant involvement of water in the

melting environment is suggested for the Othris ophiolite by the presence of pargasite in groundmass of the komatiites (Tsikouras et al., 2008), and thus it is highly plausible that slab breakoff tectonics was involved at least in the formation of the Othris ophiolite.

Our model may provide one of the alternative mechanisms for the "ridge subduction model" by Shervais (2001) explaining the termination of subduction and MORB and BABB-like magmatism, and the "depleted plume model" by Anderson (1994) explaining the plume-like deep melting of depleted mantle source.

3. Mantle dynamics of slab breakoff

3.1 Introduction

Slab breakoff model is widely applied to evolution models of world orogenic belts and subduction zones (e.g., Alps, Anatolia-Zagros, Mediterranean, Himalaya, and Tibet; Niu et al., 2017). However, most of the slab breakoff models are not appropriately constrained by geological and geophysical solid evidences, as mentioned in the general introduction (**Chapter 1**).

A slab rapture and sinking are inevitable processes as a terminal event of an steady-state subduction through continent–continent or continent–arc collision (e.g., Shervais, 2001). It has been known that the present-day slab raptures are linked with the magmatism characterized by decompressional melting at various depths (~50 − 170 km; see section **2.9.1.2**, Table 2-15) induced by upwelling of the deep sub-slab asthenosphere. Numerical models of the slab breakoff also suggest that the slab breakoff triggers upwelling and melting of the sub-slab and wedge asthenosphere from various depths, over 100 km depth range as a counter flow of the slab detachment and sinking (Gerya et al, 2004; Menant et al., 2016; Freeburn et al., 2017). The absolute depths of upwelling depend on the depth of rupture ranging from 80 – 240 km in these modeling and are similar to or deeper than the rupture depth. The depths of magma generation related to slab breakoff are distinctively deeper than those expected in decompressional melting along divergent plate boundaries, such as beneath mid-ocean ridges and back-arc basins (30 - 100 km; e.g., Kinzler and Grove, 1992; Yamashita and Tatsumi, 1994; Wiens et al., 2006). It is highly expected that a slab-breakoff causes not only a sudden change of magma generation depths shallower than ~80 km by melting of the wedge mantle above subducting slab (Tatsumi and

Eggins, 1995; Grove et al., 2012) to depths greater than ~100 km but also a sudden suppression of contribution of slab-derived fluids in magma generation. Therefore, a sudden increase in magma generation depth and change of geochemical features of magmas from those involving slab-derived fluids to those characterized by the MORB mantle source may provide lines of solid evidence for the slab breakoff. It must be, however, noted that such deep magma generation by decompressional melting requires higher potential temperature and/or higher water contents of the source mantle.

From these points of view, the decompressional melting of depleted mantle at ~170 km after the extensive flux melting documented for the Cambrian-Ordovician northeast Japan in **Chapter 2** (Kimura et al., 2020) provides the solid evidence for the slab breakoff tectonics. On the basis of the results of **Chapter 2**, we may further examine evolutional dynamics of the slab breakoff process if information before the formation of ultramafic dikes with high time resolution is available from the ophiolite. We use temporal change of melting conditions (melting depth, degree of melting, and melting mechanism) recorded in the Cumulate Member of the Hayachine-Miyamori ophiolite after establishing stratigraphy of the cumulate.

3.2 Geology and lithology of the Cumulate Member of the Hayachine-Miyamori ophiolite

The Hayachine-Miyamori ophiolite (Fig. 3-1a) has two main lithologic members: Tectonite Member and Cumulate Member. The latter is distributed to the west of the former with the boundary striking NW-SE (see, Fig. 2-1b). Our recent field study in the Cumulate Member (Fig. 3-1b) clarified a large-scale lithologic variations characterized by alternation of dunite-dominant and wehrlite-dominant zones as shown in geological map (Fig. 3-1c). Each zone

consists of layers of dunite, wehrlite, and clinopyroxenite with various thickness from several meters to a few hundred meters striking N ~48 °W and dipping ~80 °S. This indicates that the three zones correspond to three layers, the total thickness of which attains ~3.0 km. The layered structure is almost concordant with the Cumulate Member-Tectonite Member boundary and the elongate tectonite blocks exclusively occurring along the boundary (Fig. 3-1c; Ozawa, 1984). These field relationships indicate that the boundary corresponds to the bottom of the cumulate pile younging westwards. We divided the Cumulate Member into three stratigraphic zones according to the volume ratio of dunite and wehrlite. They are dunite-dominant upper and lower zones and wehrlite-dominant middle zone (Fig. 3-1c). The thickness of the lower zone is ~1170 m, and that of the middle layer is ~1080 m, and that of the upper layer is ~720 m. The boundary of the lower and middle zones is located at ~1170 m and that of the middle and upper zones at 2250 m in the stratigraphic height from the bottom. We collected samples from each zone covering the entire member from 120 to 2630 m in the stratigraphic height (Fig. 3-1b).

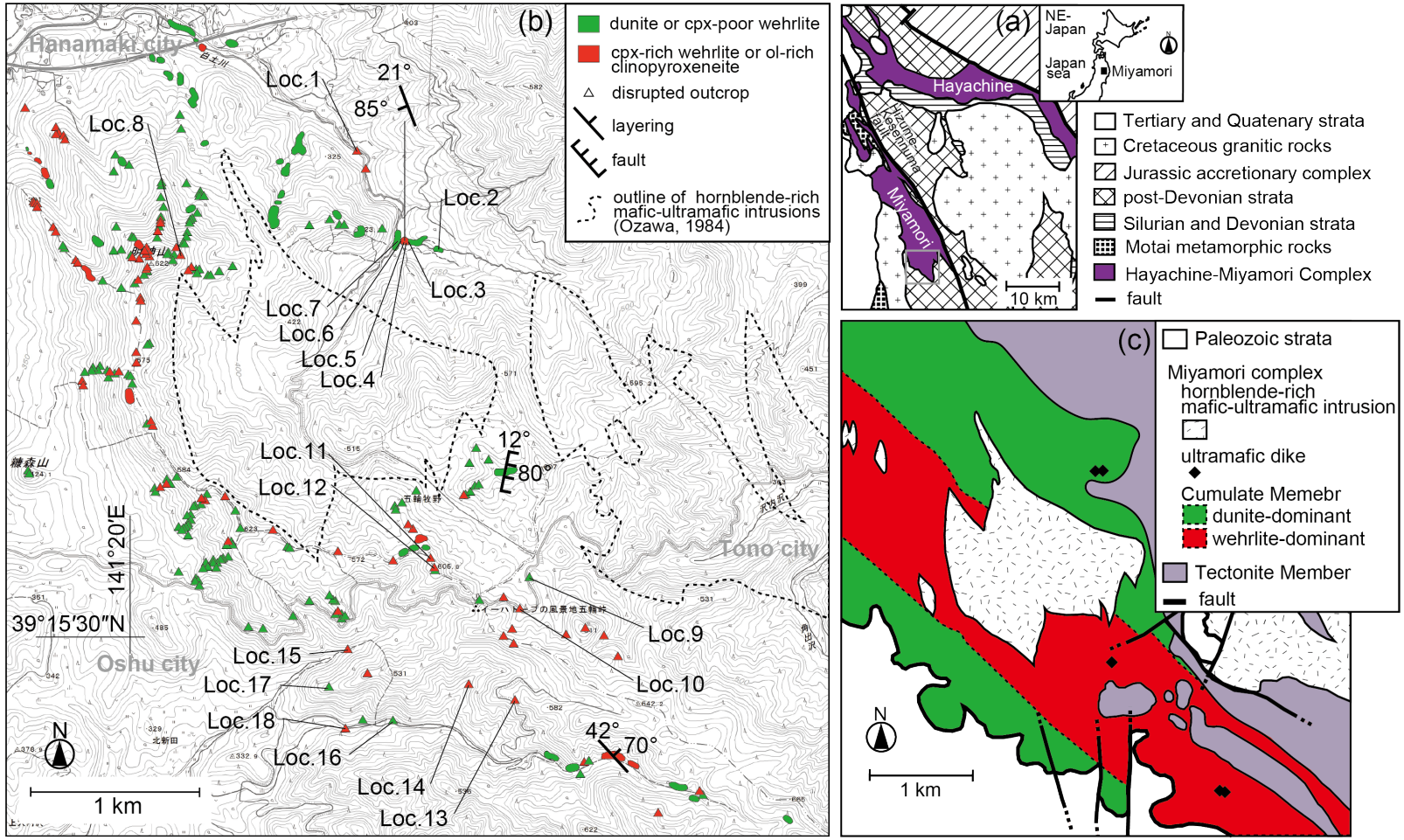
(b)
dunite or cpx-poor wehrlite
cpx-rich wehrlite or ol-rich clinopyroxeneite
disrupted outcrop
layering
fault
outline of hornblende-rich mafic-ultramafic intrusions (Ozawa, 1984)
Hanamaki city
Tono city
Oshu city
Loc.1
Loc.2
Loc.3
Loc.4
Loc.5
Loc.6
Loc.7
Loc.8
Loc.9
Loc.10
Loc.11
Loc.12
Loc.13
Loc.14
Loc.15
Loc.16
Loc.17
Loc.18
21°
85°
12°
80°
42°
70°
141°20′E
39°15′30″N
N
1 km
(a)
NE-Japan
Japan sea
Miyamori
Hayachine
Hayachine-Miyamori Complex
10 km
Tertiary and Quatenary strata
Cretaceous granitic rocks
Jurassic accretionary complex
post-Devonian strata
Silurian and Devonian strata
Motai metamorphic rocks
Hayachine-Miyamori Complex
fault
(c)
Paleozoic strata
Miyamori complex
hornblende-rich mafic-ultramafic intrusion
ultramafic dike
Cumulate Memebr
dunite-dominant
wehrlite-dominant
Tectonite Member
fault
N
1 km

Fig. 3-1: (a): Simplified geological map of the northwestern part of the southern Kitakami Mountains showing distribution of the Miyamori and Hayachine ultramafic-mafic complexes consisting of the Hayachine−Miyamori ophiolite, Ordovician-Devonian strata, and Silurian-Devonian granitic rocks (after Ehiro and Suzuki, 2003; Kawamura at al., 2013; Ozawa, 1984; Maekawa, 1981). Gray rectangle in (a) indicates the area shown in (b). (b): Route map of the Cumulate Member in the Miyamori ultramafic-mafic complex. Localities of examined samples are shown by numbers in (b). (c): Geological map of the southern part of the Miyamori ultramafic-mafic complex exhibiting layered-structure in the Cumulate Member. The outline of the hornblende-rich mafic-ultramafic intrusions and the Tectonite Member and faults are after Ozawa (1984).

The samples show mesocumulate texture with 23.0 – 89.6 vol% of cumulus phases (Table A6), which consist of euhedral – subhedral olivine including euhedral – subhedral chrome spinel and euhedral – subhedral clinopyroxene (Fig. 3-2) locally showing poikilitic texture (Ozawa, 1983). The grain size of the cumulus phase ranges from a few millimeter to 10 mm. The matrix filling interstitial part consists mainly of anhedral olivine, clinopyroxene, orthopyroxene, and amphibole with or without plagioclase, minor even if it is present (Fig. 3-2; Ozawa, 1983, 1986).

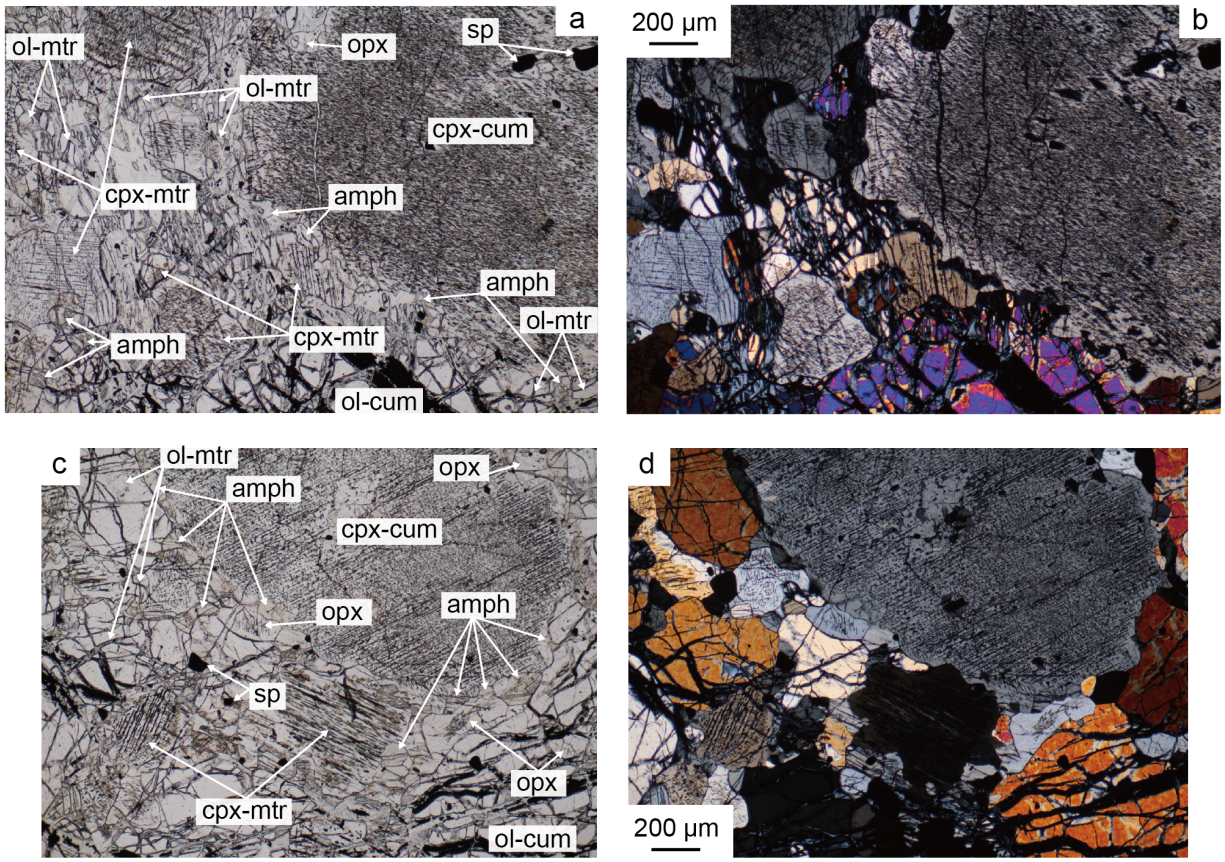

Fig. 3-2: Photomicrographs of the wehrlite in the Cumulate Member: (a), (c) under open nicol and (b), (d) crossed nicols. Euhedral-subhedral cumulus clinopyroxene (cpx-cum) including many spinel exsolution lamellae and cumulus olivine (ol-cum) have interstices filled with finer-grained equigranular minerals (clinopyroxene (cpx-mtr), olivine (ol-mtr), orthopyroxene (opx), and amphibole (amph)), which are a few hundred micron meters across. Euhedral-subhedral chromian spinel (sp) grains are included in olivine or clinopyroxene. The orthopyroxene and amphibole are partially altered in (a) and (b), but they are mostly fresh in (c) and (d).

3.3 Mineral composition

3.3.1 Major and trace element compositions of constituent minerals

Major and trace elements concentrations of cumulus olivine, clinopyroxene, and spinel were measured with EPMA, and rare earth element (REE) concentrations of clinopyroxene were measured with LA-ICP-MS both at the University of Tokyo. The analytical procedures are described in **Chapter 2** (**2.5 Analytical Methods**).

The ranges of Mg# of cumulus olivine and clinopyroxene grains, and TiO_2 wt% of cumulus clinopyroxene grains are 0.85 – 0.87, 0.87 – 0.93, 0.27 – 0.67, respectively. The $Fe^{+3}/(Cr + Al + Fe^{+3})$ of spinel ranges mostly from 0.07 to 0.20 (Fig. 3-3) with exceptions of higher values ranging 0.30 – 0.37 for a few small and anhedral grains. The latter type coexists with the dominant type in the same sample. The $Fe^{+3}/(Cr+Al+Fe^{+3})$ of the dominant type is correlated with the Cr# resulting in a trend oblique to the Cr-Al edge in the Al-Cr-Fe^{3+} ternary diagram (Fig. 3-3). The Cr# of the dominant spinel is negatively correlated with the TiO_2 wt% of clinopyroxene (Fig. 3-4). Sample means of the spinel Cr#, olivine Mg# and NiO wt%, and clinopyroxene Mg# and TiO_2 wt% are listed in Table 3-1. Representative major and trace element analyses of clinopyroxene grains are listed in Table A6.

Table 3-1. Stratigraphic variations of measured and corrected mean mineral compositions (Cr# of spinel, NiO wt% and Mg# of olivine, TiO_2 wt % and Mg# of clinopyroxene; corrected Mg# of clinopyroxene and olivine, NiO wt% of olivine) in sample from the Cumulate Member.

Locality	Sample	Horizon & Stratigraphy (m)		Mineral compositions							
				Spinel	Olivine				Clinopyroxene		
					NiO (wt%)		Mg #		TiO_2 (wt%)	Mg #	
				Cr #	raw	corrected	raw	corrected		raw	corrected
18	78082004		2630	0.35	0.20	0.18	0.85	0.88	0.38	0.89	0.85
17	78082609	upper	2510	0.53	0.23	0.22	0.86	0.88	0.33	0.91	0.86
16	78082007b		2410	0.53	-	-	-	-	0.40	0.91	0.86
15	78081907b		2250	0.56	0.22	0.21	0.86	0.88	0.26	0.92	0.86
14	79061403		1950	0.27	-	-	-	-	0.53	0.88	0.84
13	78081916		1830	-	-	-	-	-	0.30	0.90	0.87
12	77112433		1558	0.30	-	-	-	-	0.58	0.89	0.85
11	77112434	moddle	1530	0.33	-	-	-	-	0.44	0.90	0.86
10	77112427		1410	0.33	0.25	0.24	0.85	0.87	0.33	0.91	0.84
9	77112426		1240	0.55	0.24	0.23	0.85	0.86	0.36	0.91	0.84
8	17101409		1170	-	0.20	0.18	0.84	0.86	0.48	0.89	0.83
7	15080403c6		270	0.26	0.23	0.22	0.86	0.87	0.56	0.90	0.84
6	15080403c2		250	0.67	0.18	0.17	0.85	0.88	0.35	0.90	0.85
5	15080403c1		250	0.34	0.19	0.18	0.85	0.87	0.53	0.90	0.84
4	15081913c	lower	240	0.31	0.20	0.19	0.85	0.86	0.48	0.90	0.84
3	15081913j3		230	0.41	0.22	0.22	0.87	0.87	0.57	0.92	0.85
2	15081610c		120	0.39	0.21	0.19	0.85	0.87	0.59	0.90	0.84
1	77112324		30	0.51	0.25	0.24	0.85	0.86	0.27	0.91	0.83

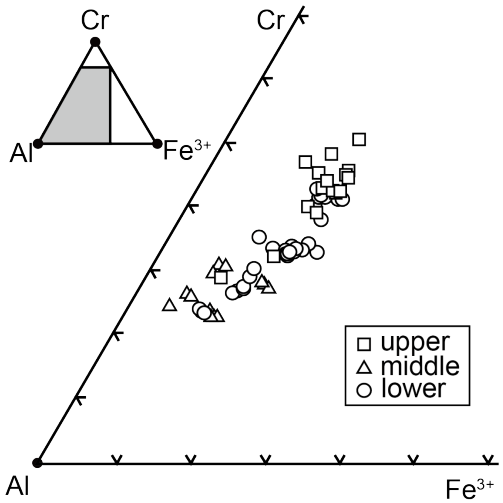

Fig. 3-3: Chemical compositions of relatively ferric-poor spinel grains in samples from the Cumulate Member plotted in the triangular diagram of Cr, Al, and Fe^{3+}. Spinel grains with $Fe^{+3}/(Cr + Al + Fe^{+3}) > 0.3$ are not shown. We analyzed 2 – 10 grains for each sample. Squares, triangles, and circles indicate spinel grains in the upper, middle, and lower zones of the Cumulate Member, respectively.

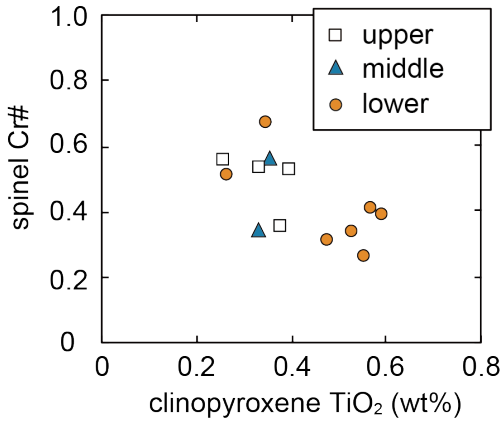

Fig. 3-4: Relationship between sample-mean values of Cr# of spinel and TiO_2 (wt%) of cumulus clinopyroxene in the Cumulate Member. Squares, triangles, and circles indicate data for samples from the upper, middle, and lower zones of the Cumulate Member, respectively.

Spatial variations of Mg#, NiO wt% of olivine and Cr# of spinel in layered wehrlite and dunite crossing their boundary over ~15 cm were examined to confirm the stratigraphic relationship inferred from the distribution of the tectonite blocks occurring near the boundary of the two members. The dunite contains clinopyroxene < 1 vol%, and the wehrlite consists of olivine (45 vol%) and clinopyroxene (43 vol%). The Mg#, NiO wt% of olivine and Cr# of spinel increase from 0.85 to 0.88, from 0.21 to 0.25, and from 0.40 to 0.52, respectively from the SW to NE (Fig. 3-5).

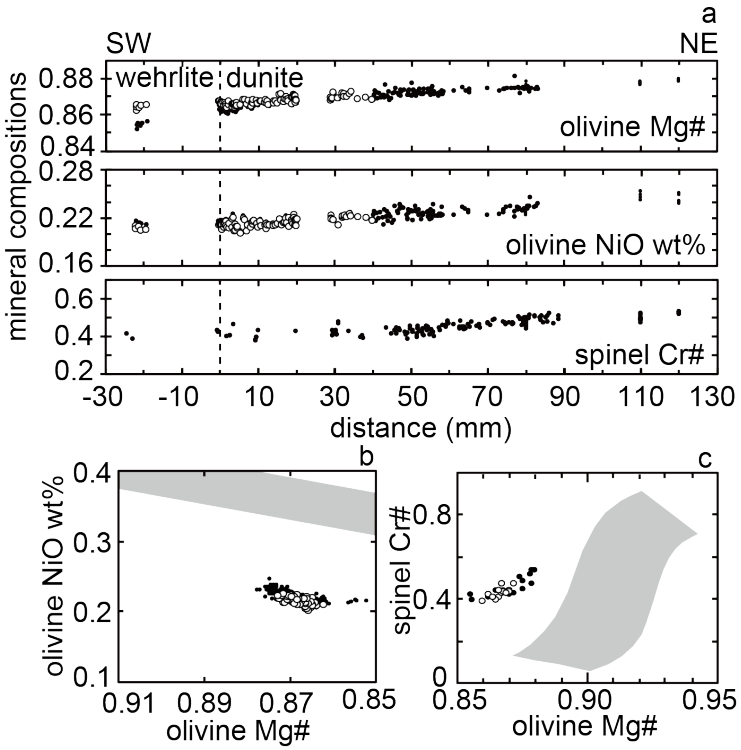

Fig. 3-5: (a) Spatial variations of Mg# and NiO wt% of olivine and Cr# of spinel crossing a contact between a wehrlite and a dunite at the Loc.#5 in Fig. 3-1b. The distance is measured from the boundary taken positive towards to the dunite. Dots are raw compositions, and open circles are magmatic composition at 1200 ℃, which were calculated by using partition coefficients and modal abundances of olivine and clinopyroxene (Kawasaki and Ito, 1994; Witt-Eickschen and O'Neill, 2005; Table A6). The correction for the dunite margin within 40 mm distance from the boundary was made by considering the effect of Fe-Mg diffusion from the wehrlite side. We modeled the subsolidus modification by assuming that the clinopyroxene mode decrease from the boundary to 40 mm inside the dunite, where the mode of clinopyroxene is as small as 0.3 %, in a pattern similar to that observed at the contact of the ultramafic dike and the host (Fig. 2-8). (b) The NiO wt% of olivine plotted against olivine Mg# and (c) the Cr# of spinel plotted against Mg# of olivine for the data shown in (a). The shaded regions in (b) and (c) are the mantle olivine arrays after Takahashi et al. (1987) and the olivine-spinel mantle array after Arai (1987), respectively.

Mean values of REE concentrations and chondrite-normalized ratios of Ce and Sm ((Ce/Sm)n), Sm and Gd ((Sm/Gd)n), and Dy and Yb ((Dy/Yb)n) of clinopyroxene for each sample are listed in Table 3-2. The mean values of (Ce/Sm)n, (Sm/Gd)n, and (Dy/Yb)n range 0.52 – 0.63, 1.03 – 1.05, and 1.43 – 1.57, respectively, in the upper zone. The values range 0.39 – 0.90, 0.92 – 1.08, and 1.29 – 1.49, respectively, in the middle zone, and 0.54 – 0.99, 0.91 – 1.27, and 1.36 – 1.77, respectively, in the lower zone.

Table 3-2. Measured sample means of REE concentrations and chondrite-normalized ratios ((Dy/Yb)n, (Sm/Gd)n, and (Ce/Sm)n) of clinopyroxene in the Cumulate Member.

Locality #	1	2	3	4	5	6	7	8	9
Sample	77112324	15081610c	15081913j3	15081913c	15080403c1	15080403c2	15080403c6	17101409	77112426
(ppm)									
La	2.52	0.67	0.64	1.62	1.28	0.69	0.83	0.92	0.82
Ce	4.77	2.33	1.75	3.83	3.71	1.97	2.60	3.42	2.35
Pr	0.70	0.51	0.33	0.63	0.71	0.39	0.52	0.82	0.42
Nd	3.78	3.21	1.93	3.49	4.42	2.28	3.22	5.46	2.18
Sm	1.21	1.09	0.65	1.21	1.58	0.76	1.18	2.20	0.65
Eu	0.40	0.39	0.23	0.41	0.57	0.28	0.38	0.73	0.25
Gd	1.29	1.59	0.95	1.53	1.97	0.91	1.44	2.93	0.87
Tb	0.19	0.28	0.16	0.23	0.30	0.15	0.24	0.49	0.14
Dy	1.17	1.66	1.09	1.61	2.01	1.04	1.49	3.29	0.95
Ho	0.22	0.32	0.22	0.30	0.37	0.18	0.29	0.65	0.17
Er	0.57	0.83	0.56	0.81	1.04	0.48	0.78	1.75	0.50
Tm	0.08	0.13	0.09	0.11	0.15	0.07	0.10	0.23	0.07
Yb	0.49	0.74	0.54	0.72	0.87	0.39	0.70	1.52	0.49
Lu	0.07	0.11	0.08	0.09	0.13	0.05	0.09	0.20	0.06
(Ce/Sm)n	0.99	0.54	0.68	0.79	0.59	0.65	0.55	0.39	0.90
(Sm/Gd)n	1.27	0.92	0.91	1.06	1.08	1.13	1.10	1.01	1.01
(Dy/Yb)n	1.58	1.49	1.36	1.50	1.54	1.77	1.43	1.45	1.29

Table 3-2. (continue)

10	11	12	13	14	15	16	17	18
77112427	77112434	77112433	78081916	79061403	78081907b	78082007b	78082609	78082004
1.30	0.53	0.74	0.43	0.94	0.55	0.63	0.90	0.55
3.52	1.84	2.64	1.49	3.85	1.74	1.83	3.29	2.18
0.65	0.40	0.53	0.32	0.91	0.32	0.39	0.66	0.47
3.97	2.46	3.21	2.09	5.98	1.94	2.34	3.84	2.85
1.41	0.88	1.19	0.89	2.27	0.69	0.88	1.34	1.03
0.48	0.31	0.43	0.33	0.76	0.26	0.32	0.47	0.37
2.04	1.13	1.49	1.30	2.84	0.90	1.13	1.74	1.32
0.38	0.19	0.26	0.22	0.46	0.15	0.19	0.27	0.23
2.75	1.28	1.83	1.43	3.06	0.97	1.31	1.80	1.51
0.55	0.24	0.35	0.30	0.59	0.18	0.25	0.36	0.30
1.52	0.66	0.96	0.78	1.61	0.47	0.66	0.94	0.81
0.22	0.09	0.13	0.10	0.22	0.06	0.09	0.12	0.11
1.41	0.63	0.85	0.64	1.45	0.42	0.57	0.84	0.68
0.19	0.09	0.12	0.09	0.19	0.06	0.08	0.11	0.09
0.62	0.52	0.55	0.42	0.42	0.63	0.52	0.61	0.53
0.93	1.05	1.07	0.92	1.08	1.04	1.05	1.03	1.05
1.31	1.35	1.45	1.49	1.42	1.57	1.55	1.43	1.48

3.3.2 Restoration of the original mineral compositions at a magmatic temperature

The calculated exchange partition coefficients of Fe^{2+} and Mg^{2+} between olivine and clinopyroxene ($X^{Ol}_{Mg} \cdot X^{CPX}_{Fe} / X^{Ol}_{Fe} \cdot X^{CPX}_{Mg}$, X is mole fraction) from the mean values of EPMA analyses for each sample yield ~0.61. This value suggests that there was Fe-Mg exchange between olivine and clinopyroxene up to temperatures lower than 800 °C (Kawasaki and Ito, 1994). We need magmatic compositions of olivine in order to evaluate extent of fractional crystallization before the solidification of the cumulate rocks. We thus estimated the Mg# and NiO wt% of olivine and Mg# of clinopyroxene at 1200 °C from the measured chemical compositions and modal abundances of these minerals (Table A6) by using temperature-dependent partition coefficients calibrated by Kawasaki and Ito (1994) and Witt-Eickschen and O'Neill (2005). The corrected values are listed in Table 3-1. The subsolidus modification of the Cr# of spinel, expected by partitioning of Cr and Al with clinopyroxene, orthopyroxene, and amphibole, is negligible though Cr and Al abundances in pyroxenes are strongly dependent on

temperature (Ozawa, 1983). The subsolidus modification of the TiO_2 in clinopyroxene by its subsolidus partitioning with spinel, orthopyroxene, and amphibole is also negligible because of the higher abundance of clinopyroxene relative to other Ti-bearing phases, such as spinel and amphibole in most of the samples (Table A6). The estimated magmatic values of Mg# and NiO wt% of olivine crossing the dunite-wehrlite boundary over ~15 cm range 0.86 – 0.88 and 0.20 – 0.25 wt%, respectively (Fig. 3-5). The magmatic olivine compositions and Cr# of spinel show systematic decreases from the dunite to the wehrlite, which implies the extent of fractional crystallization increases from east to west (Fig. 3-5).

Figure 3-6 shows the relationship between the estimated magmatic Mg# of olivine and Cr# of spinel. The diagram shows that the data from the Cumulate Member are plotted in the area at the lower Mg# side of the olivine-spinel mantle array (Arai, 1987) with Cr# of spinel ranging from 0.2 to 0.7. Moreover, there is no systematic trend for each horizon except for a weak positive correlation of all data. Such variation patterns suggest extensive fractional crystallization from parental magmas formed by various degree of partial melting (Arai, 1987). This tendency is also supported by the observed correlation between olivine Mg# and spinel Cr# observed from the dunite-wehrlite boundary shown in Fig. 3.5c.

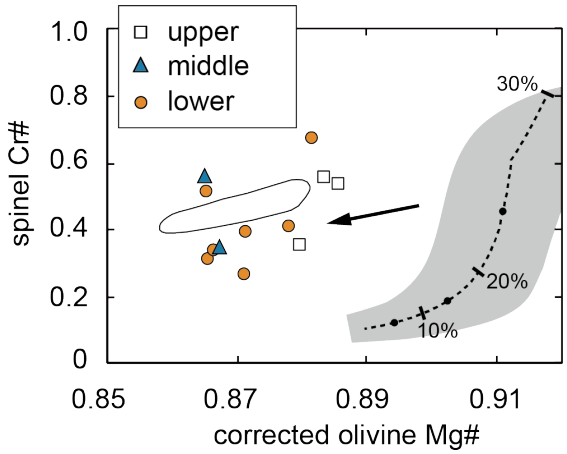

Fig. 3-6: Relationships between spinel Cr# and calculated magmatic olivine Mg# from the Cumulate Member. Symbols are the same as those in Fig 3-4. A shaded region and a dushed line show the olivine-spinel mantle array after Arai (1987) and a melting trend marked with degrees of melting in 10 % step, respectively (Ozawa 2001). A solid arrow shows a trend expected from the relationship observed in the dunite-wehrlite boundary shown as encircled area (Fig. 3-5c).

The REE concentrations of cumulus clinopyroxene are expected to be modified during crystallizations with interstitial melts in closed systems and subsolidus elemental exchanges among constituent minerals. We corrected them by using a batch crystallization model after evaluating the effect of observed matrix volume% for the interstitial modes (Table A6) using partition coefficients at the formation condition of a magma body crystallizing the Cumulate Member at ~0.6 GPa (Ozawa, 1986), ~1250 °C (Table 3-3). The cumulus clinopyroxene in the wehrlite samples is insensitive to the subsolidus modification because the REEs in the samples are mostly contained in clinopyroxene. In order to estimate the clinopyroxene compositions at the time of crystallization before adcumulus growth and matrix crystallization in a closed system, we used only samples containing > 60 % of cumulus phases (olivine and clinopyroxene) for the dunite and wehrlite and > 25 % of clinopyroxene in mineral modes for the wehrlite in order to

reduce uncertainty caused by corrections for the interstitial melt crystallization and subsolidus elemental exchange. The calculated values of (Ce/Sm)n, (Sm/Gd)n, and (Dy/Yb)n of the cumulus clinopyroxenes before adcumulus growth and matrix crystallization in a closed system are listed in Table 3-4. These REE ratios represent ratios of LREE/MREE, MREE/HREE, and HREE/HREE, respectively, which respectively have distinct sensitivities to degree of melting, melting extent in the garnet stability field, and extent of influx of an agent enriched in LREE during melting.

Table 3-3. Partition coefficients of REEs between melt and minerals used in the batch crystallization and partial melting models involved in the formation of the Cumulate Member.

Mineral	Olivine[1]		Spinel[2]	Orthopyroxene[3]		Clinopyroxene[4]		Garnet[1]	Amphibole[5]	Plagioclase[6]
Condition	crystallization	melting	crystallization & melting	crystallization	melting	crystallization	melting	melting	crystallization	crystallization
La	0.0000007	0.0000019	0.0006	0.0021	0.0010	0.050	0.055	0.0021	0.030	0.065
Ce	0.0000046	0.0000089	0.0006	0.0043	0.0019	0.08	0.088	0.0065	0.049	0.049
Pr	0.000020	0.000033	0.0006	0.0082	0.0036	0.13	0.13	0.018	0.075	0.049
Nd	0.000034	0.000050	0.0006	0.015	0.0065	0.19	0.19	0.048	0.11	0.040
Sm	0.00017	0.00020	0.0006	0.036	0.016	0.32	0.31	0.21	0.16	0.044
Eu	0.00033	0.00035	0.0006	0.050	0.022	0.38	0.36	0.37	0.18	0.87
Gd	0.00054	0.00054	0.0006	0.067	0.029	0.44	0.42	0.62	0.20	0.030
Tb	0.0012	0.0011	0.006	0.087	0.038	0.48	0.46	1.00	0.20	0.029
Dy	0.0020	0.0017	0.0015	0.11	0.049	0.52	0.50	1.54	0.20	0.017
Ho	0.0033	0.0026	0.0023	0.13	0.059	0.54	0.53	2.20	0.19	0.020
Er	0.0052	0.0038	0.0030	0.15	0.069	0.55	0.54	2.20	0.18	0.024
Tm	0.0077	0.0053	0.0038	0.17	0.078	0.54	0.55	3.80	0.17	0.049
Yb	0.012	0.0077	0.0045	0.18	0.087	0.53	0.55	4.65	0.15	0.030
Lu	0.015	0.0094	0.0053	0.20	0.094	0.52	0.55	5.47	0.14	0.024

[1] The data are after Sun & Liang (2013)
[2] The data are after Kelemen et al. (2003)
[3] The data are after Yao et al. (2012)
[4] The data are after Sun & Liang (2012)
[5] The data are after Shimizu et al.(2017)
[6] The data are after Aigner-Torres et al. (2007)

Table 3-4. Mean values of chondrite-normalized REE ratios ((Dy/Yb)n, (Sm/Gd)n, and (Ce/Sm)n) of clinopyroxene in equilibrium with parental magmas, and those of primary magmas for the samples containing > 60 % of cumulus phases for a dunite and wehrlites and > 25 % of clinopyroxene in mineral modes for wehrlites in the Cumulate Member. The data selection was made in order to reduce the effects of adcumulus and interstitial crystallization as well as subsolidus elemental exchange.

	Horizon & Sample	Clinopyroxene			Primary magma		
		(Ce/Sm)n	(Sm/Gd)n	(Dy/Yb)n	(Ce/Sm)n	(Sm/Gd)n	(Dy/Yb)n
upper	78082004	0.19	0.87	1.46	0.72	1.18	1.50
	78082609	0.19	0.82	1.39	0.73	1.11	1.43
	78082007b	0.16	0.84	1.50	0.63	1.14	1.54
	78081907b	0.19	0.82	1.51	0.74	1.11	1.55
moddle	79061403	0.12	0.86	1.40	0.48	1.17	1.44
	78081916	0.15	0.76	1.46	0.58	1.03	1.50
	77112434	0.18	0.86	1.32	0.69	1.16	1.36
	77112427	0.26	0.81	1.28	1.01	1.10	1.31
	77112426	0.29	0.81	1.24	1.10	1.09	1.28
lower	15080403c6	0.19	0.90	1.39	0.71	1.22	1.42
	15080403c1	0.18	0.91	1.56	0.71	1.23	1.60
	15081913c	0.27	0.86	1.45	1.03	1.17	1.49
	15081913j3	0.20	0.71	1.19	0.78	0.96	1.22
	15081610c	0.16	0.73	1.45	0.63	0.99	1.49

3.4 Magma generation condition and mechanism

3.4.1 Estimation of REE ratios of primary magmas

The values of (Ce/Sm)n, (Sm/Gd)n, and (Dy/Yb)n of parental magmas crystallizing cumulus clinopyroxene were calculated from the elemental ratios of the cumulus clinopyroxene before adcumulus growth and matrix crystallization, by using melt-clinopyroxene partition coefficients (Table 3-3), and are listed in Table 3-4 and Table A7.

The range of original olivine Mg#, 0.86 – 0.88, indicates that the parental magmas crystallized clinopyroxene and olivine forming the cumulate rocks are variously fractionated from primary magmas in equilibrium with mantle. We have evaluated the extent of fractional crystallization in section **2.8.5** for the ultramafic dikes by applying the olivine fractionation model. According to the results, the amount of fractionated olivine to reproduce the most fractionated parental magma having ~0.86 of olivine Mg# is 14.2 wt% (see, Table 2-8 and Fig. 2-18). The fractionation of olivine and clinopyroxene causes a shift in REE ratios ((Ce/Sm)n, (Sm/Gd)n, (Dy/Yb)n)) of estimated magma by smaller than 0.015, even if the amount of fractionated clinopyroxene attain 7.0 wt%, the value of which is a half of the fractionated olivine for the ultramafic dikes. Therefore, the fractional crystallization from the primary magma in equilibrium with the mantle does not affect the REE ratios at all. We can treat the estimated ratios of the fractionated parental magmas listed in Tables 3-4 and A7 as those of the primary magmas segregated from the mantle.

3.4.2 Estimation of temporal changes of melting conditions

The (Sm/Gd)n, (Dy/Yb)n, and (Ce/Sm)n of primary magmas estimated above are sensitive for the contribution of degree of total melting (F), percentage of melting in the garnet-stability field (~75 km; Gasparik, 2003) in total melting (PMGF, see also **Chapter 2**), and a rate of material influx into the melting system relative to the melting (β), respectively. We have developed these REE ratios as proxies for the β, F, PMGF, degree of melting in the garnet-stability field in total melting (FG), and that of spinel-stability field (FS) applicable to cumulate rocks by using open system fractional melting model (Ozawa, 2001) with an influx agent as

Agent 3 of Yoshikawa and Ozawa (2007) and partition coefficients listed in Table 3-3. The adopted melt separation rate (γ) is 1.00, which corresponds to near fractional melting.

Table 3-5. Generation conditions of primary magmas for the Cumulate Member (degree of total melting (F), degree of melting in garnet-stability field (FG), degree of melting in spinel-stability field (FS), percentage of melting in garnet-stability field in the total melting (PMGF), and influx rate in weight fraction (β)) and solidus conditions (pressure and depth) for the samples which have < 40 vol% matrix. The adopted melt separation rate (γ) is 1.00.

	Sample & Horizon	Segregation conditions					Solidus conditions	
		Degrees of melting (wt%)			PMGF (%)	β	Pressure (GPa)	Depth (km)
		F	FG	FS				
upper	78082004	6.5	5.3	1.2	82	0.02	4.9	160
	78082609	9.0	7.1	1.9	79	0.10	5.7	180
	78082007b	8.0	6.8	1.2	85	0.01	5.5	170
	78081907b	9.6	8.4	1.2	87	0.11	6.2	190
moddle	79061403	6.5	5.0	1.5	77	0.00	4.8	150
	78081916	12.1	10.8	1.3	89	0.03	7.2	220
	77112434	5.8	3.9	1.9	67	0.00	4.4	140
	77112427	10.5	7.7	2.8	74	0.31	-	-
	77112426	10.5	7.5	3.0	72	0.38	-	-
lower	15080403c6	5.5	4.1	1.4	74	0.00	4.4	140
	15080403c1	6.2	5.3	0.9	86	0.01	4.9	160
	15081913c	8.5	7.0	1.5	83	0.26	-	-
	15081913j3	15.5	12.1	3.4	78	0.19	-	-
	15081610c	14.3	13.1	1.2	92	0.08	8.1	250

Modeling results show that the overall variation of the F, FG, FS, PMGF, and β are 5.5 – 15.5, 3.9 – 13.1, 0.9 – 3.4, 72 – 92, and 0.00 – 0.38, respectively (Table 3-5). The values are weight fraction for β and wt% for other parameters. The stratigraphic variations are listed in Table 3-5, and are plotted in Fig. 3-7. In Fig. 3-7, the mean values of the F, FG, FS, PMGF, and β for the primary magmas of the ultramafic dikes estimated in **Chapter 2** are also plotted. For the ultramafic dikes, the mean melting pressures is estimated to be 5.3 ± 0.5 GPa (see, Table 2-11),

and the F, FG, FS, PMGF, and β to be 7.6 ± 1.8 wt%, 6.3 ± 1.5 wt%, 1.3 ± 0.4 wt%, 83 ± 2 %, and 0.09 ± 0.05 in weight fraction, respectively.

The stratigraphic variations of the PMGFs, Fs, and βs show large variations in the middle and lower zones but are consistent and close to those of the ultramafic dikes in the upper zone (Figs. 3-7a – 3-7c). This results in a tendency of convergence of the three parameters to the values of the ultramafic dikes. Because of the low F and β of the ultramafic dikes, they show overall decreases with stratigraphic horizon from the lower to the upper zones (Figs. 3-7b and 3-7c). Contrary to this the PMGF for the ultramafic dikes is situated in the middle of the wide range of variations for the lower zone of the cumulate (Fig. 3-7a). There is no overall correlation between F and β, but there is a weak positive correlation if points with high values of β are ignored (Fig. 3-7d). There is a weak positive overall correlation between F and PMGF, and the correlation is very tight if points with high values of β are ignored (Figs. 3-7e and 3-7f).

The β and F of the ultramafic dikes are 0.09 and 7.6 wt%, which corresponds to the variation of water contents in the source for the ultramafic dikes, 0.07 – 0.19 wt% (see, **Chapter 2** section **2.8.6**) and we know that the parent magmas of the dikes have been generated by decompressional melting. We thus infer that the formation mechanism of magmas with $\beta < 0.14$ (the upper bound of estimates for the ultramafic dikes including the error = 0.09 + 0.05) is dominated by decompressional melting with minor contribution of material influx, and those of $\beta > \sim 0.2$ is dominated by flux melting (Fig. 3-7d). When we adopt the upper limit of β for the decompressional melting, the Fs and FGs are positively correlated with the PMGFs (Figs. 3-7e – 3-7g). However, there is no such correlation with the FSs, which shows a limited variation ranging 1.0 – 2.0 wt% (Fig. 3-7h). These relationships imply that the decompressional melting for the Cumulate Member and ultramafic dikes took place mostly in the garnet-stability field.

If we assume that the melt segregation depths for the Cumulate Member and ultramafic dikes are the same, it is the variation in solidus pressure that produced the observed diversity of melting conditions. We estimated the solidus pressures for the Cumulate Member by evaluating the differences of the FG values from the mean for the ultramafic dikes (6.3 wt%), which corresponds to 5.3 GPa in the solidus pressure. The FGs range 3.9 – 13.1 wt% (Table 3-5 and Fig. 3-7g), and the differences range -2.4 – 6.8 wt%. We thus estimated the solidus pressures for the primary magmas of the Cumulate Member by using the linear relationship between dP/dF and pressure (0.41 GPa/wt% of degree of melting) constrained in the pressure range 2.6 – 3.5 GPa (Katz et al., 2003). We assumed that the linear relationship is valid even at higher pressures and obtained the solidus pressures ranging 4.4 – 8.1 GPa (Table 3-5). The stratigraphic variations of the melting pressures of primary magmas for the Cumulate Member and the mean pressure for the ultramafic dikes are shown in Fig. 3-8. In order to focus the relative pressure variation in the Cumulate Member, standard errors (1SEs) in Fig. 3-8a are based only on the FG errors for the Cumulate Member (Fig. 3-7g) calculated by propagating errors in the estimation of REE ratios of the primary magmas of the Cumulate Member (Table A7). The errors of the FG for the dikes (1.5 wt%) are propagated to the absolute pressure estimate for the Cumulate Member, resulting in the maximum errors of ± 1.5 GPa (Fig. 3-8b).

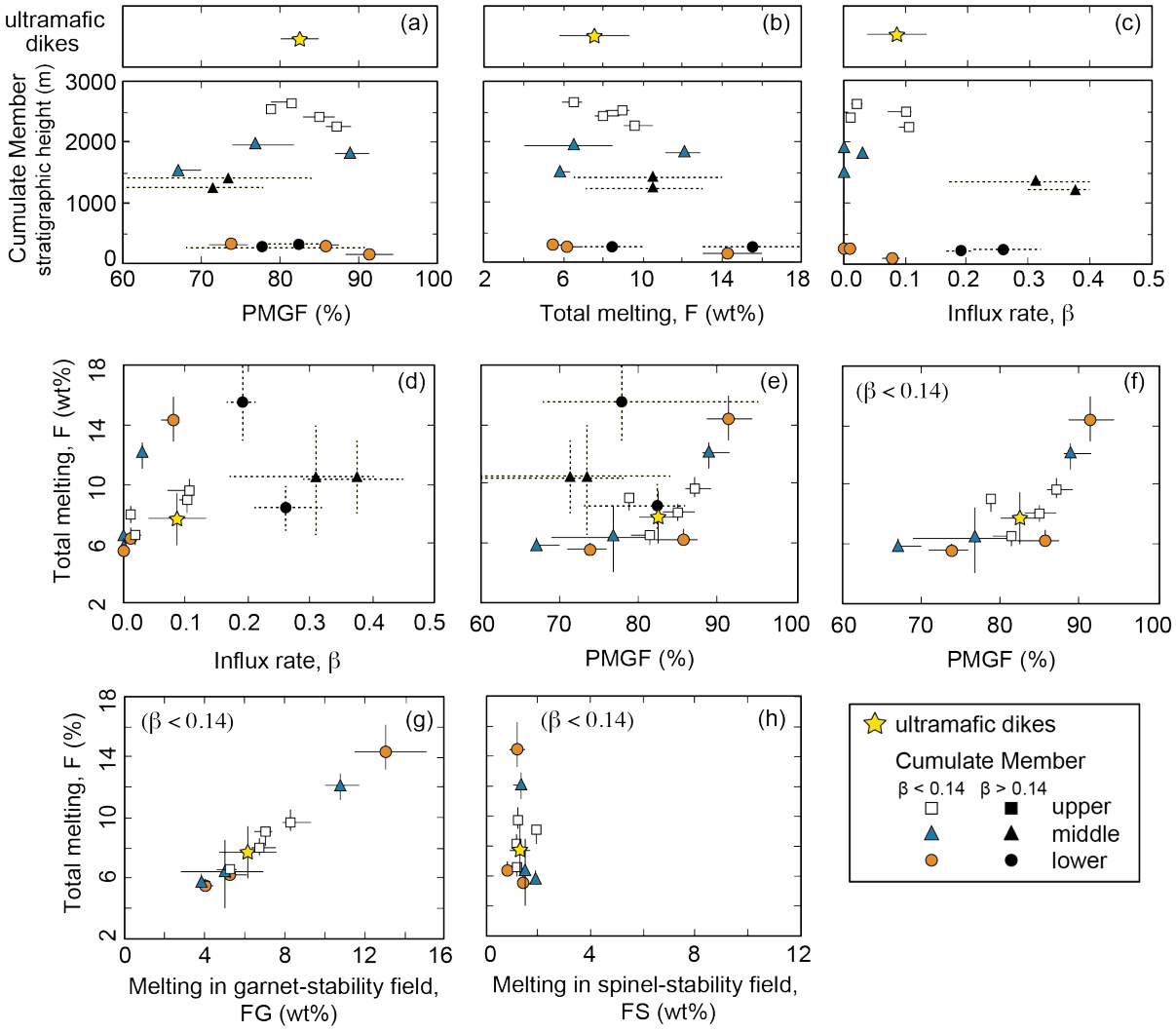

Fig. 3-7: Estimated melting conditions for the Cumulate Member and ultramafic dikes from the REE ratios. (a) Stratigraphic variations of the mean values of percentage of melting in the garnet-stability field in total melting (PMGF) for the three zones of the Cumulate Member and ultramafic dikes, (b) those of total melting (F), and (c) those of influx rate (β). (d) The mean values of F plotted against β, (e) PMGF, (f) PMGF for the samples with optimized values of $\beta < 0.14$, and (g) degree of melting in the garnet-stability field (FG) and (h) that of the spinel-stability field (FS) with $\beta < 0.14$. Squares, triangles, circles, and stars indicate the sample means from the upper, middle, and lower zones of the Cumulate Member, and the mean value of the ultramafic dikes, respectively. Solid black symbols indicate the samples having $\beta > 0.14$. Standard errors (1 SEs) for the samples of $\beta < 0.14$ and $\beta > 0.14$ are shown as solid and dotted bars, respectively.

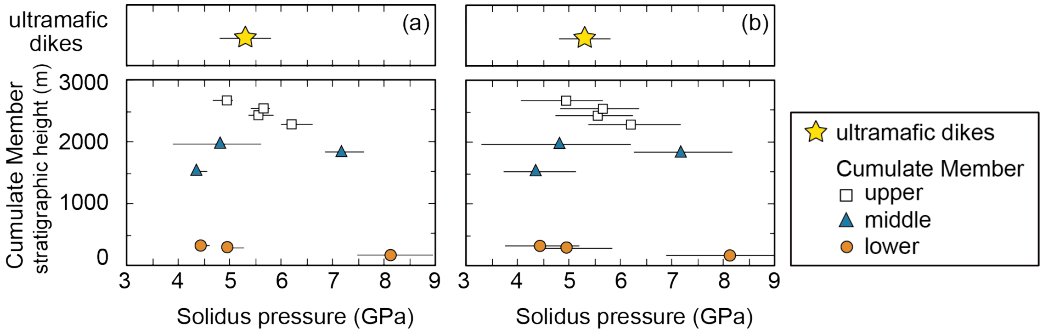

Fig. 3-8: Stratigraphic variations of solidus pressures for the primary magmas of the Cumulate Member estimated from their degrees of melting in the garnet-stability field (FG) constrained by REE element ratios, shown in the lower panels for (a) and (b), and the mean solidus pressure for the ultramafic dikes determined in Chapter 2 by using major elements (5.3 GPa, see Table 2-11), shown in the upper panels. (a) and (b) are different only in error estimation methods: (a) only REE errors are propagated in order to see relative differences in solidus pressures and (b) errors in pressure estimation of the ultramafic dikes are propagated to see absolute pressure estimates. The pressures for the Cumulate Member are calculated from differences between the FGs for each samples from the Cumulate Member (3.9 – 13.1 wt%, Fig. 3-7g) and the mean FG for the dikes (6.3 ± 1.5 wt%). Squares, triangles, circles, and stars indicate the sample means from the upper, middle, and lower zones of the Cumulate Member, and the mean value of the ultramafic dikes, respectively. Standard errors (1SEs) are shown as solid bars.

3.6 Discussion

3.6.1 Mantle dynamics of slab breakoff

The geodynamic modeling of slab breakoffs (e.g. Gerya et al., 2004; Menant et al., 2016) suggests that mantle upwelling induced by slab rupture and detachment is dominated from the bottom side of the subducting plate up to the depth of rupture (Fig. 3-9). So, we assume that

the shallowest depth of ~140 km recorded by the cumulate from the lower zone of the Cumulate Member (Fig. 3-8a, Table 3-5) represents the breakoff depth in the Cambrian-Ordovician northeast Japan.

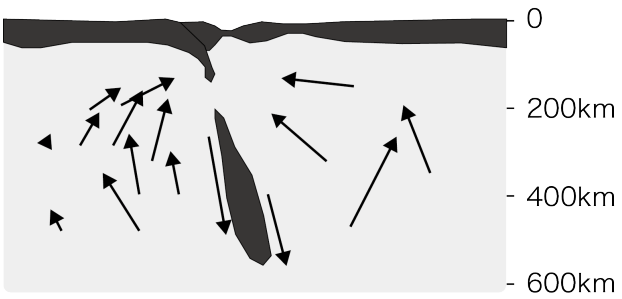

Fig. 3-9: Convective current reproduced in modeling slab breakoff after Gerya et al. (2004), which is simplified by reducing the number of velocity vectors shown by arrows. Solid regions indicate plates. Extensive upwelling of materials from the sub-slab mantle towards the breakoff depths is shown by the arrows in the sub-slab mantle.

We propose an evolutional model for the mantle dynamics of slab breakoff in the Cambrian-Ordovician northeast Japan as illustrated in Fig. 3-10. The model is constrained from the rupture depth (~140 km), temporal variations of the β and solidus depth inferred from their stratigraphic variation in the Cumulate Member and ultramafic dikes (Figs. 3-7c and 3-8a), and melting conditions of the ultramafic dikes (MPT, ~1350 °C; water contents in the source, 0.07 – 0.19 wt%; see, **Chapter 2** section **2.9** and Fig. 2-24). The slab breakoff took place at the depth of ~140 km and triggered counter flows and passive upwelling of the sub-slab mantle from various depths ranging 140 – 250 km, which induced decompressional melting generating magmas for the lower and middle zones of the Cumulate Member (Figs. 3-10a and 3-10b, black dots with

arrows). Because a small extent of melting in the spinel stability field is required (FS > 0.0; Fig. 3-7h), there might have been contribution of melting in the shallower mantle for any stages, which was induced by passive upwelling caused by a tensional tectonics of the Hayachine-Miyamori lithospheric mantle (indicated by open dots with arrows in the uppermost asthenosphere in Figs. 3-10a – 3-10d). During the initial stages, melting of the wedge mantle material affected by slab-derived fluids may have taken place (Figs. 3-10a and 3-10b, blue dots with arrows). This is consistent with the numerical modeling (Freeburn et al., 2017), which suggests flux melting induced by slab-derived fluid is short-lived (a few million years) and synchronous with the slab breakoff. As the slab sunk, the flux melting became suppressed, and upwelling and decompressional melting continued, but the upwelling depths tend to have been narrowed and confined in the depth range 160 – 190 km, which generated magmas for the upper zone of the Cumulate Member (Fig. 3-10c). After the formation of the Cumulate Member, the counter flows waned, and the only a very small amount of magma formed by decompressional melting at the depth of ~170 km, which generated magmas for the ultramafic dikes (Fig. 3-10d).

There are two possibilities resulting in the difference in melting depths. One is variation in mantle potential temperature and the other is water content in the sub-slab mantle. In the former case with nearly homogeneous distribution of water, a variation of MPT of ~150 °C is required (Katz et al., 2003). This is much larger than the present-day MPT variation along mid-ocean ridges ~50 °C (Putirka, 2005). It is even larger than the variation of the global range of MPT ~100 °C (Wiens et al., 2006; see, **Chapter 2** section **2.9.2**). The horizontal scale of mall-scale convection of asthenosphere is estimated to be ~200 – 1000 km (Haxby and Weissel, 1986; Katzman et al., 1998), which may be too large to produce the MPT diversity at a local tectonic setting to focus magmas to the scale of Cumulate Member < 50 km. Therefore, we have to invoke

a variation in water contents in the mantle. The sub-slab mantle is inferred to be at a thermal state represented by MPT of ~1350 °C and near the solidus with H_2O variation, 0.07 – 0.19 wt% (see, **Chapter 2** section **2.9.2**). Water content in the source required to increase the solidus pressures (Table 3-5) is estimated by using water-bearing solidi (Katz et al., 2003), and is plotted against the total amount of influx into the melting system, which is obtained by F x β in Fig. 3-11. They show a positive correlation. The F x β corresponds to water content if the fluid is 100 % H_2O. This supports our proposition that the solidus pressure is controlled by the amount of fluid phase in the source, if we assume that the water contents in the H_2O-rich fluid do not change much with depth in the relevant pressure range. The range of F x β is orders of magnitude smaller than that for $\beta > 0.14$, the latter of which is interpreted to be the amount of fluid influx from the wedge mantle to cause fluxed melting. Therefore, the H_2O-rich fluid that control the solidus pressure is distinct from that is dominant in component of the slab-derived fluids represented by $\beta > 0.14$. Because the water-bearing solidi shift to a higher pressure with increase in water content (Katz et al., 2003), the mantle must have been stratified in H_2O if the MPT was nearly constant.

Ozawa (1983) reported heterogeneity in harzburgite and dunite xenoliths of the Tectonite Member included in wehrlite of the lowest horizon of the Cumulate Member. The Mg# of olivine decreased from 0.912 at the core of a xenolith with 40 mm across to 0.882 at the margin, which coincides with the value of the host wehrlite. He suggested that the profile have caused by the Mg and Fe interdiffusion after the harzburgite and dunite xenoliths were entrapped in the magma of the Cumulate Member until the temperature was too low for these elements to diffuse. By using Mg-Fe interdiffusion coefficients (Dohmen and Chakraborty, 2007), the profile can be reproduced by the Mg-Fe interdiffusion at temperatures ranging 1250 – 1300 ℃ for one millions to a few millions years. The observed Mg# interdiffusion distance (40 mm) indicates a lower

limit of the cooling time scale because an initial value of Mg# is not preserved in the xenolith. We have already estimated the cooling time scale to cause Mg-Fe interdiffusion at the boundary of the ultramafic dike and the host peridotite to be one millions to a few millions years (**Chaptar2**, **2.8.1.2**). These estimates of cooling time scale are comparable or slightly longer for the development of heterogeneity in the harzburgite xenolith in cumulate.

If we consider that the xenoliths occur near the bottom of the cumulate pile and that the ultramafic dikes intruded into somewhat cooled lower zone of the cumulate pile, it is inferred that the maximum time scale of the magmatic events induced by the slab breakoff which maintain high temperatures of the entire Cumulate Member is shorter than a few millions years. The period of significant flux melting peculiar only in the lower and middle horizons of the Cumulate Member (Fig. 3-7c) is, therefore, consistent with the time scale of flux melting estimated in the slab breakoff model after Freeburn et al. (2017). The time scale of slab breakoff event estimated in this study suggests catastrophic nature of slab breakoff, which may trigger episodic cooling of the mantle from the upper thermal boundary layer of the Earth if its frequent occurrence culminates in an ophiolite pulse.

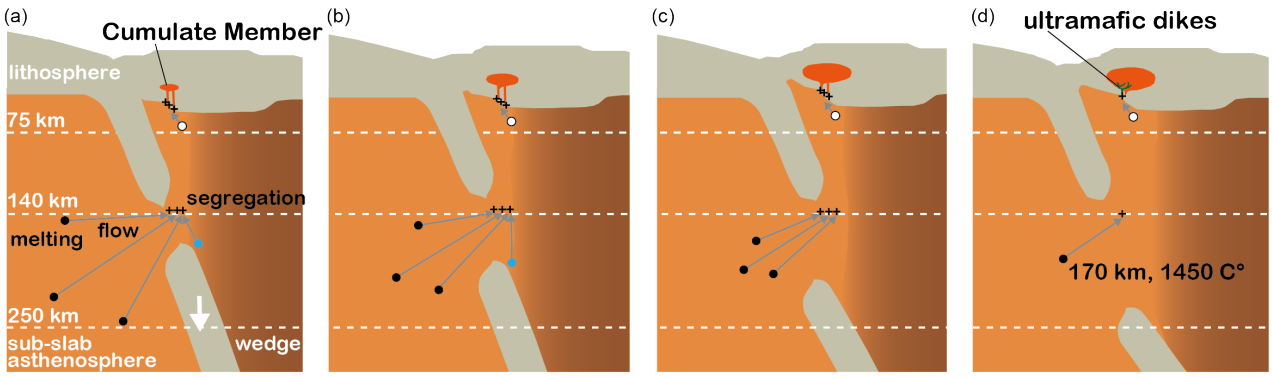

Fig. 3-10: Evolutional slab breakoff model for the Cambrian-Ordovician northern Japan. (a) A slab rupture took place at a depth of ~140 km and triggers passive upwelling of sub-slab mantle from various depths ranging 140 – 250 km (shown by black dots with arrows). A limited upwelling from the wedge mantle affected by slab-derived fluids (shown by a blue dot with arrow) may have taken place. (b) As the slab sunk, the depths of upwelling were converged to 140 – 220 km. (c) In the later stage, the flux meltings became suppressed and the upwelling depths were converged to 160 – 190 km. (d) After the formation of the Cumulate Member, a small amount of melting took place at ~170 km by waned upwelling of the sub-slab mantle.

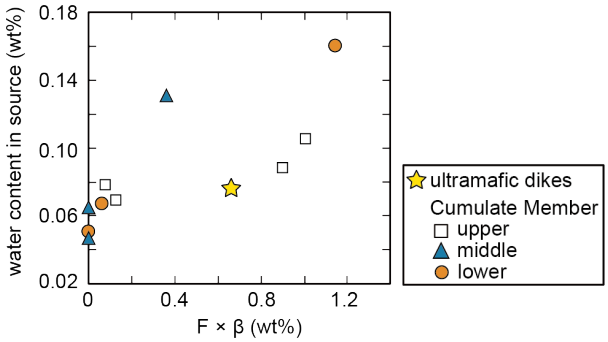

Fig. 3-11: Water content in the source required to increase the solidus pressures (Table 3-5) estimated by using water-bearing solidi (Katz et al., 2003) plotted against the total amount of influx into the melting system, which is obtained by F x β (Fig. 3-7d, Table 3-5) for the ultramafic dikes and Cumulate Member. Symbols are the same as those in Fig 3-7.

Acknowledgement and Funding

I would like to express my deepest gratitude to my supervisor, Prof. K. Ozawa. I also express my heartfelt thanks to Assoc. Prof. T. Iizuka and Dr. H. Yoshida for their supports of major, rare earth, and trace elements analyses at The University of Tokyo, and to Assoc. Prof. T. Kuritani and Prof. M. Nakagawa for the supports of isotope analyses at Hokkaido University.

I am grateful to Prof. J. Bédard at Geological Survey of Canada, Prof. T. Morishita at Kanazawa University, and Mr. S. Sasaki, a former deputy mayor of Hanamaki city for kind helps in the field surveys. I would like to thank to Prof. S. Wallis, Prof. T. Mikouchi, Assoc. Prof. T. Iizuka, Dr. N. Akizawa, Dr. T. Nagaya, and other seminar members for the insightful comments and suggestions in the seminars at The University of Tokyo.

This work was supported by Grant-in-Aid for JSPS Research Fellow (Grant Number 17J06812) and JSPS KAKENHI (Grant Number 17H02982).

References

Abbate, E., Bortolotti, V., Passerini, P., and Principi, G. (1985) The rhythm of Phanerozoic ophiolites. *Ofioliti*, **10**, 109-138.

Abers, G.A., Nakajima, J., van Keken, P.E., Kita, S., and Hacker, B.R. (2013) Thermal-petrological controls on the location of earthquakes within subducting plates. *Earth and Planetary Science Letters*, **369**, 178-187.

Aigner-Torres, M., Blundy, J., Ulmer, P., and Pettke, T. (2007) Laser ablation ICPMS study of trace element partitioning between plagioclase and basaltic melts: an experimental approach. *Contributions to Mineralogy and Petrology*, **153**, 647-667.

Aitken, B.G., and Echeverría, L.M. (1984) Petrology and geochemistry of komatiites and tholeiites from Gorgona Island, Colombia. *Contributions to Mineralogy and Petrology*, **86**, 94-105.

Allard, P., Jean-Baptiste, P., D'Alessandro, W., Parello, F., Parisi, B., and Flehoc, C. (1997) Mantle-derived helium and carbon in groundwaters and gases of Mount Etna, Italy. *Earth and Planetary Science Letters*, **148**, 501-516.

Anderson, D.L. (1994) The sublithospheric mantle as the source of continental flood basalts; the case against the continental lithosphere and plume head reservoirs. *Earth and Planetary Science Letters*, **123**, 269-280.

Arai, S. (1987) An estimation of the least depleted spinel peridotite on the basis of olivine-spinel mantle array. *Neues Jahrbuch für Mineralogie Monatshefte*, **8**, 347-354.

Arevalo Jr., R. and McDonough, W.F. (2008) Tungsten geochemistry and implications for understanding the Earth's interior. *Earth and Planetary Science Letters*, **272**, 656-665.

Arevalo Jr., R., McDonough, W.F., and Luong, M. (2009) The K/U ratio of the silicate Earth: insights into mantle composition, structure and thermal evolution. *Earth and Planetary Science Letters*, **278**, 361-369.

Armienti, P., Innocenti, F., Petrini, R., Pompilio, M., and Villari, L. (1988) Sub-aphiric alkali basalts from Mt. Etna: inferences on the depth and composition of the source magma. *Rendiconti della Societa Italiana di Mineralogia e Petrologia*, **43**, 877-891.

Armienti, P., Tonarini, S., D'Orazio, M., and Innocenti, F. (2004) Genesis and evolution of Mt. Etna alkaline lavas: petrological and Sr-Nd-B isotope constraints. *Periodico di Mineralogia*, **73**, 29-52.

Asimow, P.D., Hirschmann, M.M., and Stolper, E.M. (1997) An analysis of variations in isentropic melt productivity. *Philosophical Transactions of the Royal Society of London. Series A: Mathematical, Physical and Engineering Sciences*, **355**, 255-281.

Ávila, P., and Dávila, F.M. (2018) Heat flow and lithospheric thickness analysis in the Patagonian asthenospheric windows, southern South America. *Tectonophysics*, **747**, 99-107.

Bagnold, R.A. (1954) Experiments on a gravity-free dispersion of large solid spheres in a Newtonian fluid under shear. *Proceedings of the Royal Society of London. Series A*, **225**, 49-63.

Ballhaus, C., Berry, R.F., and Green, D.H. (1991) High pressure experimental calibration of the olivine-orthopyroxene-spinel oxygen geobarometer: implications for the oxidation state of the upper mantle. *Contributions to Mineralogy and Petrology*, **107**, 27-40.

Barragán, R., Baby, P., and Duncan, R. (2005) Cretaceous alkaline intra-plate magmatism in the Ecuadorian Oriente Basin: geochemical, geochronological and tectonic evidence. *Earth and Planetary Science Letters*, **236**, 670-690.

Barreca, G., Branca, S., Corsaro, R. A., Scarfì, L., Cannavò, F., Aloisi, M., Monaco, C. and Faccenna, C. (2020) Slab detachment, mantle flow, and crustal collision in eastern Sicily (southern Italy): Implications on Mount Etna volcanism. *Tectonics*, **39**, doi.org/10.1029/2020TC006188.

Baziotis, I., Economou-Eliopoulos, M., and Asimow, P. D. (2017). Ultramafic lavas and high-Mg basaltic dykes from the Othris ophiolite complex, Greece. *Lithos*, **288**, 231-247.

Beattie, P. (1993) Olivine-melt and orthopyroxene-melt equilibria. *Contributions to Mineralogy and Petrology*, **115**, 103-111.

Beattie, P. (1994) Systematics and energetics of trace-element partitioning between olivine and silicate melts: Implications for the nature of mineral/melt partitioning. *Chemical Geology*, **117**, 57-71.

Beattie, P., Ford, C., and Russell, D. (1991) Partition coefficients for olivine-melt and orthopyroxene-melt systems. *Contributions to Mineralogy and Petrology*, **109**, 212-224.

Berman, R.G. (1988) Internally-consistent thermodynamic data for minerals in the system Na_2O-K_2O-CaO-MgO-FeO-Fe_2O_3-Al_2O_3-SiO_2-TiO_2-H_2O-CO_2. *Journal of Petrology*, **29**, 445-522.

Berman, R.G., and Brown, T.H. (1985) Heat capacity of minerals in the system Na_2O-K_2O-CaO-MgO-FeO-Fe_2O_3-Al_2O_3-SiO_2-TiO_2-H_2O-CO_2: representation, estimation, and high temperature extrapolation. *Contributions to Mineralogy and Petrology*, **89**, 168-183.

Bernard-Griffiths, J., Carpenter, M.S.N., Peucat, J.J., and Jahn, B.M. (1986) Geochemical and isotopic characteristics of blueschist facies rocks from the Ile de Groix, Armorican Massif (northwest France). *Lithos*, **19**, 235-253.

Bezada, M.J., Humphreys, E.D., Toomey, D.R., Harnafi, M., Dávila, J.M., and Gallart, J. (2013) Evidence for slab rollback in westernmost Mediterranean from improved upper mantle imaging. *Earth and Planetary Science Letters*, **368**, 51-60.

Bian, Q.T., Li, D.H., Pospelov, I., Yin, L.M., Li, H.S., Zhao, D.S., Chang, C.F., Luo, X.Q., Gao, S.L., Astrakhantsev, O., and Chamov, N. (2004). Age, geochemistry and tectonic setting of Buqingshan ophiolites, north Qinghai-Tibet Plateau, China. *Journal of Asian Earth Sciences*, **23**, 577-596.

Bijwaard, H., and Spakman, W. (2000) Non-linear global P-wave tomography by iterated linearized inversion. *Geophysical Journal International*, **141**, 71-82.

Borgeaud, A.F., Kawai,K., and Geller, R.J. (2019) Three-Dimensional S Velocity Structure of the Mantle Transition Zone Beneath Central America and the Gulf of Mexico Inferred Using Waveform Inversion. *Journal of Geophysical Research*, **124**, 9664-9681.

Bosch, D., Maury, R.C., Bollinger, C., Bellon, H., and Verdoux, P. (2014) Lithospheric origin for Neogene–quaternary Middle Atlas lavas (Morocco): clues from trace elements and Sr–Nd–Pb–Hf isotopes. *Lithos*, **205**, 247-265.

Burke, K., and Torsvik, T.H. (2004) Derivation of large igneous provinces of the past 200 million years from long-term heterogeneities in the deep mantle. *Earth and Planetary Science Letters*, **227**, 531-538.

Campbell, I.H., and Allen, C.M. (2008) Formation of supercontinents linked to increases in atmospheric oxygen. *Nature Geoscience*, **1**, 554-558.

Cao, L., Wang, Z., Wu, S., and Gao, X. (2014) A new model of slab tear of the subducting Philippine Sea Plate associated with Kyushu–Palau Ridge subduction. *Tectonophysics*, **636**, 158-169.

Churikova, T.G., Gordeychik, B.N., Edwards, B.R., Ponomareva, V.V., and Zelenin, E.A. (2015) The Tolbachik volcanic massif: A review of the petrology, volcanology and eruption history prior to the 2012–2013 eruption. *Journal of Volcanology and Geothermal Research*, **307**, 3-21.

Cipriani, A., Brueckner, H.K., Bonatti, E., and Brunelli, D. (2004) Oceanic crust generated by elusive parents: Sr and Nd isotopes in basalt-peridotite pairs from the Mid-Atlantic Ridge. *Geology*, **32**, 657-660.

Colson, R.O., McKay, G.A., and Taylor, L.A. (1988) Temperature and composition dependencies of trace element partitioning: Olivine/melt and low-Ca pyroxene/melt. *Geochimica et Cosmochimica Acta*, **52**, 539-553.

Condie, K.C. (1998) Episodic continental growth and supercontinents: a mantle avalanche connection? *Earth and Planetary Science Letters*, **163**, 97-108.

Condie, K.C. (2001) Mantle Plumes and Their Record in Earth History. 306 p. Cambridge University Press, UK.

Condie, K.C. (2004) Supercontinents and superplume events: distinguishing signals in the geologic record. *Physics of the Earth and Planetary Interiors*, **146**, 319-332.

Dal Piaz, G.V., Bistacchi, A., and Massironi, M. (2003) Geological outline of the Alps. *Episodes*, **26**, 175-180.

Davaille, A., and Jaupart, C. (1994) Onset of thermal convection in fluids with temperature - dependent viscosity: Application to the oceanic mantle. *Journal of Geophysical Research*, **99**, 19853-19866.

Davies, J.H., and von Blanckenburg, F. (1995) Slab breakoff: a model of lithosphere detachment and its test in the magmatism and deformation of collisional orogens. *Earth and Planetary Science Letters*, **129**, 85-102.

Davies, G.F. (1999) Dynamic Earth: Plates, plumes and mantle convection, 458 p. Cambridge University Press, UK.

Davis, A.S., Clague, D.A., Cousens, B.L., Keaten, R., and Paduan, J.B. (2008) Geochemistry of basalt from the North Gorda segment of the Gorda Ridge: evolution toward ultraslow spreading ridge lavas due to decreasing magma supply. *Geochemistry, Geophysics, Geosystems*, **9**, doi:10.1029/2007GC001775.

de Lis Mancilla, F., Booth-Rea, G., Stich, D., Pérez-Peña, J.V., Morales, J., Azañón, J. M., Martin, R., and Giaconia, F. (2015) Slab rupture and delamination under the Betics and Rif constrained from receiver functions. *Tectonophysics*, **663**, 225-237.

Dilek, Y., and Furnes, H. (2011) Ophiolite genesis and global tectonics: geochemical and tectonic fingerprinting of ancient oceanic lithosphere. *Geological Society of America Bulletin*, **123**, 387-411.

Dilek, Y., and Furnes, H. (2014) Ophiolites and their origins. *Elements*, **10**, 93-100.

Dilek, Y. (2003) Ophiolite pulses, mantle plumes and orogeny. *Geological Society, London, Special Publications*, **218**, 9-19.

Dixon, J.E., Stolper, E., and Delaney, J.R. (1988) Infrared spectroscopic measurements of CO_2 and H_2O in Juan de Fuca Ridge basaltic glasses. *Earth and Planetary Science Letters*, **90**, 87-104.

Doglioni, C., Innocenti, F., and Mariotti, G. (2001) Why Mt Etna?. *Terra Nova*, **13**, 25-31.

Dohmen, R., and Chakraborty, S. (2007) Fe–Mg diffusion in olivine II: point defect chemistry, change of diffusion mechanisms and a model for calculation of diffusion coefficients in natural olivine. *Physics and Chemistry of Minerals*, **34**, 409-430.

Duggen, S., Hoernle, K., van den Bogaard, P., and Garbe-Schönberg, D. (2005) Post-collisional transition from subduction-to intraplate-type magmatism in the westernmost Mediterranean: evidence for continental-edge delamination of subcontinental lithosphere. *Journal of Petrology*, **46**, 1155-1201.

Dunn, T., and Sen, C. (1994) Mineral/matrix partition coefficients for orthopyroxene, plagioclase, and olivine in basaltic to andesitic systems: a combined analytical and experimental study. *Geochimica et Cosmochimica Acta*, **58**, 717-733.

Ehiro, M., and Suzuki, N. (2003) Re-definition of the Hayachine Tectonic Belt of Northeast Japan and a proposal of a new tectonic unit, the Nedamo Belt. *Journal of Structural Geology*, **47**, 13-21 (in Japanese with English abstract).

El Azzouzi, M., Bernard-Griffiths, J., Bellon, H., Maury, R.C., Pique, A., Four- cade, S., Cotten, J. and Hernandez, J. (1999) Evolution of the sources of Moroccan volcanism during the Neogene. *Comptes Rendus de lÕAcade´mie des Sciences*, **329**, 95–102 (in French with English abstract, introduction, major results, and discussion).

Ernst, R.E., and Buchan, K.L. (2003) Recognizing mantle plumes in the geological record. *Annual Review of Earth and Planetary Sciences*, **31**, 469-523.

Ernst, W. G., Maruyama, S., and Wallis, S. (1997) Buoyancy-driven, rapid exhumation of ultrahigh-pressure metamorphosed continental crust. *Proceedings of the National Academy of Sciences*, **94**, 9532-9537.

Fan, J.K., Wu, S.G., and Spence, G. (2015) Tomographic evidence for a slab tear induced by fossil ridge subduction at Manila Trench, South China Sea. *International Geology Review*, **57**, 998-1013.

Fang, A.M. (1998) The sedimentology and tectonic evolution of a fore-arc basin flysch in the Kudi ophiolite, west Kunlun, Xinjiang, China. Ph. D. thesis, Institute of Geology, Academia Sinica, Beijing (in Chinese with English abstract).

Fei, Y. (1995) Thermal expansion. *Mineral physics and crystallography: a handbook of physical constants*, **2**, 29-44.

Freeburn, R., Bouilhol, P., Maunder, B., Magni, V., and Van Hunen, J. (2017) Numerical models of the magmatic processes induced by slab breakoff. *Earth and Planetary Science Letters*, **478**, 203-213.

Frey, F.A. (1969) Rare earth abundances in a high-temperature peridotite intrusion. *Geochim. Cosmochim. Acta*, **33**, 1429-1447

Fujimaki, H., Tatsumoto, M., and Aoki, K. I. (1984) Partition coefficients of Hf, Zr, and REE between phenocrysts and groundmasses. *Journal of Geophysical Research*, **89**, B662-B672.

Furlong, K.P., and Chapman, D.S. (2013) Heat flow, heat generation, and the thermal state of the lithosphere. *Annual Review of Earth and Planetary Sciences*, **41**, 385-410.

Furnes, H., Dilek, Y., and Pedersen, R.B. (2012) Structure, geochemistry, and tectonic evolution of trench-distal backarc oceanic crust in the western Norwegian Caledonides, Solund-Stavfjord ophiolite (Norway). *Geological Society of America Bulletin*, **124**, 1027-1047.

Furnes, H., De Wit, M., and Dilek, Y. (2014) Four billion years of ophiolites reveal secular trends in oceanic crust formation. *Geoscience Frontiers*, **5**, 571-603.

Garcia-Castellanos, D., and Villaseñor, A. (2011) Messinian salinity crisis regulated by competing tectonics and erosion at the Gibraltar arc. *Nature*, **480**, 359-363.

Garzanti, E., Radeff, G., and Malusà, M. G. (2018) Slab breakoff: A critical appraisal of a geological theory as applied in space and time. *Earth-Science Reviews*, **177**, 303-319.

Gasparik, T. (2003) Phase diagrams for geoscientists. 462 p. Berlin Springer.

Gerya, T.V., Yuen, D.A., and Maresch, W.V. (2004) Thermomechanical modelling of slab detachment. *Earth and Planetary Science Letters*, **226**, 101-116.

Gorbatov, A., and Fukao, Y. (2005) Tomographic search for missing link between the ancient Farallon subduction and the present Cocos subduction. *Geophysical Journal International*, **160**, 849-854.

Green, T.H. (1994) Experimental studies of trace-element partitioning applicable to igneous petrogenesis—Sedona 16 years later. *Chemical Geology*, **117**, 1-36.

Grove, T.L., Till, C.B. and Krawczynski, M.J. (2012) The Role of H_2O in Subduction Zone Magmatism. *Annual Review of Earth and Planetary Sciences*, **40**, 413–39

Gvirtzman, Z., and Nur, A. (1999) The formation of Mount Etna as the consequence of slab rollback. *Nature*, **401**, 782-785.

Hall, L.S., Mahoney, J.J., Sinton, J.M., and Duncan, R.A. (2006) Spatial and temporal distribution of a C-like asthenospheric component in the Rano Rahi Seamount Field, East Pacific Rise, 15°-19°S. *Geochemistry, Geophysics, Geosystems*, **7**, doi.org/10.1029/2005GC000994.

Hart, S.R., and Dunn, T. (1993) Experimental cpx/melt partitioning of 24 trace elements. *Contributions to Mineralogy and Petrology*, **113**, 1-8.

Haselton, H.T., and Westrum, E.F. (1980) Low-temperature heat capacities of synthetic pyrope, grossular, and pyrope 60 grossular 40. *Geochimica et Cosmochimica Acta*, **44**, 701-709.

Hauri, E.H., Wagner, T.P., and Grove, T.L. (1994) Experimental and natural partitioning of Th, U, Pb and other trace elements between garnet, clinopyroxene and basaltic melts. *Chemical Geology*, **117**, 149-166.

Hawkesworth, C., Cawood, P., Kemp, T., Storey, C., and Dhuime, B. (2009) A matter of preservation. *Science*, **323**, 49-50.

Haxby, W.F., and Weissel, J.K. (1986). Evidence for small-scale mantle convection from Seasat altimeter data. *Journal of Geophysical Research*, **91**, 3507-3520.

Heit, B., de Lis Mancilla, F, Yuan, X., Morales, J., Stich, D., Martín, R., and Molina-Aguilera, A. (2017) Tearing of the mantle lithosphere along the intermediate-depth seismicity zone beneath the Gibraltar Arc: The onset of lithospheric delamination. *Geophysical Research Letters*, **44**, 4027-4035.

Herzberg, C., and Asimow, P.D. (2008) Petrology of some oceanic island basalts: PRIMELT2. XLS software for primary magma calculation. *Geochemistry, Geophysics, Geosystems*, **9**, doi.org/10.1029/2008GC002057.

Herzberg, C., Condie, K., and Korenaga, J. (2010) Thermal history of the Earth and its petrological expression. *Earth and Planetary Science Letters*, **292**, 79-88.

Hirose, K., and Kushiro, I. (1993) Partial melting of dry peridotites at high pressures: determination of compositions of melts segregated from peridotite using aggregates of diamond. *Earth and Planetary Science Letters*, **114**, 477-489.

Hirschmann, M.M. (2000) Mantle solidus: Experimental constraints and the effects of peridotite composition. *Geochemistry, Geophysics, Geosystems*, **1**, doi:10.1029/2000GC000070.

Hodges, F.N. (1974) The solubility of H_2O in silicate melts. *Carnegie Institution Washington Year book*. **73**, 251-255.

Hollocher, K., and Ruiz, J. (1995) Major and trace element determinations on NIST glass standard reference materials 611, 612, 614 and 1834 by inductively coupled plasma-mass spectrometry. *Geostandards Newsletter*, **19**, 27-34.

Ichiyama Y., Ishiwatari, A., Kimura, J., Senda, R., Kawabata, H., and Tatsumi, Y. (2012) Picrites in central Hokkaido: Evidence of extremely high temperature magmatism in the Late Jurassic ocean recorded in an accreted oceanic plateau. *Geology*, **40**, 411-414.

Irvine, T.N.J., and Baragar, W.R.A.F. (1971) A guide to the chemical classification of the common volcanic rocks. *Canadian Journal of Earth Science*, **8**, 523-548.

Irving, A.J., and Frey, F.A. (1984) Trace element abundances in megacrysts and their host basalts: constraints on partition coefficients and megacryst genesis. *Geochimica et Cosmochimica Acta*, **48**, 1201-1221.

Ishiwatari, A. (1994) Circum-Pacific Phanerozoic multiple ophiolite belts. In Circum-Pacific Ophiolites. Eds., A. Ishiwatari, J. Malpas, H. Ishizuka. *Proceedings of the 29th International Geological Congress Part D*, 7-28.

Itano, K., and Iizuka, T. (2017) Unraveling the mechanism and impact of oxide production in LA-ICP-MS by comprehensive analysis of REE-Th-U phosphates. *Journal of Analytical Atomic Spectrometry*, **32**, 2003-2010.

Jamieson, R.A. (1986) PT paths from high temperature shear zones beneath ophiolites. *Journal of Metamorphic Geology*, **4**, 3-22.

Jenner, G.A., Foley, S.F., Jackson, S.E., Green, T.H., Fryer, B.J., and Longerich, H.P. (1993) Determination of partition coefficients for trace elements in high pressure-temperature

experimental run products by laser ablation microprobe-inductively coupled plasma-mass spectrometry (LAM-ICP-MS). *Geochimica et Cosmochimica Acta*, **57**, 5099-5103.

Jiang, C.F., Yang, J.S., Feng, B.G., Zhu, Z.Z., Zhao, M., Chai, Y.C., Shi, X.D., Wang, H.D., and Hu, J.Q. (1992) Opening–closing tectonics of the Kunlun mountains. *Geological memoirs*, **5**, 12 p., Geological Publishing House, Beijing (in Chinese with English abstract).

Johnson, K.T.M. (1994) Experimental cpx/and garnet/melt partitioning of REE and other trace elements at high pressures: petrogenetic implications. *Mineralogical Magazine*, **58**, 454-455.

Katsura, T., Shatskiy, A., Manthilake, M.G.M., Zhai, S., Fukui, H., Yamazaki, D., Matsuzaki, T, Yoneda, A., Ito, E., Kuwata, A., and others. (2009) Thermal expansion of forsterite at high pressures determined by in situ X-ray diffraction: The adiabatic geotherm in the upper mantle. *Physics of the Earth and Planetary Interiors*, **174**, 86-92.

Katz, R.F., Spiegelman, M., and Langmuir, C.H. (2003) A new parameterization of hydrous mantle melting. *Geochemistry, Geophysics, Geosystems*, **4**, doi:10.1029/2002GC000433.

Katzman, R., Zhao, L., and Jordan, T.H. (1998) High-resolution, two-dimensional vertical tomography of the central Pacific mantle using ScS reverberations and frequency-dependent travel times. *Journal of Geophysical Research* **103**, 17933-17971.

Kawamura, T., Uchino, T., Kawamura, M., Yoshida, K., Nakamura, M., and Nnagata, H. (2013) Geology of the Hayachine San district. Quadrangle Series scale 1:50,000, Akita (6) no. 24, Geological Survey of Japan AIST 13-G00976 (in Japanese with English abstract).

Kawasaki, T., and Ito, E. (1994) An experimental determination of the exchange reaction of Fe^{2+} and Mg^{2+} between olivine and Ca-rich clinopyroxene. *American Mineralogist*, **79**, 461-477.

Kelemen, P.B. and Dunn, J.T. (1992) Depletion of Nb relative to other highly incompatible elements by melt/rock reaction on the upper mantle. *Eos (Trans. Am. Geophys. Union)*, **73**, 656-657.

Kelemen, P.B., Johnson, K.T.M., Kinzler, R.J., and Irving, A.J. (1990) High-field-strength element depletions in arc basalts due to mantle–magma interaction. *Nature*, **345**, 521-524.

Kelemen, P.B., Yogodzinski, G.M., and Scholl, D. W. (2003). Along-strike variation in the Aleutian island arc: genesis of high Mg# andesite and implications for continental crust. *Geophysical Monograph Series*, **138**, 223-276.

Kennedy, A.K., Lofgren, G.E., and Wasserburg, G.J. (1993) An experimental-study of trace-element partitioning between olivine, ortho-pyroxene and melt in chondrules - Equilibrium values and kinetic effects. *Earth and Planetary Science Letters*. **115**, 177-195.

Kerr, A.C., Saunders, A.D., Tarney, J., Berry, N.H., and Hards, V.L. (1995) Depleted mantle-plume geochemical signatures: No paradox for plume theories. *Geology*, **23**, 843-846.

Kerr, A.C., Marriner, G.F., Arndt, N.T., Tarney, J., Nivia, A., Saunders, A.D., and Duncan, R.A. (1996) The petrogenesis of Gorgona komatiites, picrites and basalts: new field, petrographic and geochemical constraints. *Lithos*, **37**, 245-260.

Kessel, R., Schmidt, M.W., Ulmer, P., and Pettke, T. (2005) Trace element signature of subduction-zone fluids, melts and supercritical liquids at 120-170 km depth. *Nature*, **437**, 724-727.

Kimura, J.I., Gill, J.B., van Keken, P.E., Kawabata, H., and Skora, S. (2017) Origin of geochemical mantle components: Role of spreading ridges and thermal evolution of mantle. *Geochemistry, Geophysics, Geosystems*, **18**, 697-734.

Kimura, T., Ozawa, K., Kuritani, T., Iizuka, T., and Nakagawa, M. (2020) Thermal state of the upper mantle and the origin of the Cambrian-Ordovician ophiolite pulse: Constraints from ultramafic dikes of the Hayachine-Miyamori ophiolite. *American Mineralogist*, **105**, 1778-1801.

King, E.G. (1957) Low Temperature Heat Capacities and Entropies at 298.15° K. of Some Crystalline Silicates Containing Calcium. *Journal of the American Chemical Society*, **79**, 5437-5438.

Kinzler, R.J., and Grove, T.L. (1992) Primary magmas of mid-ocean ridge basalts: 2. Applications. *Journal of Geophysical Research*, **97**, 6885-6906.

Kinzler, R.J., Grove, T.L., and Recca, S.I. (1990) An experimental study on the effect of temperature and melt composition on the partitioning of nickel between olivine and silicate melt. *Geochimica et Cosmochimica Acta*, **54**, 1255-1265.

Kojitani, H. and Akaogi, M. (1997) Melting enthalpies of mantle peridotite: calorimetric determinations in the system CaO-MgO-Al_2O_3-SiO_2 and application to magma generation. *Earth and Planetary Science Letters*, **153**, 209-222.

Komar, P.D. (1972) Flow differentiation in igneous dikes and sills: profiles of velocity and phenocryst concentration. *Geological Society of America Bulletin*, **83**, 3443-3448.

Korenaga, J. (2008a) Plate tectonics, flood basalts, and the evolution of Earth's oceans. *Terra Nova*, **20**, 419–439.

Korenaga, J. (2008b) Urey ratio and the structure and evolution of Earth's mantle. *Reviews of Geophysics*. **46**, doi.org/10.1029/2007RG000241.

Korenaga, J. and Jordan, T.H. (2003) Physics of multiscale convection in Earth's mantle: Onset of sublithospheric convection. *Journal of Geophysical Research*, **108**, doi:10.1029/2002JB001760.

Korenaga, J., and Jordan, T.H. (2004) Physics of multiscale convection in Earth's mantle: Evolution of sublithospheric convection. *Journal of Geophysical Research*, 109, doi:10.1029/2002JB001760.

Koulakov, I., and Sobolev, S.V. (2006) A tomographic image of Indian lithosphere break-off beneath the Pamir–Hindukush region. *Geophysical Journal International*, **164**, 425-440.

Koulakov, I., Gordeev, E.I., Dobretsov, N.L., Vernikovsky, V.A., Senyukov, S., and Jakovlev, A. (2011) Feeding volcanoes of the Kluchevskoy group from the results of local earthquake tomography. *Geophysical research letters*, **38**, doi.org/10.1029/2011GL046957.

Koulakov, I., Shapiro, N.M., Sens-Schönfelder, C., Luehr, B.G., Gordeev, E.I., Jakovlev, A., Abkadyrov, I., Chebrov, V.C., Bushenkova, N., and others. (2020) Mantle and crustal sources of magmatic activity of Klyuchevskoy and surrounding volcanoes in Kamchatka inferred from earthquake tomography. *Journal of Geophysical Research*, **125,** doi.org/10.1029/2020JB020097.

Krupka, K.M., Hemingway, B.S., Robie, R. A., and Kerrick, D.M. (1985) High-temperature heat capacities and derived thermodynamic properties of anthophyllite, diopside, dolomite, enstatite, bronzite, talc, tremolite and wollastonite. *American Mineralogist*, **70**, 261-271.

Kuritani, T., Yokoyama, T., and Nakamura, E. (2008) Generation of rear-arc magmas induced by influx of slab-derived supercritical liquids: Implications from alkali basalt lavas from Rishiri Volcano, Kurile arc. *Journal of Petrology*, **49**, 1319-1342.

Kuritani, T., Yoshida, T., Kimura, J. I., Takahashi, T., Hirahara, Y., Miyazaki, T., Senda, R., Chang, Q., and Ito, Y. (2014a) Primary melt from Sannome-gata volcano, NE Japan arc: constraints on generation conditions of rear-arc magmas. *Contributions to Mineralogy and Petrology*, **167**, 969.

Kuritani, T., Yoshida, T., Kimura, J. I., Hirahara, Y., and Takahashi, T. (2014b) Water content of primitive low-K tholeiitic basalt magma from Iwate Volcano, NE Japan arc: implications for differentiation mechanism of frontal-arc basalt magmas. *Mineralogy and Petrology*, **108**, 1-11.

Kurth, M., Sassen, A., and Galer, S.J. (2004) Geochemical and isotopic heterogeneities along an island arc-spreading ridge intersection: Evidence from the Lewis Hills, Bay of Islands Ophiolite, Newfoundland. *Journal of Petrology*, **45**, 635-668.

Lange, R.A., and Carmichael, I.S. (1987) Densities of Na_2O-K_2O-CaO-MgO-FeO-Fe_2O_3-Al_2O_3-TiO_2-SiO_2 liquids: new measurements and derived partial molar properties. *Geochimica et Cosmochimica Acta*, **51**, 2931-2946.

Laporte, D., Toplis, M.J., Seyler, M., and Devidal, J.L. (2004) A new experimental technique for extracting liquids from peridotite at very low degrees of melting: application to partial melting of depleted peridotite. *Contributions to Mineralogy and Petrology*, **146**, 463-484.

Leake, B., Woolley, A.R., Arps, C.E.S., Birch, W.D., Gilbert, M.C., Grice, J.D., Hawthorne, F.C., Kato, A., Kisch, H.J., Krivovichev, V.G., and others. (1997) Nomenclature of amphiboles: re- port of the subcommittee on amphiboles of the International Mineralogical Association, Commission on New Minerals and Mineral Names. *European Journal of Mineralogy*, **9**, 623-651.

Lee, C.T.A., Luffi, P., Plank, T., Dalton, H., and Leeman, W.P. (2009) Constraints on the depths and temperatures of basaltic magma generation on Earth and other terrestrial planets using new thermobarometers for mafic magmas. *Earth and Planetary Science Letters*, **279**, 20-33.

Levin, V., Shapiro, N., Park, J., and Ritzwoller, M. (2002) Seismic evidence for catastrophic slab loss beneath Kamchatka. *Nature*, **418**, 763-767.

Lissenberg, C.J., Van Staal, C.R., Bédard, J.H., and Zagorevski, A. (2005) Geochemical constraints on the origin of the Annieopsquotch ophiolite belt, Newfoundland Appalachians. *Geological Society of America Bulletin*, **117**, 1413-1426.

Lister, C.R.B., Sclater, J.G., Davis, E.E., Viilinger, H., and Nagihara, S. (1990) Heat flow maintained in ocean basins of great age: Investigations in the north-equatorial west Pacific, *Geophysical Journal International*, **102**, 603-630.

Lister, G.S., White, L.T., Hart, S., and Forster, M.A. (2012) Ripping and tearing the rolling-back New Hebrides slab. *Australian Journal of Earth Sciences*, **59**, 899-911.

Liu, S., Suardi, I., Yang, D., Wei, S., and Tong, P. (2018) Teleseismic traveltime tomography of northern Sumatra. *Geophysical Research Letters*, **45**, 13-231.

Machetel, P., and Humler, E. (2003) High mantle temperature during Cretaceous avalanche. *Earth and Planetary Science Letters*, **208**, 125-133.

Maekawa, H. (1981) Geology of the Motai Group in the southwestern part of the Kitakami Mountains. *Journal of the Geological Society of Japan*, **87**, 543-554.

Maekawa, H. (1983) Submarine sliding deposits and their modes of occurrence of the Kamuikotan metamorphic rocks in the Biei area, Hokkaido, Japan. *University of Tokyo Journal of the Faculty of Science*, Section II, **20**, 489-507.

Mahoney, J.J., Graham, D.W., Christie, D.M., Johnson, K.T.M., Hall, L.S., and Vonderhaar, D.L. (2002) Between a hotspot and a cold spot: isotopic variation in the Southeast Indian Ridge asthenosphere, 86°E-118°E. *Journal of Petrology*, **43**, 1155-1176.

Marty, B., Trull, T., Lussiez, P., Basile, I., and Tanguy, J.C. (1994) He, Ar, O, Sr and Nd isotope constraints on the origin and evolution of Mount Etna magmatism. *Earth and Planetary Science Letters*, **126**, 23-39.

Maruyama, S. (1994) Plume tectonics. *Journal-Geological Survey of Japan*, **100**, 24-49.

Matsui, Y., Onuma, N., Nagasawa, H., Higuchi, H., and Banno, S. (1977) Crystal structure control in trace element partition between crystal and magma. *Tectonics*, **100**, 315-324.

McDonough, W.F., and Sun, S.S. (1995) The composition of the Earth. *Chemical geology*, **120**, 223-253.

McKenzie, D., and Bickle, M.J. (1988) The volume and composition of melt generated by extension of the lithosphere. *Journal of Petrology*, **29**, 625-679.

McKenzie, D. and O'Nions, R. K. (1991) Partial melt distributions from inversion of rare earth element concentrations. *Journal of Petrology*, **32**, 1021-1091.

Médard, E., and Grove, T.L. (2008) The effect of H_2O on the olivine liquidus of basaltic melts: experiments and thermodynamic models. *Contributions to Mineralogy and Petrology*, **155**, 417-432.

Menant, A., Sternai, P., Jolivet, L., Guillou-Frottier, L., and Gerya, T. (2016) 3D numerical modeling of mantle flow, crustal dynamics and magma genesis associated with slab roll-back and tearing: The eastern Mediterranean case. *Earth and Planetary Science Letters*, **442**, 93-107.

Mibe, K., Kanzaki, M., Kawamoto, T., Matsukage, K.N., Fei, Y., and Ono, S. (2007) Second critical endpoint in the peridotite-H_2O system. *Journal of Geophysical Research*, **112**, doi.org/10.1029/2005JB004125C.

Miller, M.S., Gorbatov, A., and Kennett, B.L. (2006) Three-dimensional visualization of a near-vertical slab tear beneath the southern Mariana arc. *Geochemistry, Geophysics, Geosystems,* **7**, doi.org/10.1029/2005GC001110

Nakai, S., Wakita, H., Nuccio, M.P., and Italiano, F. (1997) MORB-type neon in an enriched mantle beneath Etna, Sicily. *Earth and Planetary Science Letters*, **153**, 57-66.

Nauret, F., Abouchami, W., Galer, S.J.G., Hofmann, A.W., Hemond, C., Chauvel, C., and Dyment, J. (2006) Correlated trace element-Pb isotope enrichments in Indian MORB along 18-20°S, Central Indian Ridge. *Earth and Planetary Science Letters*, **245**, 137-152.

Newman, S., and Lowenstern, J.B. (2002) VolatileCalc: a silicate melt-H_2O-CO_2 solution model written in Visual Basic for Excel. *Computers and Geosciences*, **28**, 597-604.

Nicholls, I.A., and Harris, K.L. (1980) Experimental rare earth element partition coefficients for garnet, clinopyroxene and amphibole coexisting with andesitic and basaltic liquids. *Geochimica et Cosmochimica Acta*, **44**, 287-308.

Niida, K., Kito, N., and Miyashita, S. (1999) Picrite from the uppermost part of the Lower Sorachi Group, Central Hokkaido. *Ophiolites and accretionary tectonics, Geological Society of Japan Memoir*, **52**, 77-82.

Nikogosyan, I.K., and Sobolev, A.V. (1997) Ion-microprobe analysis of melt inclusions in olivine: experience in estimating the melt-olivine distribution coefficients of impurity elements. *Geokhimiya*, **2**, 149-157. (in Russian with English abstract).

Niu, F., Solomon, S.C., Silver, P.G., Suetsugu, D., and Inoue, H. (2002) Mantle transition-zone structure beneath the South Pacific Superswell and evidence for a mantle plume underlying the Society hotspot. *Earth and Planetary Science Letters*, **198**, 371–380.

Niu, Y.L. (2017) Slab breakoff: a causal mechanism or pure convenience? *Science bulletin*, **62**, 456-461.

Noguchi, T., Shinjo, R., Michihiro, I.T.O., Takada, J., and Oomori, T. (2011) Barite geochemistry from hydrothermal chimneys of the Okinawa Trough: insight into chimney

formation and fluid/sediment interaction. *Journal of Mineralogical and Petrological Sciences*, **106**, 26-35.

Nolet, G. (2009) Slabs do not go gently. *Science*, **324**, 1152-1153.

O'Neill, H.S. (1987) Quartz-fayalite-iron and quartz-fayalite-magnetite equilibria and the free energy of formation of fayalite (Fe_2SiO_4) and magnetite (Fe_3O_4). *American Mineralogist*, **72**, 67-75.

Obayashi, M., Yoshimitsu, J., and Fukao, Y. (2009) Tearing of stagnant slab. *Science*, **324**, 1173-1175.

Ozawa, K. (1983) Relationships between tectonite and cumulate in ophiolites: the Miyamori ultramafic complex, Kitakami Mountains, northeast Japan. *Lithos*, **16**, 1-16.

Ozawa, K. (1984) Geology of the Miyamori ultramafic complex in the Kitakami Mountains, northeast Japan. *Journal of the Geological Society of Japan*, **90**, 697-716.

Ozawa, K. (1986) Partitioning of elements between constituent minerals in peridotites from the Miyamori ultramafic complex, Kitakami Mountains, Northeast Japan: estimation of P– T condition and igneous composition of minerals. *Journal of the Faculty of Science the University of Tokyo Section II*, **21**, 116-137.

Ozawa, K. (1987a) Origin of the Miyamori ophiolitic complex, northeast Japan: TiO_2/K_2O of amphibole and TiO_2/Na_2O of clinopyroxene as discriminants for the tectonic setting of ophiolites. Eds., Malpas, J., Moores, E., Panayiotou, A., Xenophontos, C, *Proceedings of the Ophiolite Conference*, 485-495.

Ozawa K., (1987b) Petrology of aluminous spinel peridotites and pyroxenites of the Miyamori ultramafic complex, northeast Japan. *Journal of the Faculty of Science, University of Tokyo. Section II*, **21**, 309-32.

Ozawa, K. (1988) Ultramafic tectonite of the Miyamori ophiolitic complex in the Kitakami Mountains, Northeast Japan: hydrous upper mantle in an island arc. *Contributions to Mineralogy and Petrology*, **99**, 159-175.

Ozawa, K. (1994) Melting and melt segregation in the mantle wedge above a subduction zone: evidence from the chromite-bearing peridotites of the Miyamori ophiolite complex, northeastern Japan. *Journal of Petrology*, **35**, 647-678.

Ozawa, K. (2001) Mass balance equations for open magmatic systems: Trace element behavior and its application to open system melting in the upper mantle. *Journal of Geophysical Research*, **106**, 13407-13434.

Ozawa, K., and Shimizu, N. (1995) Open-system melting in the upper mantle: Constraints from the Hayachine-Miyamori ophiolite, northeastern Japan. *Journal of Geophysical Research*, **100**, 22315-22335.

Ozawa, K., Shibata, K., and Uchiumi, S. (1988) K-Ar ages of hornblende in gabbroic rocks from the Miyamori ultramafic complex of the Kitakami Mountains. *Journal of Mineralogy, Petrology and Economic Geology*, **83**, 150-159 (in Japanese with English abstract).

Ozawa, K., Maekawa, H., and Ishiwatari A. (2013) Reconstruction of the structure of Ordovician-Devonian arc system and its evolution processes: Hayachine-Miyamori ophiolite and Motai high-pressure metamorphic rocks in Iwate Prefecture. *Journal of the Geological Society of Japan*, **119**, 134-53 (in Japanese with English abstract).

Ozawa, K., Maekawa, H., Shibata, K., Asahara, Y., and Yoshikawa, M. (2015) Evolution processes of Ordovician-Devonian arc system in the South-Kitakami Massif and its relevance to the Ordovician ophiolite pulse. *Island Arc*, **24**, 73-118.

Pavoni, N. (1997) Geotectonic bipolarity-evidence of bicellular convection in the Earth's mantle. *South African Journal of Geology*, **100**, 291-299.

Peacock, S.M. (2003) Thermal structure and metamorphic evolution of subducting slabs. *Geophysical Monograph-American Geophysical Union*, **138**, 7-22.

Pearce, J.A. (2008) Geochemical fingerprinting of oceanic basalts with applications to ophiolite classification and the search for Archean oceanic crust. *Lithos*, **100**, 14-48.

Pearce, J.A., Ernewein, M., Bloomer, S.H., Parson, L.M., Murton, B.J., and Johnson, L.E. (1994) Geochemistry of Lau Basin volcanic rocks: influence of ridge segmentation and arc proximity. *Geological Society, London, Special Publications*, **81**, 53-75.

Pearce, J.A., Stern, R.J., Bloomer, S.H., and Fryer, P. (2005) Geochemical mapping of the Mariana arc-basin system: Implications for the nature and distribution of subduction components. *Geochemistry, Geophysics, Geosystems,* **6**, doi:10.1029/2004GC000895.

Peccerillo, A. (2005). Plio-quaternary volcanism in Italy. 217-251 p. Springer-Verlag Berlin Heidelberg.

Pedro, J., Araújo, A., Fonseca, P., Tassinari, C., and Ribeiro, A. (2010) Geochemistry and U- Pb zircon age of the internal Ossa-Morena zone ophiolite sequences: a remnant of Rheic ocean in SW Iberia. *Ofioliti*, **35**, 117-130.

Peng, M., Jiang, M., Li, Z.H., Xu, Z., Zhu, L., Chan, W., Chen, Y., Wang, Y., Yu, C., and others. (2016) Complex Indian subduction style with slab fragmentation beneath the Eastern Himalayan Syntaxis revealed by teleseismic P-wave tomography. *Tectonophysics*, **667**, 77-86.

Petry, C., Chakraborty, S., and Palme, H. (2004) Experimental determination of Ni diffusion coefficients in olivine and their dependence on temperature, composition, oxygen fugacity, and crystallographic orientation. *Geochimica et Cosmochimica Acta*, **68**, 4179-4188.

Pin, C., and Zalduegui, J.S. (1997) Sequential separation of light rare-earth elements, thorium and uranium by miniaturized extraction chromatography: application to isotopic analyses of silicate rocks. *Analytica Chimica Acta*, **339**, 79-89.

Pin, C., Briot, D., Bassin, C., and Poitrasson, F. (1994) Concomitant separation of strontium and samarium-neodymium for isotopic analysis in silicate samples, based on specific extraction chromatography. *Analytica Chimica Acta*, **298**, 209-217.

Portner, D.E., Delph, J.R., Biryol, C.B., Beck, S.L., Zandt, G., Özacar, A.A., Sandvol, E., and Türkelli, N. (2018) Subduction termination through progressive slab deformation across Eastern Mediterranean subduction zones from updated P-wave tomography beneath Anatolia. *Geosphere*, **14**, 907-925.

Portnyagin, M., Hoernle, K., Avdeiko, G., Hauff, F., Werner, R., Bindeman, I., Uspensky, Vitaly., and Garbe-Schönberg, D. (2005) Transition from arc to oceanic magmatism at the Kamchatka-Aleutian junction. *Geology*, **33**, 25-28.

Portnyagin, M., Bindeman, I., Hoernle, K., and Hauff, F. (2007). Geochemistry of Primitive Lavas of the Central Kamchatka Depression: Magma Generation at the Edge of the Pacific Plate. *Geophysical Monograph Series*, **172**, doi.org/10.1029/172GM16.

Putirka, K.D. (2005) Mantle potential temperatures at Hawaii, Iceland, and the mid‐ocean ridge system, as inferred from olivine phenocrysts: Evidence for thermally driven mantle plumes. *Geochemistry, Geophysics, Geosystems*, **6**, doi:10.1029/2005GC000915.

Putirka, K.D. (2008) Thermometers and barometers for volcanic systems. *Reviews in mineralogy and geochemistry*, **69**, 61-120.

Rhodes, J.M., and Vollinger, M.J. (2004) Composition of basaltic lavas sampled by phase-2 of the Hawaii Scientific Drilling Project: Geochemical stratigraphy and magma types. *Geochemistry, Geophysics, Geosystems*, **5**, doi:10.1029/2002GC000434.

Richter, F.M., and Parsons, B. (1975) On the interaction of two scales of convection in the mantle. *Journal of Geophysical Research*, **80**, 2529-2541.

Robie, R.A., Hemingway, B.S., and Takei, H. (1982a) Heat capacities and entropies of Mg_2SiO_4, Mn_2SiO_4, and Co_2SiO_4 between 5 and 380 K. *American Mineralogist*, **67**, 470-482.

Robie, R.A., Finch, C.B., and Hemingway, B.S. (1982b) Heat capacity and entropy of fayalite (Fe_2SiO_4) between 5.1 and 383 K: comparison of calorimetric and equilibrium values for the QFM buffer reaction. *American Mineralogist*, **67**, 463-469.

Rosell, O., Martí, A., Marcuello, À., Ledo, J., Queralt, P., Roca, E., and Campanyà, J. (2011) Deep electrical resistivity structure of the northern Gibraltar Arc (western Mediterranean): evidence of lithospheric slab break-off. *Terra Nova*, **23**, 179-186.

Rosenbaum, G., Gasparon, M., Lucente, F.P., Peccerillo, A., and Miller, M.S. (2008) Kinematics of slab tear faults during subduction segmentation and implications for Italian magmatism. *Tectonics*, **27**, doi.org/10.1029/2007TC002143.

Sack, R.O., Carmichael, I.S.E., Rivers, M.L., and Ghiorso, M.S. (1980) Ferric-ferrous equilibria in natural silicate liquids at 1 bar. *Contributions to Mineralogy and Petrology*, **75**, 369-376.

Sakuyama, T., Ozawa, K., Sumino, H., and Nagao, K. (2009) Progressive melt extraction from upwelling mantle constrained by the Kita-Matsuura basalts in NW Kyushu, SW Japan. *Journal of Petrology*, **50**, 725-779.

Sakuyama, T., Nakai, S.I., Yoshikawa, M., Shibata, T., and Ozawa, K. (2014) Progressive Interaction between Dry and Wet Mantle during High-temperature Diapiric Upwelling: Constraints from Cenozoic Kita-Matsuura Intraplate Basalt Province, Northwestern Kyushu, Japan. *Journal of Petrology*, **55,** 1083-1128.

Sánchez-Martínez, S., Arenas, R., Andonaegui, P., Catalán, J.R.M., and Pearce, J.A. (2007) Geochemistry of two associated ophiolites from the Cabo Ortegal Complex (Variscan belt of NW Spain). *Geological Society of America Memoirs*, **200**, 445-467.

Sandiford, M. (2008). Seismic moment release during slab rupture beneath the Banda Sea. *Geophysical Journal International*, **174**, 659-671.

Scarfì, L., Barberi, G., Barreca, G., Cannavò, F., Koulakov, I., and Patanè, D. (2018) Slab narrowing in the Central Mediterranean: the Calabro-Ionian subduction zone as imaged by high resolution seismic tomography. *Scientific reports*, **8**, 1-12.

Scire, A., Biryol, C. B., Zandt, G., and Beck, S. (2015) Imaging the Nazca slab and surrounding mantle to 700 km depth beneath the central Andes (18 S to 28 S). *Geodynamics of a Cordilleran Orogenic System: The Central Andes of Argentina and Northern Chile*. 23-41 p. Geological Society of America Memoir.

Seber, D., Barazangi, M., Ibenbrahim, A., and Demnati, A. (1996) Geophysical evidence for lithospheric delamination beneath the Alboran Sea and Rif–Betic mountains. *Nature*, **379**, 785-790.

Shervais, J.W. (1982) Ti-V plots and the petrogenesis of modern and ophiolitic lavas. *Earth and Planetary Science Letters*, 59, 101-118.

Shervais, J.W. (2001) Birth, death, and resurrection: The life cycle of suprasubduction zone ophiolites. *Geochemistry, Geophysics, Geosystems*, **2**, doi:10.1029/2000GC000080.

Shibata, K., and Ozawa, K. (1992) Ordovician arc ophiolite, the Hayachine and Miyamori complexes, Kitakami Mountains, Northeast Japan: isotopic ages and geochemistry. *Geochemical Journal*, **26**, 85-97.

Shimizu, K., Liang, Y., Sun, C., Jackson, C.R., and Saal, A.E. (2017) Parameterized lattice strain models for REE partitioning between amphibole and silicate melt. *American Mineralogist*, **102**, 2254-2267.

Shukuno, H., Tamura, Y., Tani, K., Chang, Q., Suzuki, T., and Fiske, R.S. (2006) Origin of silicic magmas and the compositional gap at Sumisu submarine caldera, Izu–Bonin arc, Japan. *Journal of Volcanology and Geothermal Research*, **156**, 187-216.

Sigloch, K., McQuarrie, N., and Nolet, G. (2008) Two-stage subduction history under North America inferred from multiple-frequency tomography. *Nature Geoscience*, **1**, 458-462.

Sims, K.W.W., Goldstein, S.J., Blichert-Toft, J., Perfit, M.R., Kelemen, P., Fornari, D.J., Michael, P., Murrell, M.T., Hart, S.R., DePaolo, D.J., and others. (2002) Chemical and isotopic constraints on the generation and transport of magma beneath the East Pacific Rise. *Geochimica et Cosmochimica Acta*, **66**, 3481-3504.

Skulski, T., Minarik, W., and Watson, E.B. (1994) High-pressure experimental trace-element partitioning between clinopyroxene and basaltic melts. *Chemical Geology*, **117**, 127-147.

Slagstad, T. (2003) Geochemistry of trondhjemites and mafic rocks in the Bymarka ophiolite fragment, Trondheim, Norway: petrogenesis and tectonic implications. *Norwegian Journal of Geology*, **83**, 167-185.

Solomatov, V. S., and Moresi, L. N. (2000) Scaling of time-dependent stagnant lid convection: Application to small - scale convection on Earth and other terrestrial planets. *Journal of Geophysical Research*, **105**, 21795-21817.

Spakman, W. (1986) The upper mantle structure in the central European-Mediterranean region. In *Proceedings of the Third Workshop on the European Geotraverse Project*, Eds, Freeman, R., Mueller, S., and Giese, P., 215-221.

Spakman, W., Wortel, M.J.R., and an Vlaar, N.J. (1988) The Hellenic subduction zone: a tomographic image and its geodynamic implications. *Geophysical research letters*, **15**, 60-63.

Spakman, W., and Wortel, R. (2004) A tomographic view on western Mediterranean geodynamics. In *The TRANSMED atlas. The Mediterranean region from crust to mantle*, 31-52 p. Springer, Berlin, Heidelberg.

Stebbins, J.F., Carmichael, I.S.E., and Moret, L.K. (1984) Heat capacities and entropies of silicate liquids and glasses. *Contributions to Mineralogy and Petrology*, **86**, 131-148.

Stern, R.J. (2005) Evidence from ophiolites, blueschists, and ultrahigh-pressure metamorphic terranes that the modern episode of subduction tectonics began in Neoproterozoic time. *Geology*, **33**, 557-560.

Sui, Q.L., Wang, Q., Zhu, D.C., Zhao, Z.D., Chen, Y., Santosh, M., Hu, Z.C., Yuan, H.L., and Mo, X.X. (2013) Compositional diversity of ca. 110 Ma magmatism in the northern Lhasa Terrane, Tibet: implications for the magmatic origin and crustal growth in a continent–continent collision zone. *Lithos*, **168**, 144-159.

Sun, C., and Liang, Y. (2012) Distribution of REE between clinopyroxene and basaltic melt along a mantle adiabat: effects of major element composition, water, and temperature. *Contributions to Mineralogy and Petrology*, **163**, 807-823.

Sun, C., and Liang, Y. (2013) The importance of crystal chemistry on REE partitioning between mantle minerals (garnet, clinopyroxene, orthopyroxene, and olivine) and basaltic melts. *Chemical Geology*, **358**, 23-36.

Sun, S.S., and McDonough, W.S. (1989) Chemical and isotopic systematics of oceanic basalts: implications for mantle composition and processes. *Geol. Soc. London, Special Publications*, **42**, 313-345.

Sun, W.D., Bennett, V.C., Eggins, S.M., Arculus, R.J., and Perfit, M.R. (2003) Rhenium systematics in submarine MORB and back-arc basin glasses: laser ablation ICP- MS results. *Chemical Geology*, **196**, 259-281.

Sun, W.D., Hu, Y.H., Kamenetsky, V.S., Eggins, S.M., Chen, M., and Arculus, R.J. (2008) Constancy of Nb/U in the mantle revisited. *Geochimica et Cosmochimica Acta*, **72**, 3542-3549.

Takahashi, E. (1986) Melting of a dry peridotite KLB-1 up to 14 GPa: Implications on the origin of peridotitic upper mantle. *Journal of Geophysical Research*, **91**, 9367-9382.

Takahashi, E., Uto, K., and Schilling, J.G. (1987) Primary magma compositions and Mg/Fe ratios of their mantle residues along Mid Atlantic Ridge 29° N to 73° N. *Technical Report of ISEI Okayama University. Series A*, **9**, 1-4.

Takahashi, E., Shimazaki, T., Tsuzaki, Y., and Yoshida, H. (1993) Melting study of a peridotite KLB-1 to 6.5 GPa, and the origin of basaltic magmas. *Transactions of the Royal Society of London. Series A*, **342**, 105-120.

Takeo, A., Kawakatsu, H., Isse, T., Nishida, K., Shiobara, H., Sugioka, H., Ito, A., and Utada, H. (2018). In Situ Characterization of the Lithosphere-Asthenosphere System beneath NW Pacific Ocean Via Broadband Dispersion Survey With Two OBS Arrays. *Geochemistry, Geophysics, Geosystems*, **19**, 3529-3539.

Tatsumi, Y. and Eggins, S. (1995) Subduction Zone Magmatism, Frontiers in Earth Sciences, Eds., Hoffman, P. F., Jeanloz, R. and Knoll, A. H., Blackwell Science, Cambridge, 211 p.

Tatsumi, Y. Sakuyama, M., Fukuyama, H., and Kushiro, I. (1983) Generation of arc basalt magmas and thermal structure of the mantle wedge in subduction zones. *Journal of Geophysical Research*, **88**, 5815-5825.

Till, C.B., Grove, T.L., and Withers, A.C. (2012) The beginnings of hydrous mantle wedge melting. *Contributions to Mineralogy and Petrology*, **163**, 669-688.

Tseng, C.Y., Yang, H.J., Yang, H.Y., Liu, D., Tsai, C.L., Wu, H., and Zuo, G. (2007) The Dongcaohe ophiolite from the North Qilian Mountains: a fossil oceanic crust of the Paleo-Qilian ocean. *Chinese Science Bulletin*, **52**, 2390-2401.

Tsikouras, B., Pe-Piper, G., Piper, D.J., and Hatzipanagiotou, K. (2008) Triassic rift-related komatiite, picrite and basalt, Pelagonian continental margin, Greece. *Lithos*, **104**, 199-215.

Van Avendonk, H.J., Davis, J.K., Harding, J.L., and Lawver, L.A. (2017) Decrease in oceanic crustal thickness since the breakup of Pangaea. *Nature Geoscience*, **10**, 58-61.

van Hunen, J., and Čadek, O. (2009) Reduced oceanic seismic anisotropy by small-scale convection. *Earth and Planetary Science Letters*, **284**, 622-629.

Van Keken, P.E., Kita, S., and Nakajima, J. (2012) Thermal structure and intermediate-depth seismicity in the Tohoku-Hokkaido subduction zones. *Solid Earth Discuss*, **3**, 355-364.

VanDecar, J.C., Russo, R.M., James, D.E., Ambeh, W.B., & Franke, M. (2003) Aseismic continuation of the Lesser Antilles slab beneath continental South America. *Journal of Geophysical Research* **108**, doi:10.1029/2001JB000884.

Vargas, C. A., and Mann, P. (2013) Tearing and breaking off of subducted slabs as the result of collision of the Panama Arc - Indenter with northwestern South America. *Bulletin of the Seismological Society of America*, **103**, 2025-2046.

Vaughan, A.P., and Scarrow, J.H. (2003) Ophiolite obduction pulses as a proxy indicator of superplume events? *Earth and Planetary Science Letters*, **213**, 407-416.

Volynets, O.N., Ponomareva, V.V., and Babansky, A.D. (1997) Magnesian basalts of Shiveluch andesite volcano, Kamchatka. *Petrology*, **5**, 183–196.

Walter, M.J. (1998) Melting of garnet peridotite and the origin of komatiite and depleted lithosphere. *Journal of Petrology*, **39**, 29-60.

Wang, Z., Sun, S., Li, J., and Hou, Q. (2002) Petrogenesis of tholeiite associations in Kudi ophiolite (western Kunlun Mountains, northwestern China): implications for the evolution of back-arc basins. *Contributions to Mineralogy and Petrology*, **143**, 471-483.

Wiens, D.A., Kelley, K.A., and Plank, T. (2006) Mantle temperature variations beneath back-arc spreading centers inferred from seismology, petrology, and bathymetry. *Earth and Planetary Science Letters*, **248**, 30-42.

Williams, H., and Smyth, R. (1973) Metamorphic aureoles beneath ophiolite suites and Alpine peridotites: Tectonic implications with west Newfoundland examples. *American Journal of Science*, **273**, 594-621.

Witt-Eickschen, G., and O'Neill, H. S. C. (2005) The effect of temperature on the equilibrium distribution of trace elements between clinopyroxene, orthopyroxene, olivine and spinel in upper mantle peridotite. *Chemical Geology*, **221**, 65-101.

Workman, R.K., and Hart, S.R. (2005) Major and trace element composition of the depleted MORB mantle (DMM). *Earth and Planetary Science Letters*, **231**, 53-72.

Xia, X., and Song, S. (2010) Forming age and tectono-petrogenises of the Jiugequan ophiolite in the North Qilian Mountain, NW China. *Chinese Science Bulleti*n, **55**, 1899-1907.

Yakubchuk, A.S., Nikishin, A.M., and Ishiwatari, A. (1994) A late Proterozoic ophiolite pulse. Eds., A. Ishiwatari, J. Malpas, H. Ishizuka, *Proceedings of the 29th International Geological Congress Part D*, 273-286.

Yamashita, S., and Tatsumi, Y. (1994) Thermal and geochemical evolution of the mantle wedge in the northeast Japan arc: 2. Contribution from geochemistry. J*ournal of Geophysical Research*, **99**, 22285-22293.

Yamato, P., Burov, E., Agard, P., Le Pourhiet, L., and Jolivet, L. (2008) HP-UHP exhumation during slow continental subduction: Self-consistent thermodynamically and thermomechanically coupled model with application to the Western Alps. *Earth and Planetary Science Letters*, **271**, 63-74.

Yao, L., Sun, C., and Liang, Y. (2012) A parameterized model for REE distribution between low-Ca pyroxene and basaltic melts with applications to REE partitioning in low-Ca pyroxene along a mantle adiabat and during pyroxenite-derived melt and peridotite interaction. *Contributions to Mineralogy and Petrology*, **164**, 261-280.

Yoshida, H., and Takahashi, N. (1997) Chemical behavior of major and trace elements in the Horoman mantle diapir, Hidaka belt Hokkaido, japan. *Journal of Mineralogy, Petrology and Economic Geology*, **92**, 391-409 (in Japanese with English abstract).

Yoshikawa, M., and Nakamura, E. (2000) Geochemical evolution of the Horoman peridotite complex: Implications for melt extraction, metasomatism, and compositional layering in the mantle. *Journal of Geophysical Research*, **105**, 2879-2901.

Yoshikawa, M., and Ozawa, K. (2007). Rb–Sr and Sm–Nd isotopic systematics of the Hayachine–Miyamori ophiolitic complex: Melt generation process in the mantle wedge beneath an Ordovician island arc. *Gondwana Research*, **11**, 234-246.

Zhu, D.C., Wang, Q., Zhao, Z.D., Chung, S.L., Cawood, P.A., Niu, Y., Liu, S.A., Wu, F.Y., and Mo, X.X. (2015). Magmatic record of India-Asia collision. *Scientific Reports*, **5**, doi:10.1038/srep14289.

Appendix

Table A1: Optimized set of model parameters for one-dimensional steady-state decompressional fractional melting models without material influx and the assumed initial mineral modes and melting modes for DKSH1.

Dike: DKSH1					
Source: Primitive mantle					
Strength of melt separation: Accumulated					
Percentage of melting at the garnet stability field in F (wt%): 95.7					
Stage	Melting mode				
	Olivine	Spinel	Orthopyroxene	Clinopyroxene	Garnet
garnet	0.08	0.00	-0.19	0.81	0.30
spinel	-0.34	0.13	0.46	0.75	0.00
Stage	Lithology	Parameters for open system melting model			
		α [1]	γ [1]		
1	Gt lhz	0.000	0.000		
2	Gt lhz	0.005	0.900		
3	Gt lhz	0.020	0.900		
4	Gt/Sp lhz	0.150	1.000		
Source: MORB like mantle					
Strength of melt separation: Accumulated					
Percentage of melting at the garnet stability field in F (wt%): 88.7					
Stage	Melting mode				
	Olivine	Spinel	Orthopyroxene	Clinopyroxene	Garnet
garnet	0.08	0.00	-0.19	0.81	0.30
spinel	-0.34	0.13	0.46	0.75	0.00
Stage	Lithology	Parameters for open system melting model			
		α	γ		
1	Gt lhz	0.000	0.000		
2	Gt lhz	0.005	0.010		
3	Gt lhz	0.020	1.000		
4	Gt/Sp lhz	0.150	1.000		
Source: MORB like mantle					
Strength of melt separation: Instantaneous					
Percentage of melting at the garnet stability field in F (wt%): 99.9					
Stage	Melting mode				
	Olivine	Spinel	Orthopyroxene	Clinopyroxene	Garnet
garnet	0.08	0.00	-0.19	0.81	0.30
spinel	-0.34	0.13	0.46	0.75	0.00
Stage	Lithology	Parameters for open system melting model			
		α	γ		
1	Gt lhz	0.000	0.000		
2	Gt lhz	0.005	0.100		
3	Gt lhz	0.020	0.400		
4	Gt/Sp lhz	0.150	1.000		
Source: Depleted MORB like mantle					
Strength of melt separation: Accumulated					
Percentage of melting at the garnet stability field in F (wt%): 87.3					
Stage	Melting mode				
	Olivine	Spinel	Orthopyroxene	Clinopyroxene	Garnet
garnet	0.08	0.00	-0.19	0.81	0.30
spinel	-0.34	0.13	0.46	0.75	0.00
Stage	Lithology	Parameters for open system melting model			
		α	γ		
1	Gt lhz	0.000	0.000		
2	Gt lhz	0.005	0.200		
3	Gt lhz	0.020	0.900		
4	Gt/Sp lhz	0.150	1.000		

[1] α, and γ are the mass fraction of melt in the current system of the melting stage, and the separation rate, respectively. Gt lhz and Gt/Sp lhz are garnet lherzolite and spinel lherzolite.

Table A2: Optimized set of model parameters for one-dimensional steady-state decompressional fractional melting models without material influx and the assumed initial mineral modes and melting modes for DKSH2.

Dike: DKSH2					
Source: Primitive mantle					
Strength of melt separation: Accumulated					
Percentage of melting at the garnet stability field in F (wt%): 89.2					
Stage	Melting mode				
	Olivine	Spinel	Orthopyroxene	Clinopyroxene	Garnet
garnet	0.08	0.00	-0.19	0.81	0.30
spinel	-0.34	0.13	0.46	0.75	0.00
Stage	Lithology	Parameters for open system melting model			
		α [1]	γ [1]		
1	Gt lhz	0.000	0.000		
2	Gt lhz	0.005	0.900		
3	Gt lhz	0.020	0.900		
4	Gt/Sp lhz	0.150	1.000		
Source: MORB like mantle					
Strength of melt separation: Accumulated					
Percentage of melting at the garnet stability field in F (wt%): 76.6					
Stage	Melting mode				
	Olivine	Spinel	Orthopyroxene	Clinopyroxene	Garnet
garnet	0.08	0.00	-0.19	0.81	0.30
spinel	-0.34	0.13	0.46	0.75	0.00
Stage	Lithology	Parameters for open system melting model			
		α	γ		
1	Gt lhz	0.000	0.000		
2	Gt lhz	0.005	0.900		
3	Gt lhz	0.020	0.900		
4	Gt/Sp lhz	0.150	1.000		
Source: MORB like mantle					
Strength of melt separation: Instantaneous					
Percentage of melting at the garnet stability field in F (wt%): 99.9					
Stage	Melting mode				
	Olivine	Spinel	Orthopyroxene	Clinopyroxene	Garnet
garnet	0.08	0.00	-0.19	0.81	0.30
spinel	-0.34	0.13	0.46	0.75	0.00
Stage	Lithology	Parameters for open system melting model			
		α	γ		
1	Gt lhz	0.000	0.000		
2	Gt lhz	0.005	0.200		
3	Gt lhz	0.020	0.010		
4	Gt/Sp lhz	0.150	1.000		
Source: Depleted MORB like mantle					
Strength of melt separation: Accumulated					
Percentage of melting at the garnet stability field in F (wt%): 75.5					
Stage	Melting mode				
	Olivine	Spinel	Orthopyroxene	Clinopyroxene	Garnet
garnet	0.08	0.00	-0.19	0.81	0.30
spinel	-0.34	0.13	0.46	0.75	0.00
Stage	Lithology	Parameters for open system melting model			
		α	γ		
1	Gt lhz	0.000	0.000		
2	Gt lhz	0.005	0.900		
3	Gt lhz	0.020	1.000		
4	Gt/Sp lhz	0.150	1.000		

[1] α, and γ are the mass fraction of melt in the current system of the melting stage, and the separation rate, respectively. Gt lhz and Gt/Sp lhz are garnet lherzolite and spinel lherzolite.

Table A3: Optimized set of model parameters for one-dimensional steady-state decompressional fractional melting models without material influx and the assumed initial mineral modes and melting modes for RYO1.

Dike: RYO1					
Source: Primitive mantle					
Strength of melt separation: Accumulated					
Percentage of melting at the garnet stability field in F (wt%): 97.2					
Stage	Melting mode				
	Olivine	Spinel	Orthopyroxene	Clinopyroxene	Garnet
garnet	0.08	0.00	-0.19	0.81	0.30
spinel	-0.34	0.13	0.46	0.75	0.00
Stage	Lithology	Parameters for open system melting model			
		α [1]	γ [1]		
1	Gt lhz	0.000	0.000		
2	Gt lhz	0.005	0.900		
3	Gt lhz	0.020	0.900		
4	Gt/Sp lhz	0.150	1.000		
Source: MORB like mantle					
Strength of melt separation: Accumulated					
Percentage of melting at the garnet stability field in F (wt%): 90.1					
Stage	Melting mode				
	Olivine	Spinel	Orthopyroxene	Clinopyroxene	Garnet
garnet	0.08	0.00	-0.19	0.81	0.30
spinel	-0.34	0.13	0.46	0.75	0.00
Stage	Lithology	Parameters for open system melting model			
		α	γ		
1	Gt lhz	0.000	0.000		
2	Gt lhz	0.005	0.900		
3	Gt lhz	0.020	0.900		
4	Gt/Sp lhz	0.150	1.000		
Source: MORB like mantle					
Strength of melt separation: Instantaneous					
Percentage of melting at the garnet stability field in F (wt%): 99.9					
Stage	Melting mode				
	Olivine	Spinel	Orthopyroxene	Clinopyroxene	Garnet
garnet	0.08	0.00	-0.19	0.81	0.30
spinel	-0.34	0.13	0.46	0.75	0.00
Stage	Lithology	Parameters for open system melting model			
		α	γ		
1	Gt lhz	0.000	0.000		
2	Gt lhz	0.005	0.600		
3	Gt lhz	0.020	0.400		
4	Gt/Sp lhz	0.150	1.000		
Source: Depleted MORB like mantle					
Strength of melt separation: Accumulated					
Percentage of melting at the garnet stability field in F (wt%): 93.0					
Stage	Melting mode				
	Olivine	Spinel	Orthopyroxene	Clinopyroxene	Garnet
garnet	0.08	0.00	-0.19	0.81	0.30
spinel	-0.34	0.13	0.46	0.75	0.00
Stage	Lithology	Parameters for open system melting model			
		α	γ		
1	Gt lhz	0.000	0.000		
2	Gt lhz	0.005	0.200		
3	Gt lhz	0.020	1.000		
4	Gt/Sp lhz	0.150	1.000		

[1] α, and γ are the mass fraction of melt in the current system of the melting stage, and the separation rate, respectively. Gt lhz and Gt/Sp lhz are garnet lherzolite and spinel lherzolite.

Table A4: Optimized set of model parameters for one-dimensional steady-state decompressional fractional melting models without material influx and the assumed initial mineral modes and melting modes for RYO2.

Dike: RYO2

Source: Primitive mantle

Strength of melt separation: Accumulated

Percentage of melting at the garnet stability field in F (wt%): 98.0

Stage	Melting mode				
	Olivine	Spinel	Orthopyroxene	Clinopyroxene	Garnet
garnet	0.08	0.00	-0.19	0.81	0.30
spinel	-0.34	0.13	0.46	0.75	0.00

Stage	Lithology	Parameters for open system melting model	
		α [1]	γ [1]
1	Gt lhz	0.000	0.000
2	Gt lhz	0.005	0.900
3	Gt lhz	0.020	0.900
4	Gt/Sp lhz	0.150	1.000

Source: MORB like mantle

Strength of melt separation: Accumulated

Percentage of melting at the garnet stability field in F (wt%): 93.9

Stage	Melting mode				
	Olivine	Spinel	Orthopyroxene	Clinopyroxene	Garnet
garnet	0.08	0.00	-0.19	0.81	0.30
spinel	-0.34	0.13	0.46	0.75	0.00

Stage	Lithology	Parameters for open system melting model	
		α	γ
1	Gt lhz	0.000	0.000
2	Gt lhz	0.005	0.100
3	Gt lhz	0.020	1.000
4	Gt/Sp lhz	0.150	1.000

Source: MORB like mantle

Strength of melt separation: Instantaneous

Percentage of melting at the garnet stability field in F (wt%): 99.9

Stage	Melting mode				
	Olivine	Spinel	Orthopyroxene	Clinopyroxene	Garnet
garnet	0.08	0.00	-0.19	0.81	0.30
spinel	-0.34	0.13	0.46	0.75	0.00

Stage	Lithology	Parameters for open system melting model	
		α	γ
1	Gt lhz	0.000	0.000
2	Gt lhz	0.005	0.400
3	Gt lhz	0.020	0.700
4	Gt/Sp lhz	0.150	1.000

Source: Depleted MORB like mantle

Strength of melt separation: Accumulated

Percentage of melting at the garnet stability field in F (wt%): 93.9

Stage	Melting mode				
	Olivine	Spinel	Orthopyroxene	Clinopyroxene	Garnet
garnet	0.08	0.00	-0.19	0.81	0.30
spinel	-0.34	0.13	0.46	0.75	0.00

Stage	Lithology	Parameters for open system melting model	
		α	γ
1	Gt lhz	0.000	0.000
2	Gt lhz	0.005	0.100
3	Gt lhz	0.020	1.000
4	Gt/Sp lhz	0.150	1.000

[1] α, and γ are the mass fraction of melt in the current system of the melting stage, and the separation rate, respectively. Gt lhz and Gt/Sp lhz are garnet lherzolite and spinel lherzolite.

Table A5: Calculated adiabatic gradients, $(\partial T/\partial P)_S$ and parameters to estimate solidus conditions: temperature change for melting degree (F), ΔT; thermal expansion, α for solid and melt; partial volume, V for solid and melt; heat capacity, Cp for solid and melt; and enthalpy change of melting, ΔH; increase in melting degree with temperature increase at constant pressure, $(\partial F/\partial T)_P$; increase in temperature with pressure increase at constant melting degree, $(\partial T/\partial P)_F$.

Dike:	DKSH1	DKSH2	RYO1	RYO2	data source
$(\partial T/\partial P)_S$ [K/GPa]	57.8	58.5	58.1	58.3	
ΔT for F [K]	20.4	24.9	20.5	21.5	Takahashi et al. (1993)
α^L (10^5) [1/K]	10.9	11.2	10.7	10.9	Fei (1995)
V^L [kJ/GPa]	219	217	219	220	Lange and Carmichael (1987)
Cp^L [J/Mol/K]	95.2	94.7	94.7	95.9	Stebbins et al. (1984)
α^S (10^5) [1/K]			4.0		Fei (1995)
V^S [kJ/GPa]			45.9		Berman (1998), Berman and Brown (1985)
Cp^S [J/Mol/K]			193.2		Berman (1998), Berman and Brown (1985)
ΔH [kJ/Mol]			97.3		Kojitani and Akaogi (1997)
$(\partial F/\partial T)_P$ (10^3) [1/K]			3.8		Takahashi et al. (1993)
$(\partial T/\partial P)_F$ [K/GPa]			64.2		McKenzie and Bickle (1988)

Table A6: Sample means of mineral compositions (raw olivine Mg# and NiO wt%, spinel Cr#, clinopyroxene TiO_2 and Mg#; corrected olivine Mg# and NiO wt%, clinopyroxene Mg#), major and rare earth element concentrations of clinopyroxene grains, and igneous modal abundances of cumulus phases and matrix examined samples from the Cumulate Member.

Locality #	1		2		3		4		
Sample	77112324		15081610c		15081913j3		15081913c		
Stratigraphic height (m)	30		120		230		240		
Horizon	lower		lower		lower		lower		
Mineral compositions									
Olivine									
Mg#									
raw	0.85		0.85		0.87		0.85		
corrected	0.86		0.87		0.87		0.86		
NiO (wt%)									
raw	0.25		0.21		0.22		0.20		
corrected	0.24		0.19		0.22		0.19		
Spinel Cr#	0.51		0.39		0.41		0.31		
Clinopyroxene									
Mg#									
raw	0.91		0.90		0.92		0.90		
corrected	0.83		0.84		0.85		0.84		
Clinopyroxene grain	2g53	2g54	1g76	1g75	1g16	1g17	1g71	1g72	1g73
(wt%)									
SiO2	53.62	53.04	51.96	52.49	52.59	-	52.54	52.45	51.51
Al2O3	1.83	2.17	3.51	2.47	2.50	-	2.30	2.97	3.41
TiO2	0.24	0.29	0.65	0.54	0.57	-	0.40	0.49	0.54
FeO	2.86	3.20	3.38	3.22	2.64	-	3.15	3.38	3.36
MnO	0.10	0.13	0.07	0.07	0.09	-	0.11	0.10	0.12
MgO	16.64	16.36	15.61	16.00	16.78	-	16.52	16.15	15.89
CaO	23.61	23.62	23.94	24.01	23.89	-	23.85	23.24	23.77
Na2O	0.23	0.23	0.16	0.15	0.09	-	0.14	0.21	0.21
K2O	0.00	0.01	0.02	0.01	0.00	-	0.00	0.01	0.00
Cr2O3	0.49	0.59	0.58	0.38	0.38	-	0.42	0.63	0.89
NiO	0.04	0.04	0.01	0.01	0.03	-	0.02	0.02	0.02
total	99.66	99.68	99.87	99.35	99.55	-	99.44	99.65	99.73
(ppm)									
La	2.26	2.78	0.64	0.69	0.65	0.64	1.67	1.69	1.48
Ce	4.36	5.19	2.21	2.40	1.76	1.75	3.89	3.94	3.67
Pr	0.68	0.72	0.47	0.54	0.32	0.34	0.62	0.68	0.58
Nd	3.88	3.68	3.09	3.28	1.92	1.94	3.82	3.67	2.98
Sm	1.28	1.14	1.06	1.08	0.62	0.67	1.27	1.26	1.09
Eu	0.42	0.39	0.42	0.36	0.24	0.22	0.40	0.47	0.36
Gd	1.35	1.22	1.57	1.52	0.84	1.06	1.57	1.69	1.31
Tb	0.19	0.19	0.28	0.25	0.16	0.17	0.23	0.23	0.24
Dy	1.11	1.23	1.76	1.51	1.06	1.12	1.68	1.70	1.43
Ho	0.21	0.22	0.36	0.28	0.22	0.22	0.34	0.31	0.27
Er	0.54	0.59	0.86	0.78	0.58	0.55	0.91	0.85	0.67
Tm	0.07	0.08	0.13	0.13	0.09	0.09	0.12	0.12	0.09
Yb	0.48	0.51	0.81	0.69	0.51	0.56	0.76	0.80	0.59
Lu	0.06	0.07	0.11	0.11	0.08	0.08	0.10	0.10	0.08
Modal composition (vol%)									
Cumulus phase									
olivine	29.5	45.4	31.8	31.8	82.4	82.4	40.3	40.3	40.3
clinopyroxene	17.6	10.2	28.3	28.3	7.5	7.5	35.1	35.1	35.1
toal	47.0	55.6	60.1	60.1	90.0	90.0	75.4	75.4	75.4
Matrix									
olivine	18.4	15.2	14.1	14.1	2.5	2.5	4.2	4.2	4.2
clinopyroxene	23.0	19.0	17.6	17.6	3.1	3.1	5.2	5.2	5.2
amphibole	8.5	3.5	4.4	4.4	0.5	0.5	3.1	3.1	3.1
others	3.0	6.6	3.7	3.7	3.9	3.9	12.0	12.0	12.0
total	53.0	44.4	39.9	39.9	10.0	10.0	24.6	24.6	24.6

Table A6. (continue)

5			6		7		8				
15080403c1			15080403c2		15080403c6		17101409				
250			250		270		1170				
lower			lower		lower		middle				
	0.85			0.85		0.86			0.84		
	0.87			0.88		0.87			0.86		
	0.19			0.18		0.23			0.20		
	0.18			0.17		0.22			0.18		
	0.34			0.67		0.26			-		
	0.90			0.90		0.90			0.89		
	0.84			0.85		0.84			0.83		
1g14	1g11	1g12	1g53	1g55	1g5	1g8	1g20	1g30	1g26	1g29	1g30-2
51.66	52.44	52.72	53.23	53.14	52.88	52.03	51.99	51.99	52.67	52.55	53.47
3.94	2.52	2.56	1.88	2.17	2.52	3.21	3.07	2.95	3.03	2.67	1.56
0.56	0.53	0.50	0.33	0.37	0.57	0.54	0.61	0.49	0.50	0.50	0.29
3.42	3.02	3.03	2.92	2.98	3.09	3.10	3.44	4.10	3.16	3.48	3.17
0.11	0.12	0.10	0.11	0.12	0.09	0.08	0.14	0.12	0.10	0.11	0.11
15.70	16.22	16.26	16.59	16.40	16.24	15.90	15.82	15.78	16.36	16.02	16.63
23.04	23.88	23.79	24.05	24.05	23.72	23.98	23.59	23.10	23.22	23.63	23.89
0.40	0.16	0.16	0.10	0.11	0.13	0.13	0.19	0.20	0.25	0.19	0.12
0.01	0.00	0.00	0.00	0.00	0.04	0.00	0.01	0.02	0.01	0.00	0.01
0.82	0.41	0.37	0.38	0.48	0.37	0.74	0.54	0.72	0.43	0.50	0.22
0.02	0.01	0.02	0.01	0.01	0.03	0.00	0.01	0.03	0.02	0.02	0.01
99.66	99.30	99.50	99.61	99.83	99.66	99.69	99.40	99.51	99.74	99.67	99.46
1.05	1.26	1.52	0.75	0.62	0.80	0.86	0.67	0.64	0.61	2.21	0.48
2.79	3.72	4.63	2.16	1.79	2.63	2.57	2.74	2.39	2.48	7.89	1.61
0.53	0.74	0.86	0.41	0.36	0.52	0.53	0.68	0.59	0.56	1.88	0.39
3.02	4.74	5.51	2.59	1.97	3.30	3.15	4.73	3.85	3.90	12.34	2.50
1.06	1.78	1.90	0.82	0.70	1.19	1.18	1.89	1.64	1.69	4.80	0.99
0.40	0.59	0.72	0.31	0.24	0.39	0.38	0.58	0.57	0.50	1.60	0.37
1.25	2.15	2.53	1.01	0.80	1.45	1.44	2.62	2.17	2.00	6.50	1.33
0.21	0.30	0.40	0.16	0.13	0.26	0.23	0.49	0.39	0.35	1.01	0.22
1.42	2.04	2.58	1.20	0.88	1.58	1.41	2.95	2.60	2.35	7.00	1.58
0.25	0.37	0.51	0.20	0.17	0.30	0.27	0.60	0.56	0.47	1.34	0.29
0.70	1.02	1.41	0.55	0.40	0.86	0.69	1.60	1.47	1.15	3.74	0.77
0.10	0.13	0.21	0.07	0.07	0.11	0.09	0.21	0.20	0.15	0.46	0.12
0.61	0.83	1.18	0.45	0.33	0.80	0.60	1.38	1.20	1.07	3.27	0.67
0.09	0.12	0.19	0.06	0.04	0.10	0.08	0.17	0.17	0.14	0.43	0.10
49.6	43.8	25.7	10.6	16.2	35.5	65.4	20.0	4.8	32.5	15.0	4.8
20.1	30.3	30.1	25.2	35.1	33.3	20.3	12.0	18.2	15.5	19.4	18.2
69.7	74.2	55.8	35.8	51.3	68.9	85.7	32.0	23.0	48.0	34.4	23.0
9.4	9.6	17.3	22.9	16.2	11.0	4.9	26.7	30.5	20.0	24.7	30.5
11.8	12.0	21.7	28.7	20.3	13.8	6.1	33.3	38.1	25.0	30.8	38.1
6.3	0.9	3.9	7.3	5.9	4.0	0.5	7.3	8.0	5.5	9.7	8.0
2.8	3.4	1.2	5.2	6.3	2.3	2.8	0.7	0.6	1.5	0.4	0.6
30.3	25.8	44.2	64.2	48.7	31.1	14.3	68.0	77.0	52.0	65.6	77.0

Table A6. (continue)

9	10	11			12				13		
77112426	77112427	77112434			77112433				78081916		
1240	1410	1530			1560				1830		
middle	middle	middle			middle				middle		
0.85	0.85	-			-				-		
0.86	0.87	-			-				-		
0.24	0.25	-			-				-		
0.23	0.24	-			-				-		
0.55	0.33	0.33			0.30				-		
0.91	0.91	0.90			0.89				0.90		
0.84	0.84	0.86			0.85				0.87		
2g51	2g8	2g2	2g4	2g5	2g14	2g15	2g16	2g17	2g32	2g33	2g34
53.05	53.07	53.13	52.88	52.47	51.66	51.38	51.60	51.68	52.65	52.73	53.09
2.19	2.09	2.28	2.18	2.53	3.94	4.37	4.20	4.01	2.70	2.80	2.31
0.36	0.33	0.47	0.40	0.45	0.56	0.54	0.65	0.57	0.30	0.35	0.26
2.70	2.81	3.09	2.96	3.34	3.42	3.39	3.40	3.12	3.16	3.17	3.23
0.09	0.12	0.10	0.10	0.13	0.11	0.12	0.13	0.11	0.11	0.09	0.11
16.82	16.72	16.45	16.70	16.67	15.70	15.08	15.00	15.77	16.09	16.21	16.22
24.04	24.21	23.71	24.31	23.70	23.04	23.25	23.07	23.40	24.13	24.06	24.18
0.10	0.12	0.07	0.09	0.10	0.40	0.40	0.38	0.28	0.12	0.10	0.11
0.00	0.01	0.00	0.01	0.02	0.01	0.01	0.02	0.00	0.00	0.00	0.00
0.30	0.25	0.23	0.29	0.34	0.82	0.93	0.85	0.88	0.36	0.46	0.34
0.01	0.04	0.03	0.02	0.01	0.02	0.04	0.04	0.02	0.03	0.02	0.02
99.66	99.75	99.56	99.93	99.75	99.66	99.50	99.33	99.83	99.66	99.99	99.85
0.82	1.30	0.52	0.53	0.53	0.72	0.81	0.78	0.67	0.52	0.34	0.44
2.35	3.52	1.83	1.86	1.82	2.43	2.81	3.03	2.30	1.57	1.30	1.60
0.42	0.65	0.39	0.41	0.39	0.48	0.53	0.63	0.48	0.33	0.28	0.35
2.18	3.97	2.33	2.51	2.53	2.78	3.14	3.87	3.05	2.12	1.84	2.29
0.65	1.41	0.80	0.93	0.91	1.11	1.13	1.42	1.10	0.94	0.79	0.93
0.25	0.48	0.29	0.33	0.32	0.39	0.43	0.50	0.41	0.39	0.26	0.34
0.87	2.04	1.06	1.17	1.16	1.36	1.31	1.79	1.51	1.41	1.12	1.36
0.14	0.38	0.18	0.20	0.18	0.22	0.24	0.33	0.26	0.24	0.18	0.24
0.95	2.75	1.18	1.41	1.25	1.58	1.71	2.18	1.84	1.61	1.14	1.54
0.17	0.55	0.22	0.26	0.25	0.30	0.32	0.44	0.35	0.35	0.23	0.31
0.50	1.52	0.64	0.70	0.63	0.86	0.90	1.12	0.97	0.87	0.64	0.83
0.07	0.22	0.09	0.10	0.09	0.12	0.13	0.16	0.13	0.12	0.08	0.11
0.49	1.41	0.64	0.64	0.63	0.72	0.78	1.05	0.83	0.76	0.53	0.64
0.06	0.19	0.08	0.09	0.10	0.10	0.11	0.15	0.12	0.10	0.07	0.08
57.6	56.0	25.6	25.6	25.6	3.9	3.9	3.9	3.9	12.5	3.6	14.2
16.2	33.6	46.0	46.0	46.0	47.7	47.7	47.7	47.7	66.1	58.7	53.2
73.9	89.6	71.7	71.7	71.7	51.6	51.6	51.6	51.6	78.5	62.3	67.4
8.6	3.0	9.3	9.3	9.3	19.3	19.3	19.3	19.3	6.3	14.3	11.0
10.8	3.7	11.7	11.7	11.7	24.2	24.2	24.2	24.2	7.9	17.9	13.8
5.3	1.1	2.1	2.1	2.1	1.0	1.0	1.0	1.0	4.2	2.2	1.8
1.5	2.6	5.2	5.2	5.2	3.9	3.9	3.9	3.9	3.0	3.3	6.0
26.1	10.4	28.3	28.3	28.3	48.4	48.4	48.4	48.4	21.5	37.7	32.6

Table A6. (continue)

14			15			16		17		18		
79061403			78081907b			78082007b		78082609		78082004		
1920			2250			2410		2510		2630		
middle			upper			upper		upper		upper		
	-			0.86			-		0.86		0.85	
	-			0.88			-		0.88		0.88	
	-			0.22			-		0.23		0.20	
	-			0.21			-		0.22		0.18	
	0.27			0.56			0.53		0.53		0.35	
	0.88			0.92			0.91		0.91		0.89	
	0.84			0.86			0.86		0.86		0.85	
2g36	2g37	2g38	2g42	2g43	2g44	2g45	2g47	2g55	2g57	2g29	2g30	2g31
51.92	52.28	51.82	53.15	53.03	52.99	51.74	53.09	52.93	53.21	52.32	52.67	52.52
3.41	3.23	3.55	1.72	1.82	1.97	3.23	2.01	2.33	1.82	3.25	3.18	3.01
0.56	0.56	0.47	0.22	0.27	0.29	0.46	0.34	0.43	0.24	0.37	0.43	0.34
3.80	3.41	3.83	2.30	2.69	2.81	2.78	2.69	2.71	3.02	3.50	3.64	3.28
0.12	0.16	0.12	0.11	0.10	0.10	0.08	0.10	0.09	0.11	0.09	0.10	0.10
16.41	16.48	15.69	17.26	16.66	16.55	16.26	16.67	16.74	16.42	15.91	16.84	16.25
22.82	22.82	23.47	24.25	24.48	24.10	24.05	24.20	23.85	23.82	23.77	22.57	23.66
0.18	0.19	0.19	0.09	0.11	0.13	0.15	0.09	0.23	0.20	0.17	0.11	0.18
0.00	0.00	0.00	0.00	0.00	0.00	0.00	0.00	0.00	0.00	0.01	0.01	0.01
0.47	0.44	0.50	0.42	0.25	0.48	0.88	0.37	0.46	0.62	0.43	0.30	0.31
0.03	0.01	0.03	0.03	0.00	0.03	0.03	0.03	0.03	0.02	0.03	0.00	0.02
99.73	99.60	99.68	99.54	99.42	99.45	99.66	99.59	99.80	99.47	99.85	99.85	99.66
0.85	1.23	0.73	0.55	0.62	0.49	0.65	0.61	0.84	0.96	0.53	0.55	0.57
3.68	5.13	2.73	1.87	1.91	1.44	1.85	1.81	2.99	3.58	2.02	2.21	2.31
0.91	1.20	0.63	0.35	0.33	0.28	0.40	0.39	0.62	0.70	0.42	0.47	0.51
5.91	7.76	4.26	2.22	2.00	1.60	2.41	2.27	3.62	4.07	2.55	3.01	2.99
2.29	2.83	1.71	0.83	0.69	0.56	0.90	0.87	1.26	1.43	0.95	1.07	1.06
0.79	0.92	0.57	0.32	0.25	0.22	0.32	0.32	0.43	0.51	0.33	0.37	0.41
2.95	3.44	2.12	1.13	0.81	0.75	1.14	1.11	1.62	1.87	1.20	1.35	1.41
0.48	0.56	0.35	0.18	0.14	0.12	0.19	0.19	0.26	0.29	0.21	0.23	0.25
3.11	3.69	2.39	1.13	0.90	0.89	1.32	1.31	1.71	1.88	1.42	1.55	1.58
0.62	0.71	0.45	0.21	0.17	0.16	0.26	0.25	0.34	0.37	0.29	0.29	0.31
1.70	1.93	1.21	0.58	0.41	0.44	0.67	0.65	0.88	1.01	0.76	0.80	0.86
0.22	0.26	0.17	0.07	0.06	0.06	0.09	0.09	0.12	0.13	0.10	0.11	0.11
1.44	1.78	1.12	0.47	0.39	0.39	0.57	0.56	0.80	0.89	0.64	0.69	0.72
0.19	0.24	0.15	0.06	0.05	0.05	0.08	0.08	0.11	0.12	0.08	0.10	0.10
7.7	0.2	19.2	48.9	48.9	18.9	32.5	34.4	45.3	24.7	14.7	17.6	17.6
46.0	49.2	40.9	11.4	11.4	43.8	35.0	29.9	15.8	36.2	62.1	51.1	51.1
53.6	49.4	60.1	60.4	60.4	62.7	67.5	64.3	61.1	60.9	76.8	68.7	68.7
18.4	19.7	14.3	15.6	15.6	13.8	12.7	14.1	13.8	12.1	8.7	11.6	11.6
23.0	24.6	17.8	19.6	19.6	17.3	15.9	17.7	17.2	15.1	10.8	14.5	14.5
3.4	5.0	4.8	1.8	1.8	5.6	1.8	0.3	7.4	8.6	3.3	2.7	2.7
1.5	1.3	3.0	2.6	2.6	0.6	2.1	3.6	0.5	3.3	0.4	2.5	2.5
46.4	50.6	39.9	39.6	39.6	37.3	32.5	35.7	38.9	39.1	23.3	31.3	31.3

Table A7. Means of REE concentrations and the chondrite-normalized REE ratios ((Dy/Yb)n, (Sm/Gd)n, and (Ce/Sm)n) of the fractionated parental magmas for the samples containing > 60 % of cumulus phases for a dunite and wehrlites and > 25 % of clinopyroxene in mineral modes for the wehrlites in the Cumulate member. Standard errors (1SEs) for the REE ratios are also shown.

Locality #	2	3	4	5	7	9	10
Horizon			lower				
Sample	15081610c	15081913j3	15081913c	15080403c1	15080403c6	77112426	77112427
(ppm)							
La	0.80	0.84	2.80	1.61	1.37	0.91	4.13
Ce	2.70	2.18	6.17	4.37	4.06	2.53	10.15
Pr	0.57	0.40	0.95	0.81	0.77	0.43	1.68
Nd	3.44	2.23	4.92	4.71	4.42	2.13	8.94
Sm	1.07	0.70	1.50	1.54	1.42	0.58	2.52
Eu	0.38	0.25	0.51	0.52	0.44	0.21	0.78
Gd	1.45	0.98	1.71	1.68	1.57	0.71	3.06
Tb	0.25	0.16	0.25	0.24	0.25	0.11	0.54
Dy	1.45	1.07	1.69	1.60	1.51	0.73	3.73
Ho	0.28	0.21	0.32	0.28	0.29	0.13	0.72
Er	0.72	0.56	0.84	0.78	0.77	0.38	2.00
Tm	0.11	0.09	0.11	0.11	0.10	0.06	0.29
Yb	0.65	0.58	0.76	0.67	0.71	0.38	1.90
Lu	0.10	0.09	0.10	0.10	0.09	0.05	0.27
(Ce/Sm)n	0.63	0.78	1.03	0.71	0.71	1.10	1.01
(Sm/Gd)n	0.99	0.96	1.17	1.23	1.22	1.09	1.10
(Dy/Yb)n	1.49	1.22	1.49	1.60	1.42	1.28	1.31
1SE							
(Ce/Sm)n	0.01	0.02	0.02	0.02	0.02	0.04	0.05
(Sm/Gd)n	0.02	0.03	0.02	0.04	0.03	0.06	0.07
(Dy/Yb)n	0.02	0.03	0.02	0.03	0.02	0.03	0.04

Table A7. (continue)

11	13	14	15	16	17	18
middle					upper	
77112434	78081916	79061403	78081907b	78082007b	78082609	78082004
1.04	1.06	1.10	0.58	0.90	1.07	1.27
3.45	3.37	3.95	1.74	2.50	3.79	4.72
0.70	0.67	0.87	0.31	0.51	0.73	0.94
4.03	4.00	5.66	1.79	2.91	4.06	5.27
1.25	1.46	2.06	0.59	0.99	1.29	1.63
0.43	0.52	0.67	0.22	0.35	0.44	0.55
1.45	1.90	2.37	0.71	1.16	1.56	1.85
0.23	0.30	0.38	0.11	0.19	0.24	0.30
1.53	1.93	2.54	0.75	1.28	1.52	1.97
0.28	0.39	0.48	0.14	0.25	0.30	0.38
0.77	1.02	1.27	0.36	0.64	0.79	1.02
0.11	0.14	0.17	0.05	0.09	0.11	0.14
0.75	0.86	1.18	0.32	0.56	0.72	0.88
0.11	0.12	0.16	0.05	0.08	0.10	0.12
0.69	0.58	0.48	0.74	0.63	0.73	0.72
1.16	1.03	1.17	1.11	1.14	1.11	1.18
1.36	1.50	1.44	1.55	1.54	1.42	1.50
0.01	0.01	0.02	0.01	0.01	0.01	0.01
0.01	0.02	0.06	0.02	0.02	0.01	0.02
0.01	0.01	0.03	0.01	0.01	0.01	0.01